A geophysical survey in the Chocaya Basin in the central Valley of Cochabamba, Bolivia, using ERT and TEM

Hannes Pilser

Dissertations in Geology at Lund University,
Master's thesis, no 581
(45 hp/ECTS credits)

Department of Geology
Lund University
2020

A geophysical survey in the Chocaya Basin in the central Valley of Cochabamba, Bolivia, using ERT and TEM

Master's thesis

Hannes Pilser

Department of Geology
Lund University
2020

Contents

Cover Picture: From the valley of Cochabamba waiting for a TEM measurement to finish. Facing north with the highest peak of the surrounding mountains (Tunari) in the background. Photo: Hannes Pilser.

A geophysical survey in the Chocaya Basin in the central Valley of Cochabamba, Bolivia, using ERT and TEM

HANNES PILSER

Pilser, H., 2020: A geophysical survey in the Chocaya Basin in the central Valley of Cochabamba, Bolivia, using ERT and TEM. *Dissertations in Geology at Lund University*, No. 581, 40 pp. 45 hp (45 ECTS credits) .

Abstract:
The Chocaya Basin is situated in the north-western part of the Valley of Cochabamba, Bolivia, where a semi-arid climate prevails. The increasing population is dependent on local aquifers for drinking water and irrigation. Wells are used to extract water. Scarce amount of rainfall, mainly during the dry season, and constructions of buildings, are reducing the infiltration of water in the soil and consequently the net recharge of the aquifers. This has resulted in deeper wells, lower groundwater levels and the risk of depleting the aquifers.

This thesis investigates the current situation of the hydrology and hydrogeology of the valley, in particular the Chocaya Basin, where a potential aquifer is located. The study area is mainly on farmland and at parts of the Chocaya River. The aim is to map the geometry of this potential aquifer. Two geophysical methods were applied, ERT (Electrical Resistivity Tomography) and TEM (Transient Electromagnetic Method). The ERT method is based on passing a current through the subsurface and measuring the resistivity of the ground, while the TEM uses transient waves that are sent through the ground. The ground acts as a conductor that induces electrical current into the surrounding material, which generates a secondary wave. Equipment at the surface registers these secondary waves and makes it possible to calculate the resistivity of the subsurface, i.e. the ability of materials to resist the flow of electrical current. Different geological materials have different resistivities, making it possible to determine the lithology and thereby the dimension of the potential aquifer.

The use of both TEM and ERT helps to obtain more accurate results. In addition, lithology reports from nearby wells were used to characterise the top 100 m of the subsurface. The data processing showed that the TEM results in this area were more reliable. For this reason, data from the TEM were mainly used for interpretations and conclusions. The results show that the top 50–100 m part of the subsurface in the study area has a high resistivity (≈1000–2000 Ωm). High resistivities are linked to coarse sediments such as gravel and sand. Further down, the resistivity drops to approximately 100 Ωm. The lithology report indicates that the sediment consists of mainly gravel and sand down to 75 m and below finer sediments become more abundant. These results of the measurements are in line with the geological history of the valley: alluvial fan deposits on top lacustrine and fluviolacustrine sediments. Overall, the dimensions of the potential aquifer can be linked to the high resistivities, i.e the top 50–100 m of the ground. There, water can infiltrate and be stored in the potential aquifer.

An open surface is needed for a good infiltration of water through the local geological material. However, there is a high demand of construction buildings due to the increase in the population, which would reduce the infiltration of water in this area for recharging the potential aquifer.

Some additional TEM and ERT measurements were performed outside of the study area. They should contribute to assess the resistivity of the bedrock and to find an explanation for the existence of a thermal spring (Liriuni) located near the study area.

Keywords: ERT, TEM, geophysics, Cochabamba, aquifer

Supervisor(s): Andres Gonzales, Dan Hammarlund

Subject: Geology, Geophysics

Hannes Pilser, Department of Geology, Lund University, Sölvegatan 12, SE-223 62 Lund, Sweden. E-mail: nat15hpi@student.lu.se

En geofysisk undersökning av Chocaya bassängen i dalen av Cochabamba i Bolivien med ERT och TEM

HANNES PILSER

Pilser, H., 2020: En geofysisk undersökning av Chocaya bassängen i dalen av Cochabamba i Bolivian med ERT och TEM. *Examensarbeten i geologi vid Lunds universitet*, Nr. 581, 40 sid. 45 hp.

Sammanfattning:
Chocaya Basin ligger i den nordvästra delen av dalen Cochabamba i Bolivia, där ett halvtorrt klimat råder. Den ökande befolkningen är beroende av lokala akviferer för dricksvatten och jordbruk, där brunnar används för att utvinna vattnet. Låg nederbörd, främst under torrperioden, och uppförandet av nya hus eller fabriksbyggnader, påverkar infiltrationen av vattnet i jorden och därmed akviferernas påfyllning. Detta har resulterat i djupare brunnar, lägre grundvattennivåer och utökat risken för att tömma akviferna.

Detta arbete undersöker den nuvarande situationen av hydrologin och hydrogeologin i dalen, särskilt Chocaya-bassängen, där en potentiell akvifer förekommer. Området som utforskats ligger främst på jordbruksmark, men inkluderar även delar av Chocaya-floden. Målet är att kartlägga geometrin för denna potentiella akvifer. Två geofysiska metoder har använts: ERT (Electrical Resistivity Tomography) och TEM (Transient Electromagnetic Method). ERT-metoden bygger på att leda en ström genom jorden vilket möjliggör mätning av jordens resistivitet, medan TEM använder transienta vågor som skickas genom i jordlager. Geologiska material/sediment kan fungera som en ledare och kan inducera en elektrisk ström till omgivande material. Detta genererar i sin tur en sekundär våg. Utrustningen vid ytan registrerar dessa sekundära vågor och beräknar därmed materialets resistivitet, det vill säga markens förmåga att motstå en elektrisk ström. Olika geologiska material ger upphov till olika resistiviteter. Med hjälp av de uppmätta resistiviteterna är det möjligt att fastställa litologin och därmed kartlägga dimensionen av den potentiella akviferen.

De båda metoderna användes som komplement med syfte att uppnå detaljerade och mer exakta resultat. Dessutom användes två litologirapporter från närliggande brunnar för att identifiera hur litologin varierar i de översta 100 metrarna. Datahanteringen visade att TEM-resultaten inom detta område var mer tillförlitliga. Sålunda har främst TEM-data använts gällande tolkningar och slutsatser. Resultaten visar att höga resistiviteter (≈1000–2000 Ωm) dominerar i de översta 50–100 metrarna av marken i studieområdet. Därefter sjunker resistiviteten till cirka 100 Ωm. Höga resistiviteter är kopplade till grova sediment, såsom grus och sand. Enligt litologirapporterna består sedimenten huvudsakligen av grova sediment ner till 75 m djup. Andelen finare sediment blir därefter högre. Resultaten av mätningarna stämmer väl överens med dalens geologiska historia: alluvialkoner deponerade över lakustrina sediment. Sammanfattningsvis kan sägas att geometrin hos den potentiella akviferen kopplas till de höga resistiviteterna och därmed de översta 50–100 metrarna i marken. I den delen av marken kan vatten infiltrera och lagras i den potentiella akviferen.

En öppen yta behövs för en god infiltration av vatten genom det lokala geologiska materialet. Befolkningsökningen genererar dock stor efterfrågan på bygglov, vilket skulle resultera i en minskad infiltration av vatten i området och påverka nettouppladdningen av den potentiella akviferen.

Kompletterande TEM- och ERT-mätningar genomfördes utanför studieområdet. Dessa bidrar till att klarlägga berggrundens resistivitet och finna en förklaring till förekomsten av ett termiskt källa (Liriuni) beläget i närheten.

Nyckelord: ERT, TEM, geofysik, Cochabamba, akvifer

Handledare: Andres Gonzales, Dan Hammarlund

Ämnesinriktning: Geologi, Geofysik

Hannes Pilser, Geologiska institutionen, Lunds Universitet, Sölvegatan 12, 223 62 Lund, Sverige. E-post: nat15hpi@student.lu.se

1 Introduction

The Chocaya Basin is located in the highlands of Bolivia, northwest of the city of Cochabamba. The climate is semi-arid, with annual precipitation rates lower than 600 mm, resulting in water shortage. The local population of over a million inhabitants is dependent on local aquifers in the northern and western part of the Valley of Cochabamba for fresh drinking water supply and irrigation purposes. The high demand for drinking water will increase further with a growing population. Low precipitation rates in the area in combination with urban expansion are threatening the local groundwater processes and the infiltration capacity in the groundwater recharge areas, which all have a negative impact on the groundwater storage of the aquifers. Due to the increasing demand of drinking water, local people are drilling numerous wells to extract water from the aquifers. They are allowed to do so since there is no strict regulation or law in Bolivia prohibiting such activities. Assuming this process will continue, the aquifer will fail to recover its loss of groundwater since more water is extracted than its sources can provide. In the long run the aquifer may risk being depleted (Renner & Velasco 2000; pers.comm. Gonzales 2019).

The project is in collaboration with Laboratorio de Hidráulica (Hydraulics lab) and Centro Agua at Universidad Mayor de San Simon (UMSS) in Cochabamba, together with Engineering Geology at Lund University, and with funding from SIDA (Swedish International Development Cooperation Agency) and Geoscientists Without Borders (GWB).

2 Objectives

The hydrology and hydrogeology within the Valley of Cochabamba is currently not well known. The UMSS has envisioned to investigate the knowledge of the hydrology and hydrogeology of the Valley of Cochabamba in order to be able to use and extract the water from the aquifers as efficiently as possible without risking their depletion. This thesis is part of this project and primarily aims to map the general geometry of a potential aquifer in the Chocaya basin. The geophysical methods Electrical Resistivity Tomography (ERT) and Transient Electromagnetic (TEM) were used. If made possible by geophysical methods, the thesis secondarily aims to determine depth to the bedrock in this area, for this is not well known within the valley. After finishing all of the geophysical surveys there was time over for further research. Firstly, to determine the resistivity of the bedrock. For this, measurements were performed closer to the mountain where the bedrock is closer to the surface. Both ERT and TEM measurements were performed. Secondly, within the mountainous zone, there is a thermal bath called Liriuni. The existence of this thermal bath is rather unusual since Cochabamba and its surroundings is not in a geological active area. Two ERT measurements were carried out in Liriuni attempting to find an explanation for the thermal activity in this area.

3 Study area

3.1 Geography

The study site is located in the central Valley of Cochabamba in the central part of Bolivia in the Eastern Cordillera within the Andean mountain range (Fig. 1). The study area lies in the north-western part of the valley and is an open farmland and part of the adjacent Chocaya River (Fig. 1). The farmland and the river border each other. Additional investigations were done at three locations of the mountain area north of the study area. In this thesis the three locations will be referred to as: “the forest”, “the soccer field” and “Liriuni”, with the latter being furthest away from the study area (Fig. 1). The area of the central Valley of Cochabamba is approximately 1150 km^2 (Neumann-Redelin et al. 1978). The Valley of Cochabamba is situated within the latitudes 17.28°S – 17.18°S and longitudes 66.23°W – 66.07°W. The valley hosts the fourth largest city in Bolivia, Cochabamba, which also is the capital of the department of Cochabamba (Renner & Velasco 2000). According to the National Institute of Statistics of Bolivia (INE, according to its initials in Spanish), the Department of Cochabamba was home to 1.9 million people in 2016, with an increasing population. More than two thirds (69.1%) live in urban areas and the rest in rural areas. Cochabamba City has roughly 1 million people (INE 2016). The lowest part of the valley is situated at 2470 m above sea level (m.a.s.l.). The valley is surrounded by mountains and the highest peaks are located in the northern and western parts, which reach up to 5035 m.a.s.l. In the east, the valley is divided from the Sacaba Valley by a ridge with a NNW – SSE direction. The mountains in the southern part are eroded and do not exceed 3200 m.a.s.l. (Neumann-Redelin et al. 1978).

Cochabamba and the Valley of Cochabamba are located in the subandean belt. The climate is semi-arid in the highland of the valley and temperate in the valley. During the year the average temperatures stay constant with only minor variations. The mean annual temperature is 17.5°C. However, temperatures can range from 35°C and 5°C during the day. The hottest months of the year are during the wet season between October and February, while June and July are regarded as the coldest months (Renner & Velasco 2000).

The Valley of Cochabamba receives 400 – 600 mm of rainfall annually and the mountains surrounding the valley 800 – 1300 mm. Roughly 87% of the total precipitation falls during the summer months, especially in January. More than 10 mm/month of rainfall are rare in the winter months (Neumann-Redelin et al. 1978; GEOBOL 1979; Renner & Velasco 2000).

At the edge of the valley, the vegetation consists mainly of high steppe and high mountain prairie, naturally dominated by grass and bushes. Further to the centre, the vegetation changes to trees, bushes and denser vegetation. This area has also favourable conditions regarding climate, humidity and soil. Therefore, agriculture with the help of irrigation becomes dominant and includes the cultivation of maize, alfalfa, vegetables, potatoes, tubers, cereals, vegetables and many different kind of fruit (Renner & Velasco 2000; Saldías et al. 2013).

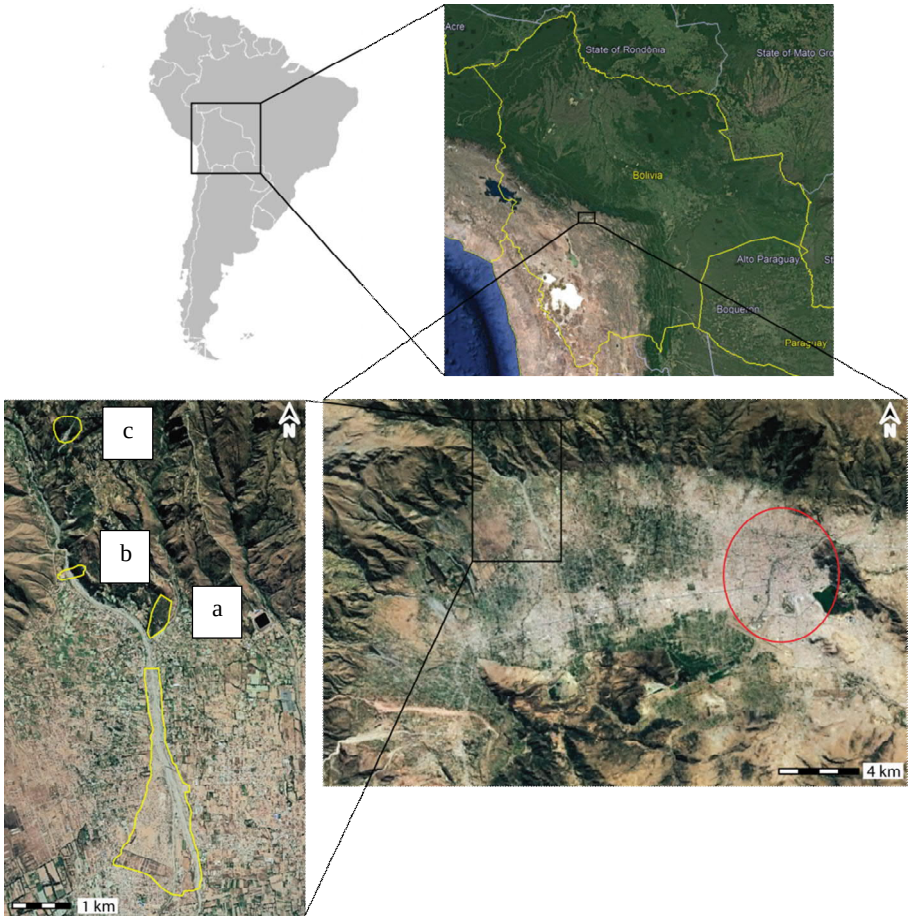

Figure 1. Overview of the location of the study area. Bottom right shows the Valley of Cochabamba where Cochabamba situated within the red circle. The study area is in the northwestern part of the valley (black box) and is marked by the big yellow area in the bottom left picture. The smaller marked areas are where the additional investigations were done with "the forest" (a) being the closes to the study area, followed by "the soccer field" (b) and "Liriuni" (c) located within the mountainous area, furthest from the study area.

The Rocha River is the main river of the Valley of Cochabamba. Its source is in the Sierra de Cochabamba in the east and flows west through the Sacaba Valley to the city of Cochabamba and further to the village Vinto (southwest). In Vito it changes direction to the south and flows out of the valley where it merges with other rivers before reaching Río Grande and draining out to the Amazon River. Other rivers flow through the valley and feed the Rocha River, but their sources are in the Cordilleran mountain range in the north and west. These rivers are either torrential or intermittent, meaning that the amount of water depends on precipitation rates or that water flow is only occasional. (Renner & Velasco 2000). Due to irrigation, farming and other purposes, water is extracted from the rivers, which decreases the river flow downstream (pers. comm. Gonzales 2019).

3.2 Geology

3.2.1 General geology

Bolivia consists of two different types of territories (i.e. lowlands and highlands), resulting in a diverse geology. The lowlands with the Beni and Chaco Plains (Fig. 2) have altitudes below 400 m.a.s.l. This territory also contains part of the Amazon catchment (Argollo & Iriondo 2008). The highlands are part of the Andean mountain range. The widest section, approximately 700 km, of the Andes is located in the Central Andes in Bolivia (Gregory-Wodzicki 2000). The Central Andes in Bolivia vary are divided into three regions: The Western Cordillera, the Altiplano, the Eastern Cordillera (in which the Valley of Cochabamba is located). Both territories are separated by a transition zone known as the Subandean zone (Fig. 2) (Murray et al. 2010).

The Valley of Cochabamba can be divided into three morphologically different zones: (1) the mountainous zone, (2) the zone of slope and piedmont and (3) the zone of the plain. The mountainous zone consists of the Tunari and Mazo Cruz mountain ranges in the north and west of the valley and hills in the southern and south-eastern side. The high slope gradient in the mountainous zone triggers landslides and collapses are common. Due to rainfall and glaciation, sediments from this area are transported to the valley, forming alluvial cones. The numerous alluvial cones in the valley form the slope and piedmont and are predominantly found in the northern and western part of the valley. In general, the sediments of the alluvial cones are coarse-grained near the edge of the valley but become

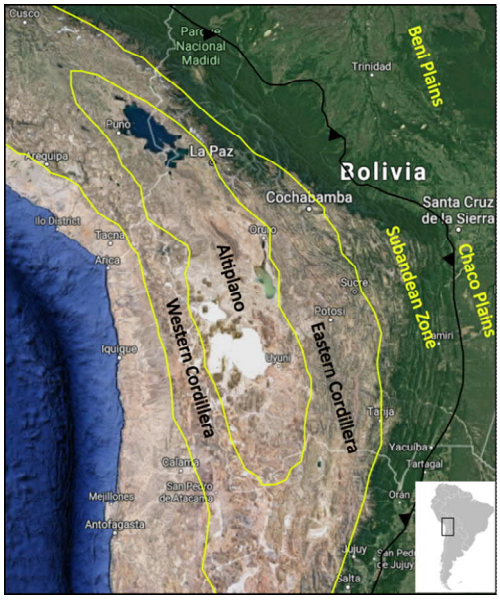

Figure 2. Bolivia is geologically divided into the highlands in the west and the lowlands in the east. The highlands are divided into the Western Cordillera, the Altiplano and the Eastern Cordillera. The lowlands are divided into the Beni and Chaco plains. The highlands and lowlands are separated by the transition zone known as the Subandean zone. Modified from Murray et al. (2010).

gradually more fine-grained closer to the centre. The zone of the plain is located in the centre of the valley, including the city of Cochabamba. It is dominated by fluvio-lacustrine sediments and consists mainly of fine sediment such as silt and clays (Renner & Velasco 2000).

3.2.2 Tectonic evolution

The tectonic evolution of Bolivia and of the central Andes dates back to the Mesoproterozoic (1200 – 1100 Ma). At the time, cratons like Laurentia, Amazonia and Pampia, as well as the Arequipa and Antofalla blocks (as of now referred to as Arequipa-Antofalla) were present. For simplification purposes, the Pampia Craton is not included in this description. During the Mesoproterozoic, Laurentia accreted to Arequipa-Antofalla, and they in turn accreted to Amazonia (Fig. 3A) (Ramos 2008). Approximately 1000 Ma, the Arequipa-Antofalla were enclosed by Laurentia and Amazonia, which also resulted in a slab break-off (Fig. 3B) (Ramos 2008). As a consequence of this amalgamation, the Grenville orogeny formed on Arequipa-Antofalla and the Sunsas orogeny on Amazonia. At this time the supercontinent Rodinia had formed. (Fig. 3B). In late Proterozoic times, 850 – 600 Ma, Rodinia broke up and an aulacogen (failed triple junction) formed between Arequipa-Antofalla and Amazonia (Fig. 3C) (Ramos 2008).

At the transition from the late Proterozoic to the Cambrian, the boundary between Amazonia and the Arequipa-Antofalla experienced an extensional phase, creating a retroarc basin (Fig. 3D) (Ramos 2008). Ramos (2008) further mentions that there could have been a subduction zone between the Chilenia terrane and Arequipa-Antofalla (Ramos 2008). During the Middle Ordovician the so-called Famatinian orogen took place at the southwestern margin of the supercontinent Gondwana. This orogeny set the boundary between the Altiplano and the Eastern Cordillera that exists today and deformed the Eastern Cordillera in the so-called Hercynian deformation (Fig. 3E) (Argollo & Iriondo 2008; Rapalini et al. 2018; Rojas Vera et al. 2019). The orogeny continued during the Silurian and Devonian, creating the Proto Eastern Cordillera (Fig. 3F). During the Carboniferous a viscoelastic basin

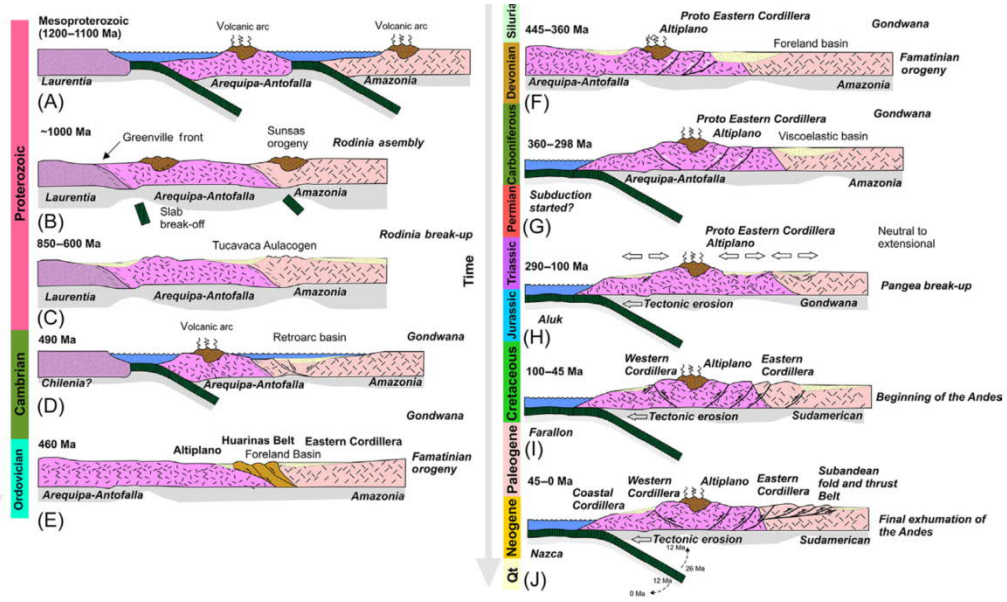

Figure 3. Tectonic evolution of Bolivia and the central Andes from 1200 Ma – present. From Rojas Vera et al. (2019).

formed at the retro-foreland basin (Fig. 3G). It is also possible that the subduction and the beginning of the Andes started during this time (Ramos 2008).

The Mesozoic is characterized as an extensional regime. The extension was minor in the Early to Middle Mesozoic but at the onset of the Cretaceous a rifting stage had matured (Fig. 3H) (Ramos 2018; Rojas Vera et al. 2019). The Andes, as we know them today, started to form in the Early Cretaceous to Eocene (Fig. 3I) (Lavenu et al. 2000). The formation of the Andes also meant the start of volcanic activity, at approximately 20 Ma (Argollo & Iriondo 2008). According to Gregory-Wodzicki (2000), the Eastern Cordillera had only gained 25 – 30% of its current altitude around 14 – 20 Ma and half of the current altitude at 10 Ma (Gregory-Wodzicki 2000). This has also been discussed by Lavenu (1992), suggesting that the Andean Cordillera reached modern elevations during the Pleistocene (Lavenu 1992). During the Miocene, the Subandean fold-thrust belt formed (Fig. 3J) (Horton 2018).

It should be noted that this description of the tectonic evolution within the Central Andes is simplified due to its complex nature. The tectonic evolution changes regionally within the Andes and is not yet fully understood.

3.2.3. Bedrock geology

Rocks from the Paleozoic era, especially Ordovician rocks, dominate in the Eastern Cordillera. The Valley of Cochabamba and the surrounding area is not different. During the early Cretaceous, when the Andes started to form, the Paleozoic rocks from a marine environment were uplifted and exposed to deformation (Lavenu et al. 2000; Renner & Velasco 2000). Therefore, the rocks consist of sandstone, quartzitic siltstones, shales and in small amounts of limestone and have been exposed to various degrees of diastrophism. For this reason, Ordovician rocks can be found in contact with rocks from the Tertiary (Renner & Velasco 2000). A geological map from GEOBOL (1994) is shown in appendix A.

In general, Paleozoic rocks make up most of the bedrock surrounding the valley and are found north, east, south and to some extent southwest of the valley. West of the valley, Mesozoic and Cenozoic rocks dominate (GEOBOL 1994).

In detail, Ordovician rocks make up most of the Paleozoic bedrock and are mainly found north, east and south of the valley. Silurian rocks can be found in the south-eastern sector. To some extent they can also be found north of the valley. Devonian formations are found west and southwest of the valley. The scarce amount of limestone from the Paleozoic era was formed during the Permian and is also found west of the valley. The Cretaceous rocks make up a rather big portion of the rocks west of the valley. They consist of clays, marls, calcareous sandstone and conglomerate and crop out in a wide zone following a northwest to southeast direction. Lastly, the Tertiary rocks can also be found in the western region, mainly consisting of conglomerates and red clays (GEOBOL 1994; Renner & Velasco 2000).

3.2.4. Tertiary - Quaternary

During the Late Tertiary, the area (as in the rest of the Eastern Cordillera) experienced neotectonic movements and compressions (Lavenu 1992; Lavenu et al. 2000). Two major fault-systems formed as a result. The most important is the Tunari Fault, a normal dextral fault with an east-west direction (App. A) (Lavenu et al. 2000; Renner & Velasco 2000). Its location is in the northern part of the valley, at the base of the Tunari mountain range. The topographic difference that exists between the valley and the mountain range today is caused by this fault (SERGEOMIN; GEOBOL 1979). The second fault, the Sipe Sipe Fault, is located in the southwestern part of the valley, which is a reverse fault with a northwest-southeast direction (App. A). Due to its reverse nature, the Ordovician rocks come into contact with rocks from the Mesozoic and Cenozoic. These two fault systems created the Valley of Cochabamba. The valley is therefore a tectonic basin formed by strike slip faults (Fig. 4) (Renner & Velasco 2000; Argollo & Iriondo 2008).

At the onset of the Quaternary, the basin was an endorheic basin and the water running down from the surrounding mountains filled the basin with sediments and retained most of the water. Smaller lakes started to form, eventually merging into a single lake, covering almost all of the basin (Fig. 5a). Temperatures, climate and to some extent tectonic processes oscillated during the Quaternary, resulting in fluctuations of the size of the lake. Lacustrine and low-energy sediments, such as silt and clays, were deposited when the lake covered large areas of the basin. During periods of lower shorelines, rivers deposited fluviolacustrine sediments and coarse-grained materials. This cycle continued until the onset of the Quaternary. This alteration of deposits has given rise to heterogeneous sediments in the valley, in both lateral and vertical directions (Renner & Velasco 2000).

During the Pliocene-Pleistocene, the basin experienced tectonic movements, resulting in drainage of the basin (Fig. 5b). The cause of this drainage is still unclear. Renner& Velasco (2000) has provided the following hypothesis: A ridge extended northwest from where the village Vinto is today, towards the Tunari mountain range. Tectonic activities triggered the downfall of the ridge, ensuring the drainage of the basin and the endorheic basin ceased to exist. Recent geophysical studies in this area have supported this hypothesis (Renner & Velasco 2000).

In the mountainous zone, the Quaternary is represented by glacial formations, such as glacial shaped valleys, glacial lakes and glacial cirques and other landforms that are typical for glacial environments (SERGEOMIN). The sediments consist predominantly of till. Two generations of till have been identified, estimated to have formed 28000 years and 15000 – 10000 years ago (Renner & Velasco 2000). However, there is no evidence of glacial impact within the Valley of Cochabamba. It is assumed that the maximum extension of the glaciers did not reach below 3400 m.a.s.l. Sediments from the mountainous zone have, with time, been transported down towards the valley, creating alluvial fans. The alluvial fans are of different ages and are superimposed at the edge of the valley. Moreover, they are predominantly coarse-grained,

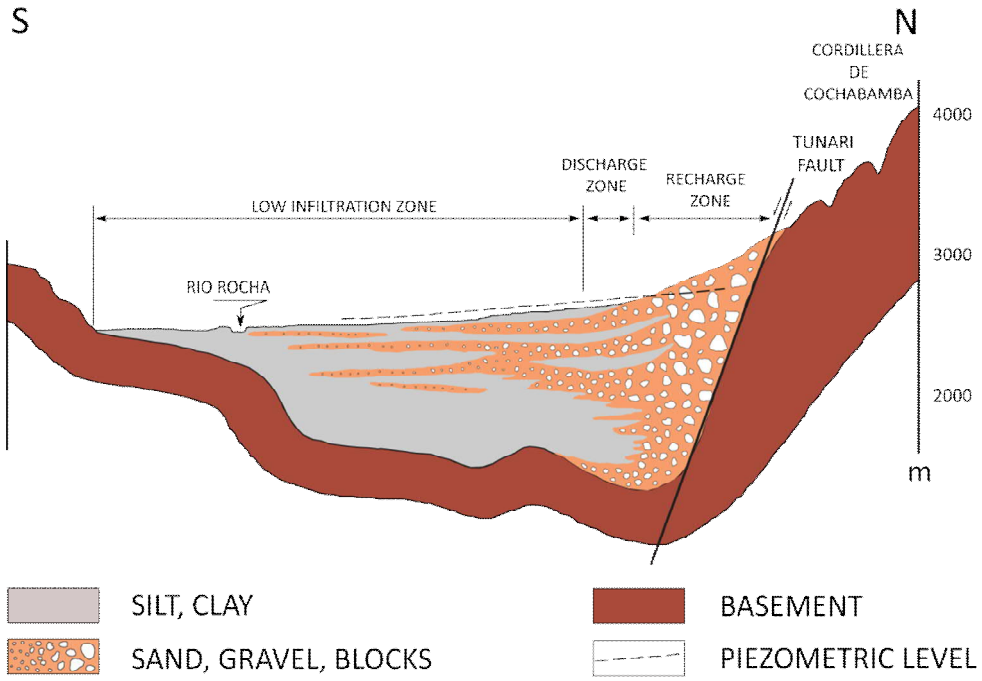

Figure 4. Cross-section of the Valley of Cochabamba from south to north. Of the two major faults in the valley, only the Tunari fault is marked since it stretches through the whole valley form west to east. The other fault, Sipe Sipe fault, is located in the south-western part of the valley. The figure is modified from Gouzes& Delpont (1990).

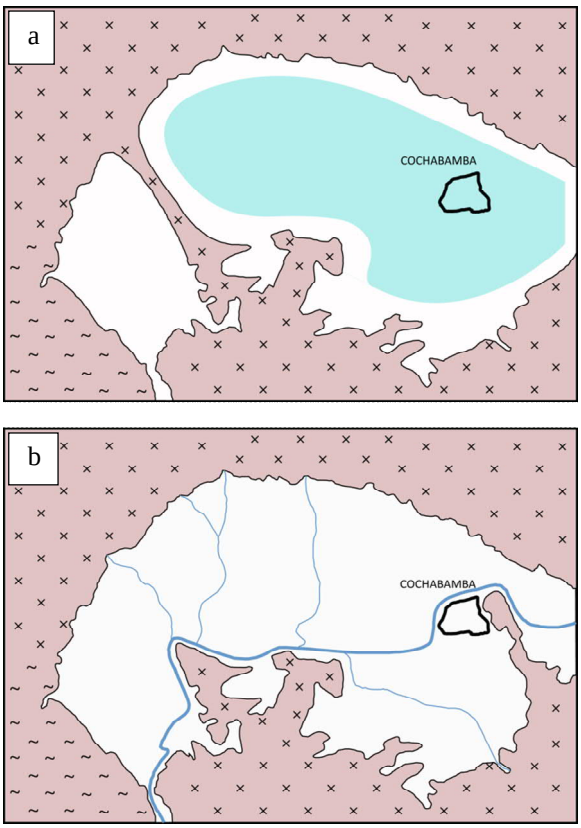

Figure 5. Tectonic evolution of the Valley of Cochabamba. (**A**) During the late Tertiary, an endorheic basin formed from streams flowing down from the mountain. (**B**) Tectonic processes caused drainage of the basin during the Pliocene-Pleistocene. Modified from Renner& Velasco (2000).

adding to the heterogeneity of the sediments in the valley. It should be noted that the general grain size of the sediments decreases from the edge of the valley towards the centre. The alluvial cones mainly contain blocks and boulders, while the centre of the valley is dominated by lacustrine and fluviolacustrine sediments, containing primarily silt and clays. Some geophysical studies have estimated the thickness of the sediments. The basement dips towards the north, leading to an estimated sediment thickness of approximately 100 m in the south to up to 1000 m in the north of the valley (Renner & Velasco 2000).

Two lithology reports from two wells were retrieved from the United Nation Development Programme (UNDP 1979). One of the wells (number 1) is located in the south-eastern part of the study area and the other (number 2) outside of the study area, also in the south-eastern part. They are approximately 700 m apart and their respective locations are shown in figure 21. The lithology report from well #1 (left in Fig. 6) has a depth of 120 m. The first few meters is made up of finer sediments (mud). Downwards to 70 m, the most abundant grain size is sand and gravel and blocks. Within this layer there are three thin layers where the grain size decreases: 29 – 36 m, 46 – 50 m and 55 – 60 m. Below 70 m the grain size becomes finer. The lithology report from well #2 (right in Fig. 6) has a depth of 105 m. The lithology generally follows the same pattern as in well #1. Mud is more frequent in the shallow part of the ground. At 5 – 97 m gravel and blocks become the main grain size. Although there is a variation of the amount of mud and sand in this layer, the layers of finer sediments seen in well #1 cannot be seen in well #2. In the bottom part,

the grain size seems to decrease. It is important to understand that the lithology generally is the same but small variations can occur over short distances.

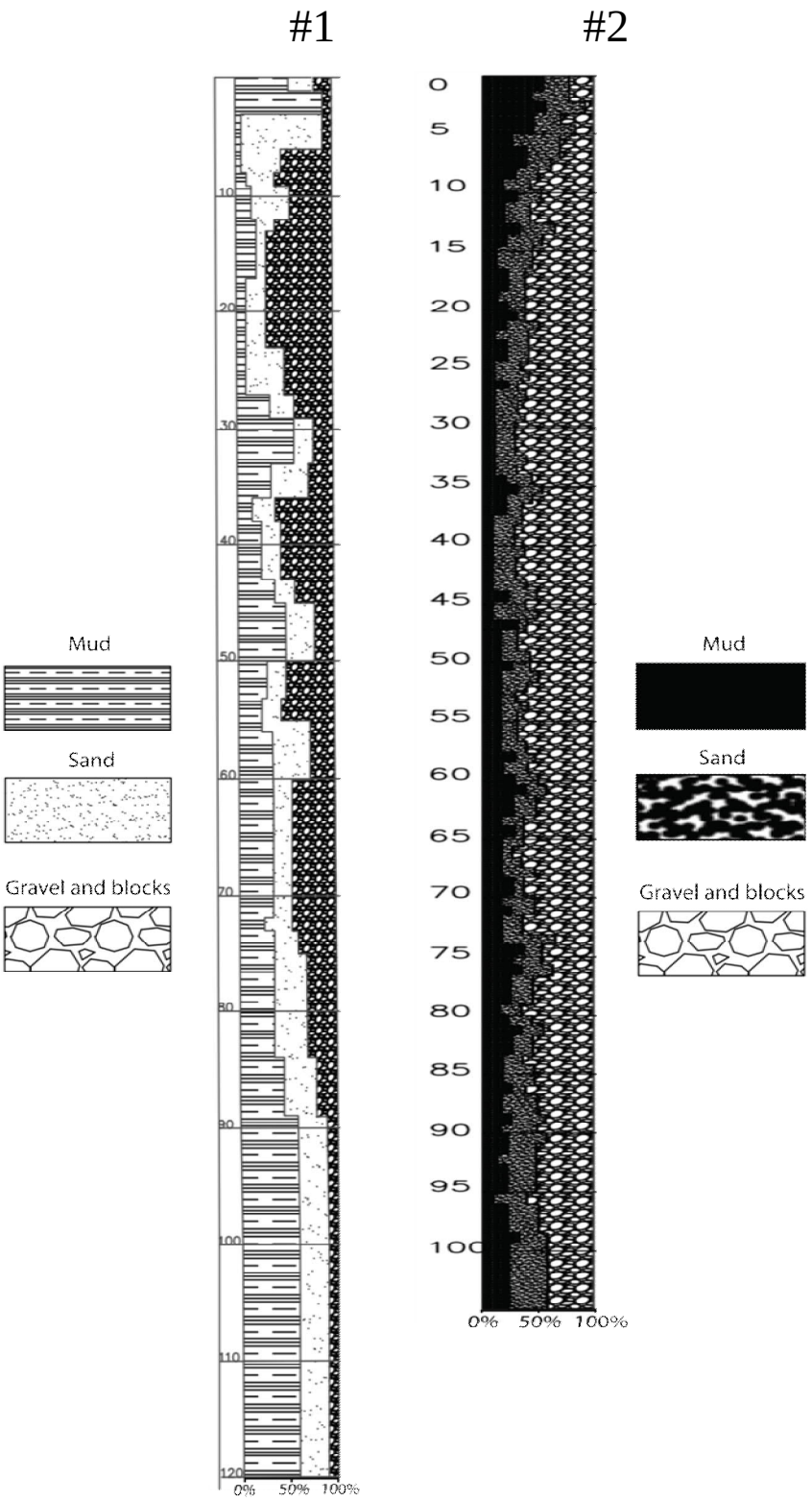

Figure 6. Lithostratigraphic well logs retreived from UNDP (1979). Their locations are marked in Fig. 21.

In the study area rocks from the river are mined and used for construction of roads. At a few places within the river the first 10 to 15 m are exposed as a result from the mining activity, revealing the sediments of the top layer of the farmland and hence, the study area (Fig. 7). The sediments have been transported and deposited by water and the grains are rounded. In general, the structure of the outcrop is massive (no structure such as lamination can be seen) and graded. It is predominantly clast supported but matrix supported at a few places. The lithofacies was determined as cobbles and gravels clast supported, CoGcm(g). The matrix is poorly sorted and the smallest grain size could not be determined exactly during the field work but is estimated to be fine sand according to the Wentworth classification (or 3 to 2 on the Phi scale). The geometry of the layers is primarily tabular and wedge shaped. At the top, where the tree is (Fig. 7), boulders have not been deposited naturally and are therefore not part of the description. The thin layer beneath could not be reached and thus not examined. If it formed from the river or as a result of farming or by other natural or human activities is not known. It is important to emphasize that the description of the outcrop (Fig. 7) has been generalized since the layers and textures can vary.

Figure 7. Picture of an outcrop of the top 10 to 15 m found in the river within the study area. It consists of rounded grains deposited by water. The grain size varies. The picture is taken facing west.

3.3. Hydrogeology

It should be noted that the knowledge and information about the hydrogeology in the valley of Cochabamba is still limited. A report of the Servicio Geológico de Bolivia (GEOBOL 1979) provides an overview of the hydrogeology in the valley. Most of the information about the hydrogeology in this thesis is retrieved from this report. However, it is important to keep in mind that it was written 40 years ago. Furthermore, a master thesis of Stimson (1991) and a report of Renner& Velasco (2000) add some further aspects about the local hydrogeology.

As mentioned in section 4.2.1, the northern and western parts of the valley are made up of alluvial fans. Within these fans the main aquifers are present and extending to the central part of the valley. It should be noted that there are other aquifers in the valley as well but at greater depths than these main aquifers. The fans have a high permeability due to their sediments mainly containing coarse grains: boulders, gravel and sand. The aquifers are limited by the Mesozoic rocks in the western part and the Paleozoic rocks in the northern part (GEOBOL 1979). Regarding the vertical limits of the aquifers, the report from GEOBOL (1979) states that the aquifers are limited by the Paleozoic basement. However, according to Stimson (1991), the deepest sediments are assumed to be clays, before making contact to the Paleozoic basement. Renner& Velasco (2000) confirmed this assumption because deep drilling in the area revealed that the lowest layers consist of fluviolacustrine sediments. In general, the Paleozoic rocks in the area are considered to be impermeable, although secondary permeability, such as fractures, can occur. The lower boundary of the aquifers is roughly south of the city Cochabamba and north of the Rocha River. This lower part consists of fluviolacustrine and lacustrine sediments (GEOBOL 1979).

The main aquifers in the upper part of the fans can be classified as unconfined aquifers. The thickness of the permeable material, although difficult to estimate, varies between 15 and 45 m, with only few and thin clay horizons (GEOBOL 1979; Stimson 1991). The hydraulic conductivity within these sediments generally decreases when transitioning from the coarse grain sizes to the fine sediments at the bottom (Renner & Velasco 2000). However, the abundance and thickness of these clay horizons increase toward the south within the aquifers. The lithology changes at the base of the fans and a transition zone (approximately where the discharge zone is) (Fig. 8) with semi-confined aquifers evolves, containing multiple layers of material with a lower permeability (clays). Here, the thickness of the permeable layers varies between 10 and 30 m. Moreover, the piezometric level is above the ground in this region and wells are of artesian nature. Near the Rocha River, fine sediments start to dominate, and the aquifers become confined to occasional sandy horizons. The permeable layers in this area decrease from 20 m to only a few cm in thickness (GEOBOL 1979).

The water table within the aquifers varies in depth throughout the Valley of Cochabamba and has been measured in numerous wells. Fluctuations of the water table can occur within the aquifers and are mainly due to rains and river water from the highlands. At

the fan zone (high recharge area) (Fig. 8), the water table can fluctuate by up to 10 m, while fluctuations are minimal in the transition zone. In the lacustrine zone the water table is affected by the rainy season and irrigation and varies by 0.5 to 2 m. In general, the water table decreases with elevation. In the north-western sector of the valley, the depth of the water table was 54 m. In the El Paso area (northern area), the depth of the water table ranged from 7 to 34 m. Within the transition zone (Fig. 8), the water table was close to the surface, varying from 0.2 to 1 m and during dry periods the water table lowered further. In the lacustrine zone (Fig. 8), the topographically lowest part, the water table fluctuated from 1 to 5 m (GEOBOL 1979). According to Stimson (1991), the depth of the water table is between 30 and 50 m in the alluvial fans. At the transition zone it varies from 2 to 10 m and at the Rocha River it is close to the surface (Stimson 1991). The allegations about the depth of the water table should the taken with caution since they were written many years ago. Today, the water table is, in general, lower. How much is has lowered is unknown, therefore monitoring campaigns of water table are needed (pers. comm. Gonzales 2019).

The groundwater flow is in general from the north to the south and towards the centre of the valley. The outflow is mainly in two areas; (1) west of the airport of Cochabamba, characterized by a swampy area and (2) in the southwestern sector of the valley (GEOBOL 1979; Renner & Velasco 2000).

The aquifers are recharged through water from rain, infiltration from the many rivers and streams that the mountain range provide and by irrigation. Recharge occurs mainly during the rainy season, from November to March. However, rivers recharge through surface flows until September, before they decrease in size and cease to exist until the next rainy season (GEOBOL 1979). The main recharge areas are in the northern and western sector where the upper alluvial fans (Fig. 8) create optimal conditions for infiltration due to their high permeability (GEOBOL 1979; Stimson 1991). Given that the annual precipitation in this zone is around 600 mm and assuming 15 to 20% infiltration of the rain, it is estimated that the aquifers are recharged with a volume of 15 to 20 ´ 10^6 m^3/year (GEOBOL 1979). Infiltration of surface flows is difficult to measure according to GEOBOL (1979), but assuming 15 to 20% infiltration of the total flow within the valley, it is estimated to add a volume of 35 to 50 ´ 10^6 m^3/year to the aquifers. Finally, infiltration by irrigation extracted by local surface water constitutes only a minor component of the volume of water that feeds the aquifers. Approximately 20% to 25% of the water used for irrigation infiltrates and the estimated volume for recharge is 3 to 5 ´ 10^6 m^3/year (GEOBOL 1979).

The discharge zone coincides with the lower portion of the alluvial fans and the transition zone (Fig. 8) (GEOBOL 1979; Stimson 1991). The direction of the groundwater flow is generally towards the

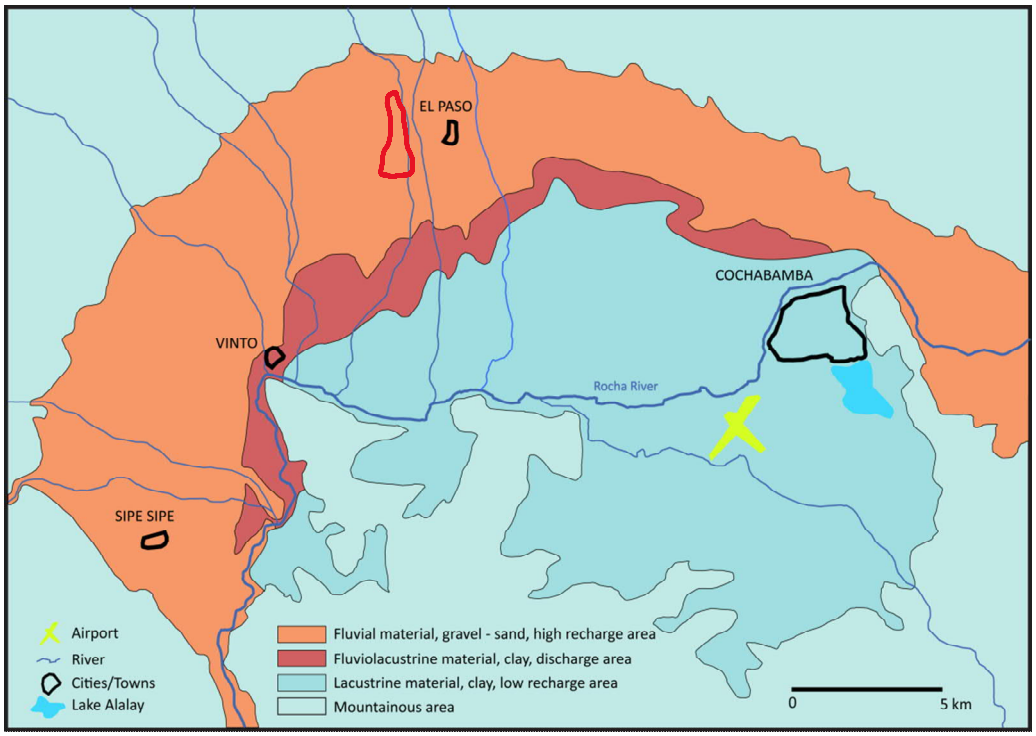

Figure 8. Recharge and discharge areas in the Valley of Cochabamba. In the recharge areas the infiltration of water is favourable. In the discharge area infiltration normally does not occur. Note that in the text, the fan zone and transition zone are used as synonyms for the recharge and discharge areas respectively. The red area in the picture roughly represent the location of the study are. The flow direction of the river is from east to west, i.e. right to left in the figure. Modified from Renner & Velasco (2000).

centre of the valley but due to the decreasing permeability, the groundwater is close to the surface and sometimes emerges (as mentioned above) and discharges into springs. Discharge of the aquifers is related to evapotranspiration, the base flow of the Rocha River, wells and springs. Considering a discharge area of approximately 30 km^2, the evapotranspiration is estimated to discharge a water volume of 13 to 15 ´ 10^6 m^3/year. Base flow from the Rocha river is estimated to discharge water with a volume of 15 to 22 ´ 10^6 m^3/year. When measuring the discharge from wells and springs, only drilled wells are used to measure and estimate the water balance of the aquifers. The estimated volume of extracted water from wells is 13 to 19 ´ 10^6 m^3/year and the discharge from springs is estimated to be 4.7 to 5.5 ´ 10^6 m^3/year (GEOBOL 1979). However, GEOBOL (1979) mentioned that the latter estimates may not be precise because of insufficient information when calculating the yearly discharge (GEOBOL 1979).

With this estimation of the recharge and discharge of the aquifers it is possible to estimate the water balance of the aquifers. This total estimation is summarized in Table 1.

Table 1. Estimated amounts of recharge and discharge from aquifers in the Valley of Cochabamba. Numbers are taken from GEOBOL (1979) and the table is modified from GEO-

Recharge, 10^6 m^3/ year		**Discharge, 10^6 m^3/year**	
Precipitation	15 – 20	Evapotranspiration	13 – 15
Surface flows	35 – 50	Base flow	15 – 22
Irrigation	3 – 5	Wells	13 – 19
		Springs	4.7 – 5.5
Total	**53 – 75**	**Total**	**45.7 – 61.5**

The factors that affect the discharge of the aquifer are difficult to measure and vary with time, especially since more and more wells are being drilled. For this reason, GEOBOL (1979) emphasized that the estimates are only tentative and that the water balance most likely will change and fluctuate in the future. Repeated measurements of the water balance are therefore encouraged (GEOBOL 1979). GEOBOL (1979) further mentioned, given the estimates of recharge and discharge, that extraction of water from the wells does not lead to depletion of the aquifer. However, this allegation referred to the situation in 1979. Since then, the number of wells and the demand of drinking water due to the increased population in the Valley of Cochabamba have increased. Today, the amount of wells and extraction of water is affecting the aquifer negatively and the discharge is possibly greater than the recharge (pers. comm. Gonzales 2019).

4. Methods

4.1. Geoelectrics

Geoelectric methods are based on transmitting a current into the ground and measuring the potential difference between electrodes in order to measure the electric property of the ground. Electrical resistivity methods were first used in the early 1900s, but their popularity increased in the 1970s when computers became powerful enough to handle the data processing and the data analysis. Today these methods are commonly used for mapping subsurface features, especially in the fields of hydrogeology, engineering and archaeology (Dahlin 2001; Reynolds 2011).

4.1.1. Theory

Resistivity is a fundamental property of materials. It is the ability of materials to resist the flow of an electrical current. Consider a cube with the length (L) and the side with an area (A). A current (I) is passing perpendicularly through one of the sides. The material of the cube will resist part of the current while it is passing through, causing a potential drop (V) when reaching the opposite side of the cube. The resistivity of the material is denoted by the Greek letter "rho" (ρ) and the SI-unit is Ohm-meter, Ωm. The opposite of resistivity is conductivity, s, and its SI-unit is Siemens/meter (S/m). A complete descriptions of the resistance, Ohm's law and resistivity is given in Reynolds (2011).

The resistance of the material is described by the following equation

$$R = \frac{\rho \cdot L}{A} \tag{1.1}$$

Another definition of resistance is described by Ohm's law

$$R = \frac{V}{I} \tag{1.2}$$

Furthermore, the potential difference (V) is the product of electric field strength, E (V/m), and distance, L (m). Also, the current (I) is the product of current density, J (A/m^2), and area, A (m^2). Equation 1.2 and resistance can therefore be rewritten as

$$R = \frac{E \cdot L}{J \cdot A} \tag{1.3}$$

Finally, given equations 1.1, 1.2 and 1.3, the resistivity of a material can be calculated through the following equations

$$\rho = \frac{R \cdot A}{L} = \frac{V \cdot A}{I \cdot L} = \frac{E}{J} \tag{1.4}$$

The basic principle of resistivity surveys is directing a current into the ground through two current electrodes (C). A potential difference emerges and the magnitude of this potential difference depends on the resistivity of the materials in the ground. Two potential elec-

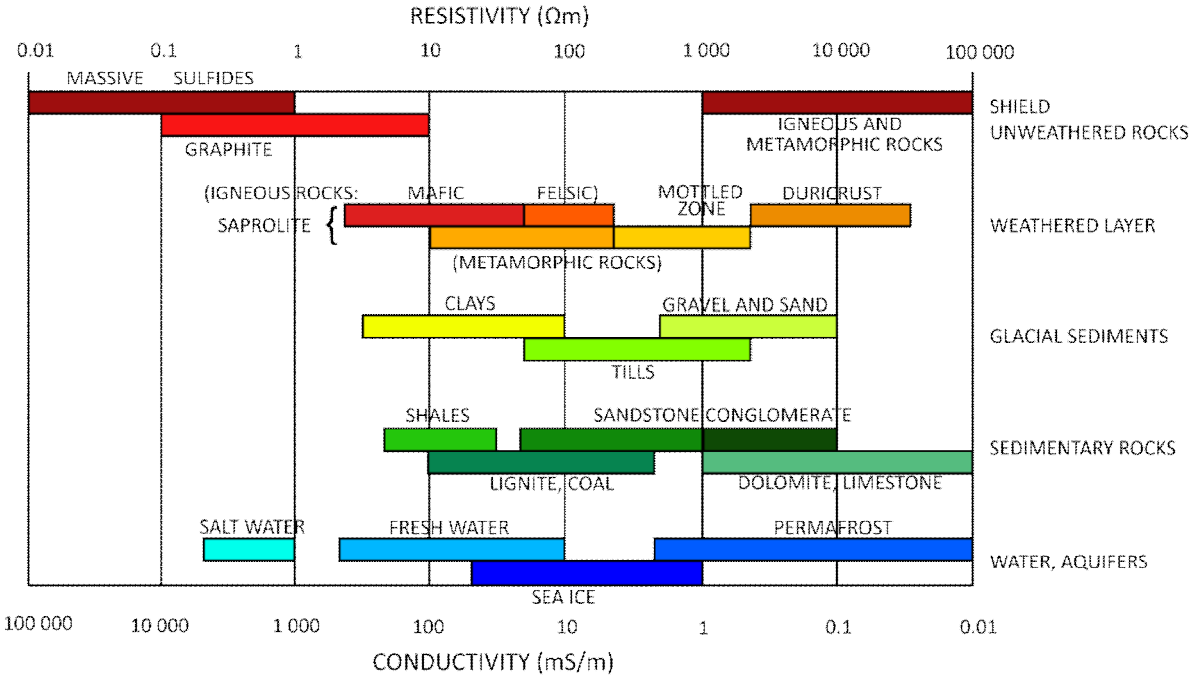

Figure 9. Resistivity and conductivity of different geological materials. The two most important categories for this thesis are resistivities for the glacial sediments and the sedimentary rocks. Modified from Palacky (1987).

trodes (P) measure this potential difference and with Ohm's law the resistance can be calculated, see equation 1.2 (Jeppsson & Dahlin 2017).

When conducting electrical resistivity methods, the resistivity of the geological formation of the subsurface is measured, i.e. the ability of the ground to resist an electrical current. Different geological formations have, in general, different resistivities (Jeppsson & Dahlin 2017). The spectrum of the resistivity of geological materials can vary between 1.6×10^{-8} and 10^{16} Ωm according to Reynolds (2011). Palacky (1987) has summarized the resistivity of common geological materials, which is presented in Fig. 9. As seen in Fig.9, the resistivity of any given geological formation can vary and different geological formations can have overlapping resistivities, sometimes making interpretations difficult. Factors affecting the resistivity of a geological formation are: porosity, the amount of liquids in the pore space, the liquid in the pore space, mud content, salinity content, fracture zones, weathering and to some degree temperature (Reynolds 2011; Jeppsson & Dahlin 2017). The geoelectric method used during the field work was the Electrical Resistivity Tomography (ERT) see section 5.3.1.

4.1.2. Current diffusion patterns

Given a homogenous material and a simple electrode setup, the current spreads radially into the material. The current density spreads according to a hemisphere and therefore loses its density away from the original source (Fig. 10A) (Reynolds 2011). For several electrodes aligned, the current diffusion pattern would be as illustrated in Fig. 10B and 10C.

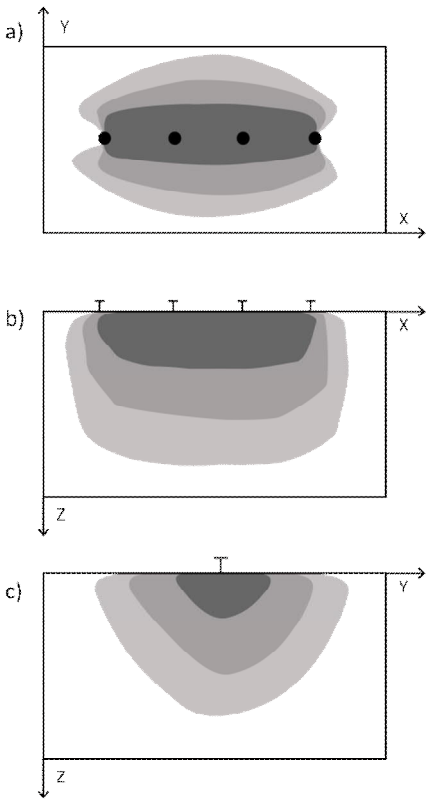

Figure 10. Current diffusion patterns for given homogenous ground and a simple electrode setup. The current spreads according to a hemisphere and loses its strength further away from the source. (**A**) seen from the z-axis. (**B**) seen from the y-axis. (**C**) seen from the x-axis. Taken from Jeppsson& Dahlin (2017).

4.1.3. Apparent resistivity

If all the measured materials were homogenous, the measured resistivity would be the real resistivity and interpretations could be done. However, this situation never occurs in the field and the resistivity measured which is an average of the heterogeneous material. This resistivity is called apparent resistivity and should never be used for interpretation. In order to retrieve the real resistivity of the material a so-called inversion process has to be made (Jeppsson & Dahlin 2017). This can be done by a computer programs. In this thesis the program RES2DINV was used. More about inversion will be discussed in section 5.4.

4.1.4. Penetration depth

The penetration depth of resistivity surveys depends on the distance between the electrodes, the used array and the resistivity of the layers. A rule of thumb is that the penetration depth increases with the increase of distance between the current electrodes and the potential electrodes. This applies for all types of arrays. The penetration depth further depends on the array used. Some arrays have a greater penetration depth than other. The current that is sent out is concentrated in materials with lower resistivity. If layers with low resistivity occur at shallow depths, the penetration depth will decrease as opposed to low resistivity layers located deeper within the ground (Jeppsson & Dahlin 2017).

4.1.5. The Schlumberger array

When performing resistivity surveys there are several arrays to choose from. The three most popular are the Wenner, Schlumberger and Dipole-dipole arrays. These arrays in turn have variants of themselves. All methods have advantages and disadvantages depending on the objective of the survey. Table 2 summarizes the most important features and how they differ between these three arrays.

Table 2. Comparing different characteristics of the three most common arrays. Modified from Reynolds (2011).

Criteria	Wenner	Schlumberger	Dipole-dipole
Vertical resolu-	· · ·	· ·	·
Depth penetra-	·	· ·	· · ·
Insensitivity to	· · ·	· ·	·
· · · = good, · · = moderate, · = poor			

For this work, a variant of the Schlumberger array was used because this array renders a moderate vertical resolution and penetration depth, both of which are desired for this study. The variant of the Schlumberger array that was used is called gradient. It is an asymmetric variant of the Schlumberger array allowing two potential electrodes (P) to be placed wherever between two current electrodes (C).

4.2. Electromagnetics

An electromagnetic wave is energy (W/m^2) containing an electric and a magnetic component that are perpendicular to each other and vary with time (Fig. 11) (Jeppsson 2017). They are described by Maxwell's equations. Christiansen et al. (2009) describe this phenomenon in more detail. The waves can either be periodic or transient. The former refers to a wave with a given frequency, period, wavelength and velocity. The latter has a period that is infinite and is therefore not repetitive (Fig. 11) (Jeppsson 2017). The formation of an electromagnetic wave is also described by Maxwell's equations. They prove that a time-varying electric field give rise to a time-varying magnetic field and vice versa. Hence, in order to create an electromagnetic wave, only either a magnetic or and electric wave needs to be created (Jeppsson 2017).

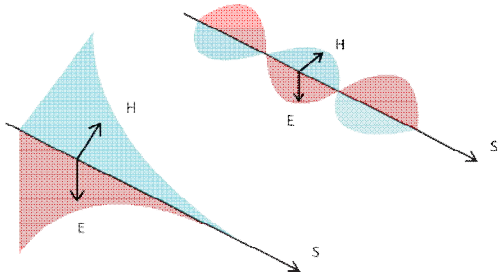

Figure 11. Transient (left) and periodic (right) electromagnetic waves. The difference between the two is that the periodic wave has a frequency, period, wavelength and velocity, whereas the transient wave does not have a period. Modified from Jeppsson (2017).

Electromagnetic methods can be divided into two main groups: induction methods and reflection methods. The induction methods use low frequencies, 1 – 100 000 Hz, where the primary waves induce secondary electromagnetic waves. Reflection methods use higher frequencies, 1Mhz – 1GHz, where the waves are reflected at the boundary between two geological layers. The sources for the electromagnetic methods can be divided into artificial and natural sources, the latter being applied less. When performing electromagnetic measurements, two kinds of waves can be used: periodic (repetitive) waves or transient (non-repetitive) waves (Fig. 11) (Jeppsson 2017).

Electromagnetic methods use electromagnetic waves that vary with time. A primary wave is sent into the ground. The ground acts as a conductor and induces an electrical current into the surrounding material. A secondary wave is formed as a consequence, that in turn creates other waves, and so on. Equipment at the surface registers these waves, which provide information about the conductivity in the ground. It is therefore possible to measure the electric and magnetic properties of sediments and bedrock with electromagnetic methods. Examples of these properties are electric conductivity (mS/m), magnetic susceptibility (k) and resistivity (Ωm) (Christiansen et al. 2009; Jeppsson 2017).

The Transient Electromagnetic Method (TEM) was used in the fieldwork for this thesis. Transient

waves are sent into the ground and the data are registered as a function of time. This is an induction method that uses an artificial source to create transient waves (Christiansen et al. 2009; Reynolds 2011; Jeppsson 2017). The method was developed in the 1980s, making it a "young" method in comparison to other electromagnetic methods. Its late development is due to the need for advanced electronic equipment and computers, which have become better and more accessible in recent years. For the last two decades this method has been used more frequently for hydrogeological purposes, despite being developed for mineral and ore investigations. The downside of using it for hydrogeological purposes is that the response of the hydrogeological formations does not differ much from background responses. Therefore, small error percentages are desired (Christiansen et al. 2009).

4.2.1. Theory

The physical phenomena behind the TEM are described by Maxwell's equations. When performing a TEM survey, a direct current (DC) is turned on ("Turn-on") (Fig. 12A) and passed through an ungrounded receiver loop. A constant (primary) magnetic field is created in the process. The current is then sharply suspended and marks the end of the "On-time" (Fig. 12B). This causes an electromotive force (emf) to induce in conductors in the ground according to Faraday's law during the "Turn-off". The magnitude of the emf depends on how fast the magnetic field changes. A rapid change will create an emf of larger magnitude than a slow change in the magnetic field. Therefore, it is of interest to turn the DC current off as quickly as possible. The emf will induce so-called eddy currents in the existing conductors in the ground. These currents will decay while moving through the conductor and produce a secondary magnetic field during the "Off-time" (Fig. 12C). This secondary magnetic field will reflect the shape, size and conductivity of the conductor when it is measured by a receiver coil. It should be noted that the primary magnetic field is absent during the "Off-time", when the measurements are taking place. Measurements are done in cycles and time intervals, so called gates (Fig. 12C). These gates are arranged with a logarithmically increasing time between the measurements in order to improve the signal-to-noise (S/N) ratio during late measurements (Mcneill 1980; Christiansen et al. 2009; Reynolds 2011). Information about the resistivity at greater depth is obtained by measuring the secondary fields as a function of time (Reynolds 2011). A normal measurement is made up of 1 000 – 10 000 pulses (transients) that are sent out during each sounding. After each pulse the current shifts direction (Fig. 12A). Normal times for the pulses are 50 – 200 ms "Turn-on" time, with a total "On-time" of 1 – 40 ms. "Turn-off" time is typically 1 – 30 ms and 1 – 40 ms "Off-time" (Christiansen et al. 2009).

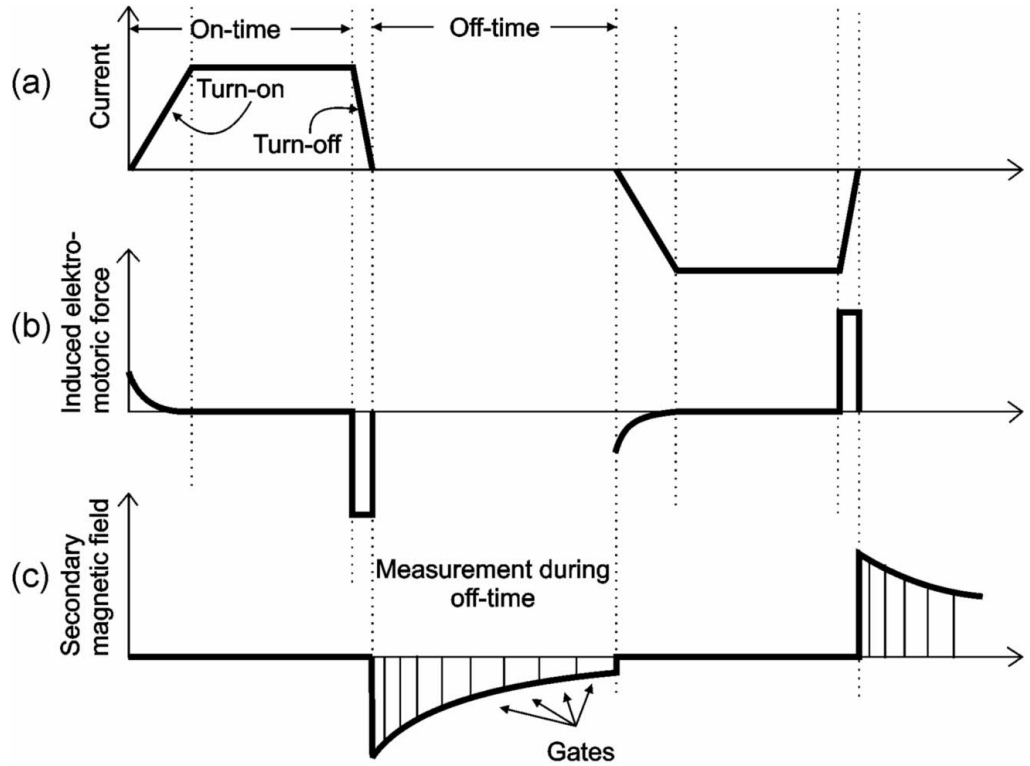

Figure 12. Theory behind a TEM measurement. (**A**) A current is turned on and is marked by the "turn-on" time until it reaches its highest value. The current is then turned off. A quick "turn-off" time is desired. This process is repeated, and the current is shifted each time. (**B**) An induced electromotoric force (emf) is created and its magnitude is dependent on the "turn-off" time. A rapid "turn-off" time will yield a greater emf. (**C**) The emf induces eddy currents in existing conductors in the ground. Their shape, size and conductivity are reflected by the secondary magnetic field that they create. Measurements are done with so-called gates that are arranged in a logarithmically increasing time between each other. Taken from Christiansen et al. (2009).

The use of dual moment is applied for the TEM. Dual moment means that all transients during the measurement consist of so-called high moment (HM) and low moment (LM). The HM transmits a current of 16 A in the receiver loop and generates a strong emf and thereby a large penetration depth. However, the turn-off time for the HM is longer and results in a poor signal quality for early gates (but not late gates) since the current will not fade completely during the turn-off time. The LM transmits a lower current of 2 A in the receiver loop. This will generate a weak emf that will have a quick turn-off time and therefore a lower penetration depth. The quick turn-off time will allow a good signal quality for early gates and therefore accounts for the lost data from the HM. Since the method is a function of time, the LM obtains data at shallow depths and the HM at greater depths (Fig. 13). Combining the HM and LM will assemble a continuous depth profile of the resistivity (Danielsen et al. 2003).

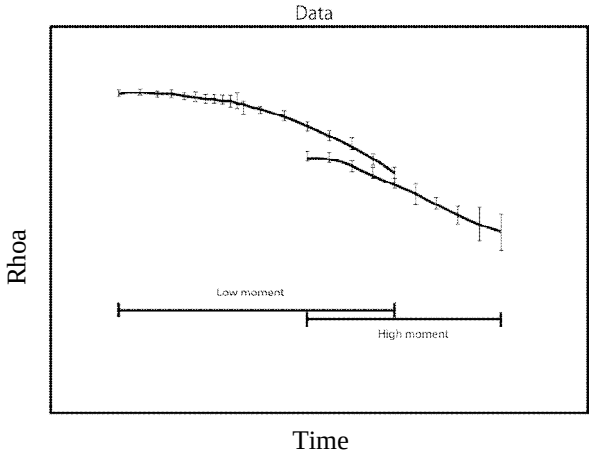

Figure 13. Theory behind a TEM measurement. A TEM measurement uses dual moments, meaning a measurement is made up of a so-called high moment (HM) and a low moment (LM). The HM uses a current of 16A, enabling measurements at greater depth. The LM uses a 2A current instead, enabling measurements at shallower

4.2.2. Current diffusion patterns

When the DC is turned off, it will disperse outwards and downwards. The movement will be at a 30° angle in relation to the ground, i.e. it will move further outwards than downwards. Fig. 14 (left) is a simplified representation of the spread and direction of the current density at three different times (10 ms, 100 ms and 1000 ms) after the DC current is switched off. Fig. 14 (left) represents a homogenous ground and Fig. 14 (right) a layered ground with different resistivities. Decay rates depend on the resistivity of the layers in the ground. Higher resistivity will cause the current to decay more quickly, whereas lower resistivities will keep the current for a longer period of time and provide more information about the layer. In Fig. 14 (right) the layers have resistivities of 30, 100 and 10 Ωm from the top to the bottom. At first the density is congregating at the top layer but will then directly jump to the lowest layer due to the low resistivity and only a fraction of the current density will be in the middle layer. This will result in little information on the middle layer (Christiansen et al. 2009).

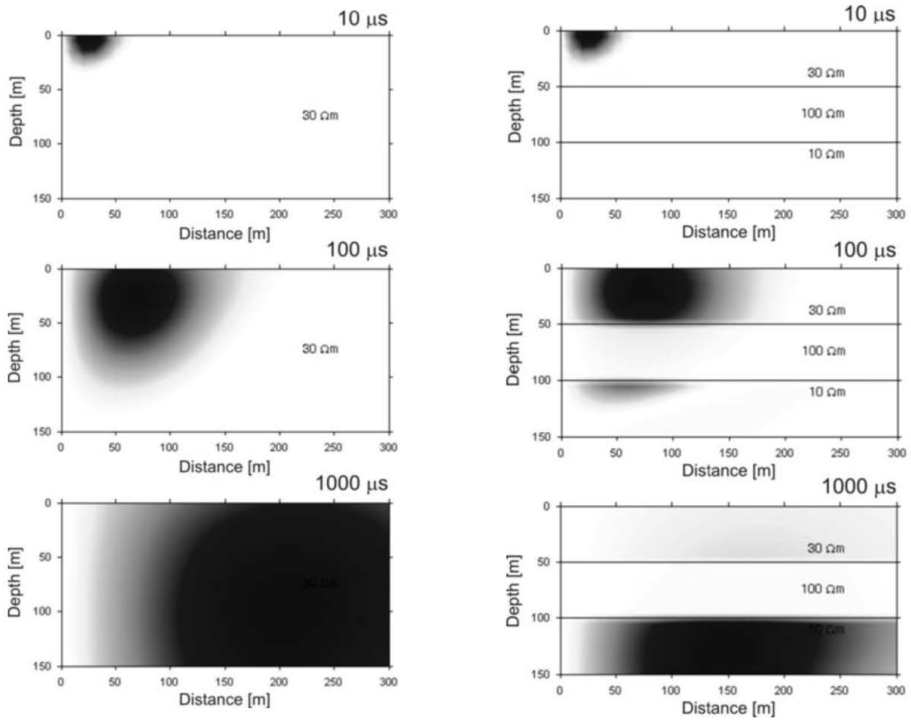

Figure 14. Illustration of spread and direction of current density at three different times and two different scenarios: homogenous ground (left) and heterogenous ground (right). In the homogenous ground the current density spreads outwards and downwards. In the heterogenous ground the current moves in the same direction as in the homogenous ground but will concentrate in layers of lower resistivity since the current decays faster in layers of

4.2.3. Noise and resolution

Data points always have an uncertainty due to background noise. For this reason, a TEM sounding has 1 000 – 10 000 pulses (transients) because a single pulse often is affected by background noise. By making many pulses, the pulses can be stacked and background noise can be accounted for. Fig. 15 represents two different TEM sounding, one with 50 transients and the other with 5 000 transients. From the figure it is obvious that the measurement containing 5 000 transients is easier to interpret. It is assumed that the noise follows a Gaussian (normal) distribution and the S/N ratio is proportional to ÖN, where N is the number of pulses in the measurement (Christiansen et al. 2009).

Noise can originate naturally from lightening that can travel large distances and from fluctuations of the Earth's magnetic field. The latter have virtually no influence on the equipment. Electricity supplies, electric installations and communication equipment can also generate noise (Christiansen et al. 2009).

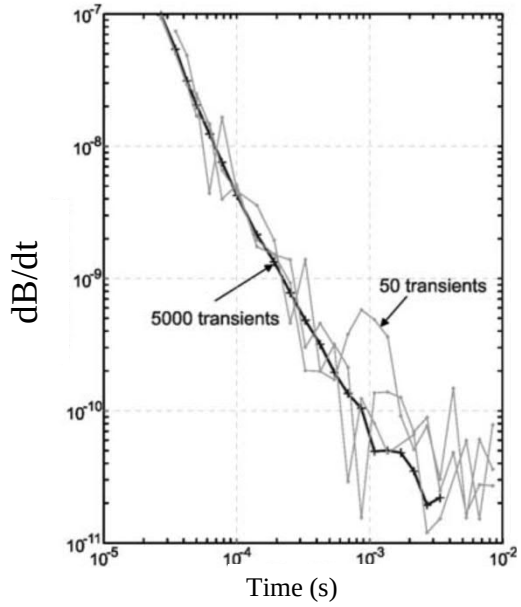

Figure 15. Illustration of the difference between a TEM sounding consisting 50 and 5000 transients. The latter yields a more accurate graph, making interpretation easier. Taken from (Christiansen et al. 2009).

4.2.4. Penetration depth

When calculating penetration depths with geophysical methods, uncertainties can be high, depending on characteristics and geometry of the layers in the ground. Equation 1.5 can be used for calculating the maximum penetration/diffusion depth for TEM soundings,

$$z_d = 0.551 \left(\frac{M}{\sigma V_{noise}} \right)^{1/5} \qquad (1.5)$$

where M is the moment of the current loop, s the conductivity and V_{noise} the noise level. The equation shows that for increasing or decreasing penetration depth, the moment of the current loop and the noise level would have to be increased or decreased respectively (Christiansen et al. 2009).

Two receiver loops (RC-5 and RC-200) with different sizes were used (see section 5.3.2). The difference in size of the loops generates different penetration depths. The bigger loop has a greater penetration depth. The LM in the RC-5 will therefore obtain data at shallow depth and the HM at medium depth. The LM in the RC-200 will also obtain data at medium depth and the HM at greater depth.

4.2.5. Coupling effects

Coupling noise is another form of noise that can affect the data. Christiansen et al. (2009) describe this as an effect of man-made conductors. It originates from pipelines, cables, power lines, rail, metal fences and cars. If these conductors are too close to the measurement site, they disturb the transmitted electromagnetic field during measurements. These effects are difficult to remove, and the interpretation of the data will probably be faulty. The minimum recommended distance from these mentioned conductors is 100 m (Christiansen et al. 2009).

These man-made conductors can be classified as galvanic and capacitive couplings (Fig. 16). Galvanic coupling is essentially a R-L circuit, a circuit consisting of a resistor (R) and an inductor (L) (Fig. 16, left). It can originate from e.g. power lines, metallic fences and crash barriers. When interpreting data, galvanic coupling is difficult to identify because the sounding curve is only shifted with an exponential decay and the curve has no major outliers (Fig. 16, left). Due to this effect, data can easily be misinterpreted as low resistive layers. The only way to identify such a coupling is to compare data with data at nearby points. Capacitive coupling is essentially a R-L-C circuit, a circuit consisting of a resistor (R), an inductor (L) and a capacitor (C) (Fig. 16, right). It can originate from e.g. isolated/buried cables. If the data are affected by capacitive coupling it can be relatively easily recognized because the decay has a saw-tooth shaped pattern (Fig. 16, right) (Danielsen et al. 2003; Christiansen et al. 2009).

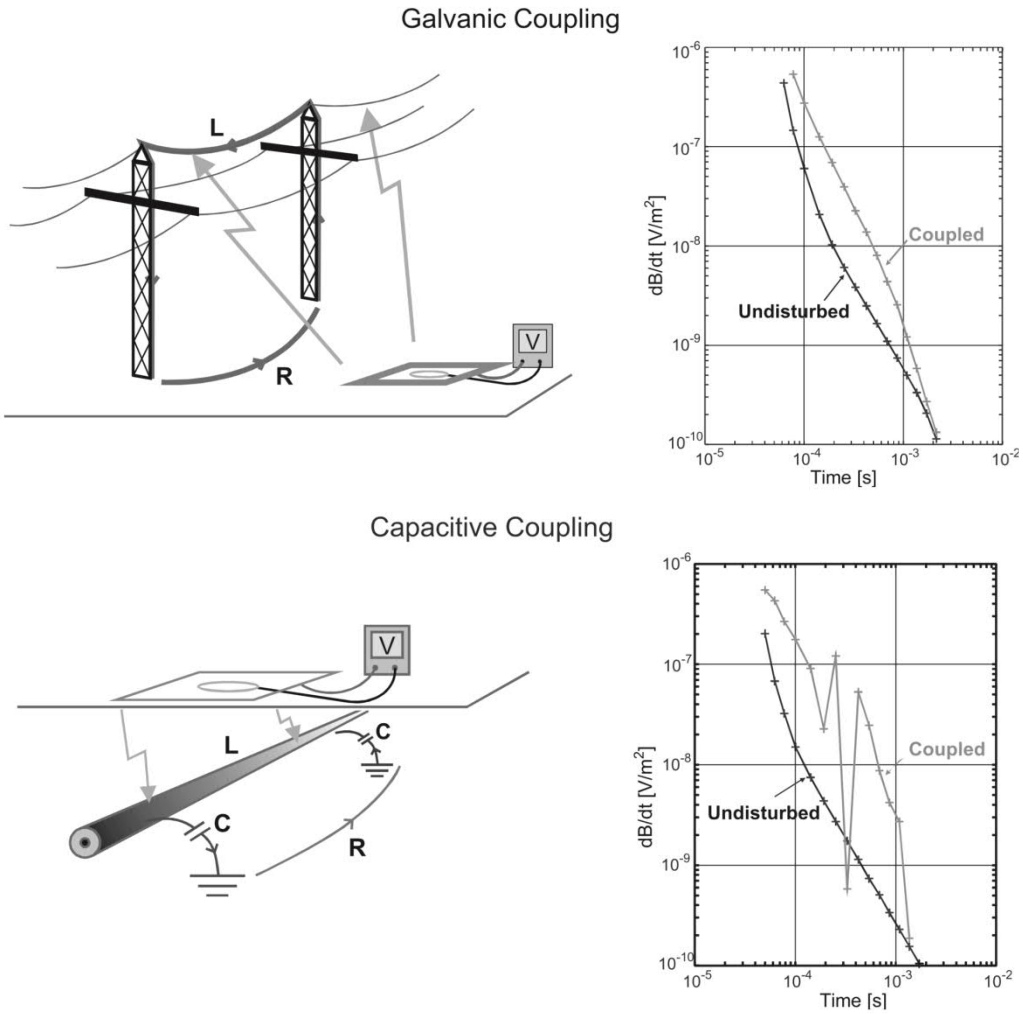

Figure 16. Galvanic coupling (left) and capacitive coupling (right). Both coupling effects can affect the data. Galvanic coupling is the more difficult to identify of the two since the curve is only shifted. Capacitive coupling can easily be identified due to its saw-tooth shape. Taken from (Christiansen et al. 2009).

4.3. Field methodology

The fieldwork was done in the Chocaya Basin (Fig. 1) in August and September 2019. As mentioned, two geophysical methods were used: TEM and ERT. Fieldwork was performed three days per week, with a total of 8 weeks. Every week, an update of the tentative plan was made for the TEM and ERT locations.

4.3.1. ERT

Equipment and applications used for the ERT measurements:

- A Terrameter LS with an integrated PC by ABEM.
- Four cable wheels, each 200 m long cable with 21 sockets each for connecting the electrodes.
- 64 electrodes.
- 64 cable jumpers to connect the electrodes to the sockets from the cable wheel.
- Two cable joints to connect the cable wheels with each other.
- One 12V battery that connects with the Terrameter LS.
- A GPS to mark differences in altitude when the terrain had varying topography. It was also used for assuring the cable was laid out as straight as possible.
- A hammer for fastening the electrodes in the ground.

The ERT method is not sensitive to coupling effects like the TEM. Metal fences and powerlines did therefore not have to be taken into consideration when choosing the location for performing the ERT measurements. The step-by-step instructions to set up the ERT-configuration were as follows:

1. Choosing an appropriate area as close as possible to the planned location for rolling out the cable wheel.

2. Two people start rolling out the wheel in a straight line. Two people are needed due to the weight of one cable wheel. Four wheels are rolled out. When rolling out a new cable wheel, an overlap of the cables was done: the first socket of the new cable was placed next to the last socket of the already rolled out cable. The end of each 200 m cable was then connected with a cable joint.

3. Two other people start hammering in the electrodes in the ground where the sockets are on the rolled-out cable. The distance between these sockets is 10 m. The electrodes are then connected with the cable by the cable jumpers.

4. The Terrameter LS is connected to the cable in the middle of the configuration, i.e. two cables of 200 m on either side of the Terrameter LS. The battery is also connected to the Terrameter LS.

5. The last step was to turn "on" the Terrameter LS and to start taking the measurements.

The Terrameter LS has the option to confirm that all electrodes are connected properly or do not have good contact with the ground. Before every measurement, this was checked. There were always electrodes that fell in either of the two just mentioned categories. This was often the case within the Chocaya River since the sediments consist of gravel and boulders. The best contact with the ground is when the sediments are more fine grained, which they were on the farm land. These electrodes were then adjusted and checked by the Terrameter LS again. If there still were electrodes that were not connected or had bad contact with the ground after several tests, they were discarded from the measurement. This was done with another option of the Terrameter LS.

The Terrameter LS was configured for the desired purposes. The most important configurations were the spread, the protocol, the spacing of the electrodes and the measure mode, which were set to 4 ´ 21, Gradient, 10 m and "RES, IP", respectively.

The use of multiple electrodes along a straight line (Fig. 17A) with the gradient array is called multielectrode gradient surveying. Once the measurement starts, the Terrameter LS controls which electrodes are being used for measurements. Each measurement consists of two chosen current electrodes (C) and two chosen potential electrodes (P) (Fig. 17B). After the measurement is done, two other current electrodes and potential electrodes are chosen by the instrument (Fig. 17C). This process is repeated with different spacing and combination between the current and potential electrodes for reaching different depths in the ground (Fig. 17D and 17E). Further, the whole measurement is divided into two steps. The first step uses all the cable wheels but only every second electrode in order to obtain data at greater depth. The second step uses only the two cables situated in the middle but uses all the electrodes in order to obtain data from more shallow depth. One whole measurement consists of many hundreds of measurements and normally takes between 30 and 90 minutes to complete depending if all electrodes were active of if some had to be discarded due to reasons mentioned above. The obtained data consists of apparent resistivity that is graphically represented in a so-called pseudosection. These data (pseudosections) should not be used for interpretation since they only show apparent resistivity (see section 5.1.3) (Jeppsson & Dahlin 2017). In order to be able to interpret the data, an inversion has to be made. This is done by the computer program RES2DINV. This will be discussed in section 5.4.

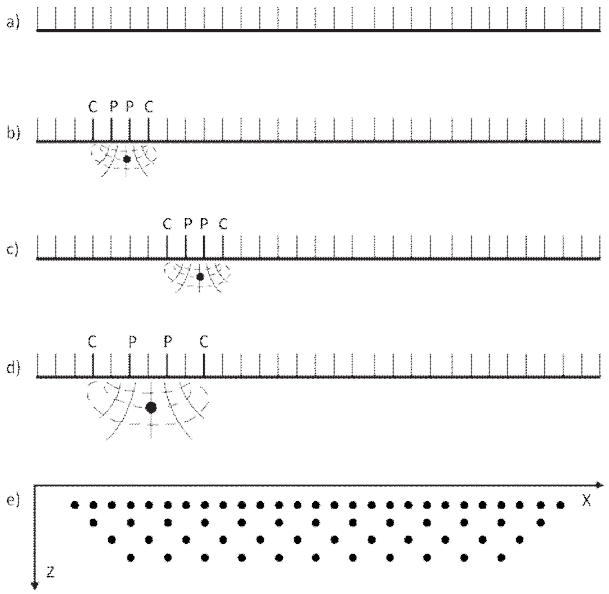

Figure 17. (**A**) the ERT electrodes are set up in a straight line. (**B**) During the measurement the Terrameter LS regulates which electrodes are used as current electrodes (C) and which electrodes are used as potential electrodes (P). (**C**) Two new C and P electrodes are chosen to perform another measurement. (**D**) The distance between the C and P electrodes increased to obtain measurements from deeper parts of the ground. (**E**) Schematic illustration of all the locations and depths of the measurements obtained during measurements with the Terrameter LS. Modified from Jeppsson& Dahlin (2017).

For one of the ERT measurements that were performed (line 6), a technique called "roll-along" (Fig. 18) was used. It is used when the desired measurement exceeds the length of the available length of the cable wheels, which was 800 m in this case. The ERT line is approximately 2000 m long. The setup is the same as described above (Fig. 18 A and 18B). The difference is when the measurement is finished. Instead of rolling in all the cables and removing all the electrodes, only one of the four cables (cable 1) is rolled in and the electrodes removed. Cable 1 is then moved and rolled out next to cable 4. Cable 1 thus becomes cable 5 (Fig. 18 C). The Terrameter LS is also moved in order to be placed in the middle of the new setup. A new measurement is carried out. This procedure is repeated until the desired length of the ERT profile is obtained.

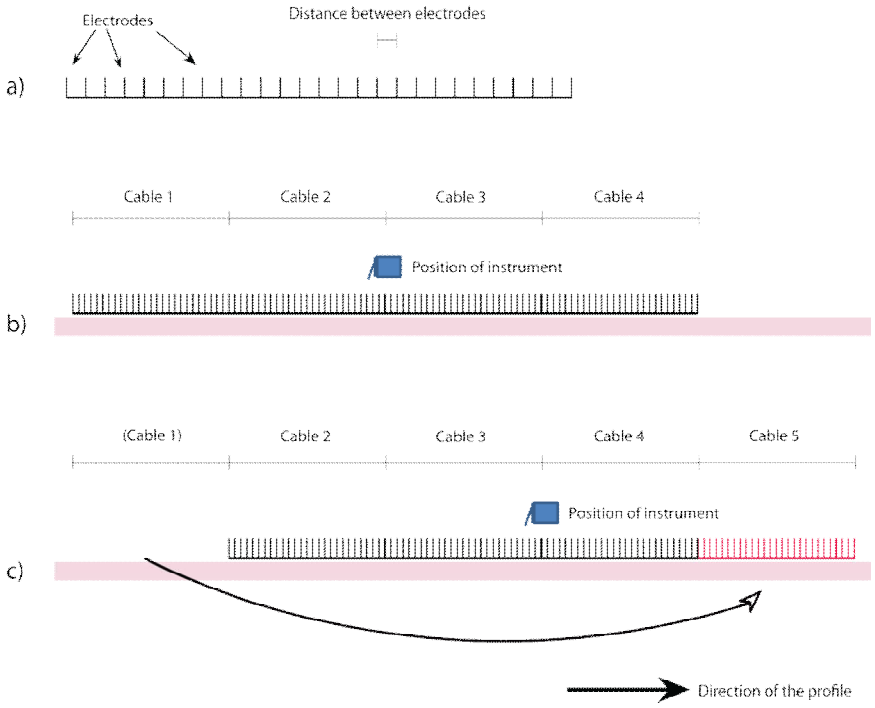

Figure 18. Roll-along technique. (**A**) Electrodes are set up in a straight line. (**B**) The line of electrodes is 800 m long consisting of four cables, each 200 m long. Measurement is started with the instrument in the middle. How the measurement is done is described in figure 17. (**C**) After the measurement is complete, cable 1 (with all the electrodes) is moved and connected to cable 4. Cable 1 becomes cable 5. The instrument is moved according to the picture. A new measurement is made. This process continues until the desired length of the line is reached. Modified from Jeppsson& Dahlin (2017).

4.3.2. TEM

Equipment and applications used for the TEM measurements:

- A WalkTEM with an integrated PC by ABEM.
- A 200 m transmitter cord laid out in a square shape of 50 × 50 m.
- Two receiver loops: RC-5 and RC-200. The RC-5 receiver is a square of approximately 0.5 × 0.5 m. The RC-200 receiver is a 40 m long cord that was laid out in a square shape of 10 × 10 m.
- An external power source of two 12V batteries.
- A 330 Ohm damping resistor.
- Cables connecting the batteries with the WalkTEM and the transmitter.
- A foldable measuring stick for checking the required distances for the setup.
- The application “Google Maps” on an iPhone 6s was used for marking the locations of the measurements.
- The application “Compass” on an iPhone 6s to ensure the RC-200 receiver was parallel to the transmitter when using the “Offset” setup (see below for more details).

A 200 m separation between each measurement was envisaged. When needed, the tentative plan was adapted during the field work. Keeping the minimum 100 m distance from man-made conductors in mind, some measurements had to be cancelled or were moved depending on the proximity of power lines, metal fences, houses and metal trash found in the field. In some cases, measurements were performed despite the proximity to power cables and possible coupling effects were marked in the notes (App. B) of those measurement points.

Depending on nearby power lines and metal objects, two different setups were used; the “Centre-loop” or the “Offset” (Fig. 19). The difference between the two setups is that the RC-200 receiver is inside the transmitter-loop in the “Centre-loop” setup and outside the transmitter-loop in the “Offset” configuration (Fig. 19). When possible, the “Offset” setup was used because the RC-200 receiver coil can affect the RC-5 receiver coil during measurement times when using the “Centre-loop” setup (pers. comm. Gonzales 2019). Appendix B shows which points were done with the “Offset” and “Centre-loop” configuration and a short comment if they had powerlines, metal objects etc. near them or not.

The step-by-step instructions to set up the “Offset” configuration were as follows:

1. Placing the equipment as close as possible to the planned location. The RC-5 receiver coil was placed on the spot and was marked on Google Maps. The cable from the RC-5 receiver coil was unravelled in the direction of one its corners. Comments on the surrounding and the type of setup used for the specific measurement were noted.

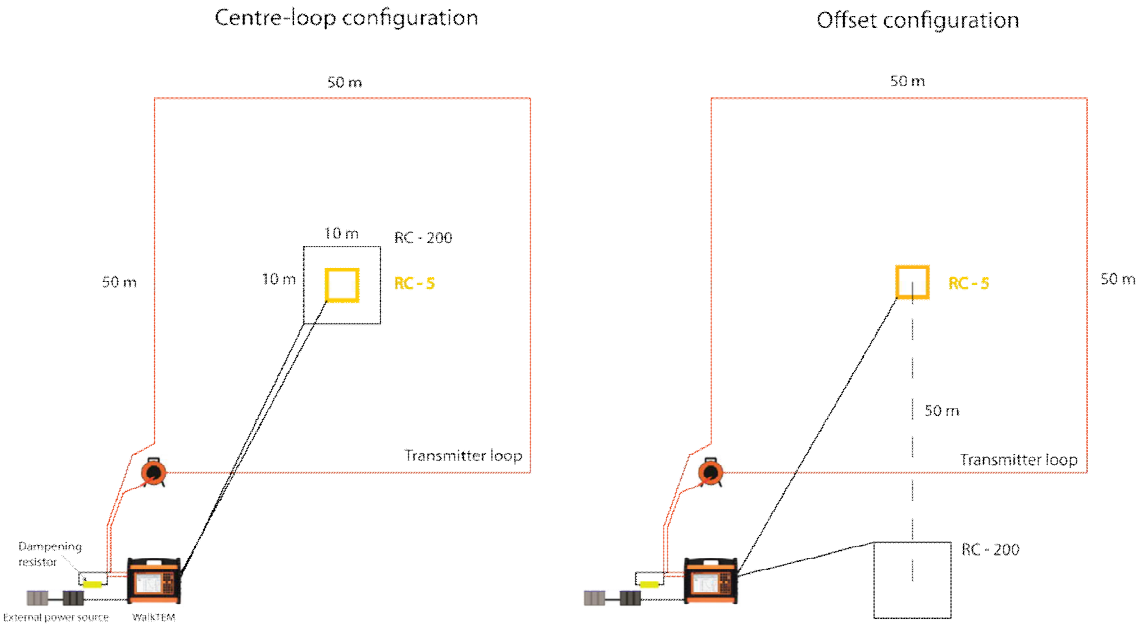

Figure 19. Illustration of the setup of the two loop configurations: center-loop (left) and offset loop (right). The only difference between the two configurations is that the RC-200 loop is outside of the transmitter loop in the offset loop configuration. Modified from ABEM (2019).

2. With the measuring tape, the corners of the transmitter loop were measured from the RC-5 receiver coil. The corners were marked on the soil. The distance from one corner to the centre is 35.36 m, half the distance of the hypotenuse of a 50 ´ 50 m square.

3. The start and end point of the transmitter cable was the corner were the cable of the RC-5 receiver coil was located. Then the transmitter cable was unravelled along the marked points.

4. The transmitter cable was put straight to a square as far as possible by persons pulling at each corner of the square.

5. The RC-200 receiver coil has then to be put outside of the transmitter loop (Fig. 19), 50 m from the centre of the RC-5 receiver coil and perpendicular to the sides. The 50 m mark represents the centre of the RC-200 receiver coil. This spot was marked.

6. Setup of the RC-200 receiver loop: A distance of 5 m was measured from the marked spot (see point 5) in the direction of the RC-5 receiver coil. From that marked spot, two people went 5 m in opposite direction, parallel to the sides of the transmitter loop. A compass was used to ensure that the sides of the RC-200 receiver coil and the transmitter loop were parallel. The corners were marked. This process was repeated for the other corners. Afterwards, the RC-200 receiver cable was setup to a square in the same manner as described in point 4. When using the other "Centre-loop" setup, the same steps were taken but the RC-200 receiver was put around the RC-5 receiver coil, inside the transmitter loop.

7. The RC-200 receiver coil was connected with a connector cable to the WalkTEM in the Input B. The cable of the RC-5 receiver coil (input A), batteries (in series), the dampening resistor and the transmitter loop were also connected to the WalkTEM.

8. The last step was to turn "on" the WalkTEM and to start taking the measurements.

The script of the WalkTEM was set to "DualMoment_10ms_32gates" and the number of cycles was set to five. The measurements therefore used HM and LM and the 10 ms and 32 gates mean that the "Turn-off" time for the current is 10 ms and 32 measurements is done during each "Off-time". The number of cycles mean that the measurement was done five times. The configuration of the loop-type was set to "50 ´ 50m_24V". This means that the WalkTEM is set to measure the RC-200 transmitter loop that is a square with 50 m on each side and the external power source was 24 V (two batteries, each 12 V).

Two receiver loops (RC-5 and RC-200) were used as mentioned. The difference in size of the loops generates different penetration depths. The bigger receiver loop has a greater penetration depth. The LM in the RC-5 will therefore obtain data at shallow depth and the HM at medium depth. The LM in the RC-200 will also obtain data at medium depth and the HM at greater depth (pers. comm. Gonzales 2019). The total measurement time was between 6 and 7 minutes for all measurements.

4.4. Data processing

Processing the data of the ERT and TEM measurements follow the same steps in general. It starts with exporting the data from the Terrameter LS or the WalkTEM. Necessary files are created that include the topography of the terrain if needed. The files are imported to a program used for processing the data of the ERT and TEM respectively. The inversion is then made within respective programs. Inversion is a mathematical and statistical process that uses measured geophysical data to acquire a fitting model that can be used for interpretation. The process is done in iterations, meaning it creates a model, repeats this process from the previous iteration until a final model is obtained. Each model is then given a data residual or percentage related to the reliability of each model, where a low number indicates good reliability.

4.4.1. ERT

The data from the Terrameter were exported to a computer. With the program Terrameter LS Toolbox *dat-files are created and stored on the computer. If measurements have been done in a terrain with varying topography, this was added within these files. The files are then opened in the program RES2DINV. Within this program there is an option called “exterminate bad datum points”. This option enables to view all the data points and to exclude those that are believed to be bad. Thereafter, the inversion can be made. For the inversion, the program Workbench was used, a GIS program. The files were opened in the program and the inversion was done with the laterally constrained inversion (LCI).

4.4.2. TEM

Two programs were used to process the TEM data, SPIA and Workbench. SPIA was used for inverting all data points. The data obtained from SPIA make interpretation difficult, since it can only create 1D models. Therefore, Workbench was used for generating 2D and 3D models, making it easier to visualize and interpret.

The data were imported to SPIA. In the interface of the program, the points are divided into stations. Before performing the inversions, it is necessary to analyse which points to use. Each station contains the HM, LM and noise, which were obtained from each measurement. Axes were set to stacked dB/dt against time. This makes it is easier to visualize when the noise starts interfering with the data (compared to when using stacked Rhoa (r) against time). All the points which interfered with the noise were excluded, but also the first 2 – 3 points from the LM, due to the long turn-off time for the HM, that can affect the reliability of early gates.

SPIA uses a 1D inversion algorithm when performing the inversions. It creates two types of inversions: smooth and layered (Fig. 20). The smooth inversion consists of 20 layers with predefined thicknesses, whereas the layered inversion consists of five layers whose thickness of the layers are not predefined. There are pros and cons with both models but due to the apparent heterogeneity of the geology the smooth model was preferred for this study, since this model is more likely to detect small variations within the ground. Each inverted model has a data residual. A desired data residual below 15 was aimed for this study, although data residuals above 15 were acceptable but had to be interpreted with caution. In order to obtain the

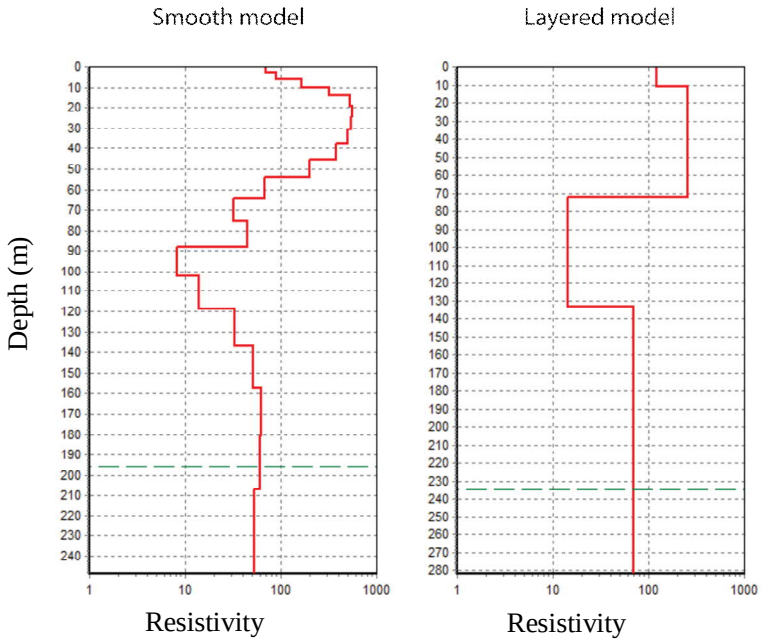

Figure 20. The two types of inversion models that can be created in SPIA are shown: the smooth inversion model (left) and layered inversion model (right). The smooth model assumed the ground is made up of 20 layers, creating a more detailed result. The layered model assumes the ground is made up of five layers, creating an overview of how the resistivity changes with depth.

best model, and hence the most reliable, points were excluded and included several times to receive as low data residual as possible. Appendix B summarizes the data residual of all measurement points/stations and ERT profiles.

Within SPIA, all smooth and layered models with the lowest data residual were saved for each station. The smooth and layered models were separately imported to Workbench. When opening the models in Workbench, the coordinates were automatically plotted on the program interface, since each station had coordinates attached to it in SPIA. In Workbench the following was created: mean resistivity at different depths within the ground from the smooth and layered models, 2D profiles at points of interest for the study containing the smooth model and a 3D model from the created 2D models.

For the mean resistivity at different depths, six layers of different depths were created for each station. The top layer is located at 2660 m.a.s.l. and the separation of each layer is 40 m. A 2D grid, with the mean resistivity of the smooth model, was applied to each of the eight layers at all stations. In the options the number of processors was 4, the search radius was set to 400 m, the node spacing was set to 10 and the interpolation method used was inverse distance with the power of 4. The same was done for the layered model. The 2D profiles were drawn manually at points of interest. The search distance was set to either 100 or 250 m depending on which search distance gave the most coherent looking profile. This means that, from where the profiles were drawn, Workbench searches for nearby measurements, at the given distance, to make the interpolation. Appendix C shows search distances for the different profiles. Only the smooth model was used for the TEM profiles. A 3D model was also created from the previously created 2D models.

4.5 Limitations of the methodology

Some limitations were detected when performing the geophysical method of Transient Electromagnetic Method (TEM) and Electrical Resistivity Tomography (ERT) during the fieldwork. TEM is sensitive to metallic objects, such as metal trash, and powerlines close to the measurements and can in their presence influence the results. Consequently, measurements were not performed in some areas. Other planned measurements could not be performed due to inaccessible property. However, the number of measurements proved to be sufficient for providing accurate and detailed results. ERT measurements provide optimal results on a horizontal topography. The variation of the topography in some areas can affect the signal strength at greater depths during measurements, resulting in lower penetration depth (pers. comm. Gonzales 2019).

5. Results

Three ERT lines and 33 TEM measurements were performed in the study area (Fig. 21). The red and light blue lines represent the locations and directions of the ERT and TEM lines and the white and blue dots all locations of the TEM measurements. During data processing three measurements/stations (points 6, 21 and 33, marked in blue on Fig. 21) had to be excluded because of inaccurate results. Points marked in black on Fig. 21 were foreseen for TEM measurements, but these locations were either inaccessible properties or in proximity to powerlines or metal objects that posed a high risk of galvanic coupling resulting, in poor data. To complement the ERT and TEM results, two UNDP (1979) lithology reports from nearby wells (Fig. 6) were used (see yellow points on Fig. 21). Appendix D shows a geological map containing all ERT an TEM measurements.

Before inverting the TEM data in SPIA, it was necessary to identify possible coupling effects at all stations. In the field notes (mentioned in section 5.3.2), 13 stations (App. B) are marked for being close to powerlines, metallic objects, trash and other noise sources. that possibly could suffer from coupling effects. However, none of them showed effects of galvanic or capacitive coupling and all stations (except station 32) had data residuals below 15 (see 5.4.2). Regarding the other 20 stations, a few data residuals were higher than 15 (App. B). The cause for their high data residual is not known. Nevertheless, they were kept during the data processing since they did neither show obvious signs of galvanic or capacitive coupling, nor were there any known disturbances nearby. However, the possibility of galvanic coupling cannot be ruled out due to difficulties identifying such effects.

A total of nine lines were drawn in Workbench from the TEM data. Three of these lines were drawn at the same locations and directions as the ERT lines in order to compare and assess the TEM and ERT results. These lines are named TEM lines 1, 2 and 6. Appendix E shows the locations and directions of all TEM lines made in Workbench.

For providing an overview, not all results are shown in section 6.1. The results not shown in this section are included in appendix F. A Workbench option allows to merge 1D models and to present them in a graph. Two graphs are presented in Fig. 22. One with selected locations from the farmland and the other graph with selected locations from the river. These graphs make it possible to determine a general resistivity trend within the farmland and the river. This is followed by TEM and ERT lines 1, 2 and 6. Then the smooth and layered models of mean resistivity at different depths are presented. Finally, one 3D model containing TEM lines 1, 2 and 6 illustrates how the resistivity varies with depth throughout the study area.

Results from three ERT lines and four TEM measurements in the mountain area are shown in section 6.2.

Reliable interpretations of ERT and TEM profiles can only be done down to a certain depth, as defined by the so-called depth of investigation (DOI). There are two types of DOIs: the conservative and the standard types. The TEM profiles only contain the

conservative DOI, while the ERT lines include both DOIs. The conservative DOI is always located below the standard DOI. Within the conservative DOI no interpretations should be made. Data within the standard DOI are considered reliable but interpretations have to be done with caution. Both DOIs are marked with shaded areas. Furthermore, descriptions and interpretations of the profiles are done by analysing the main features that the profiles are presenting. The ground consists of sediments where higher resistivities are associated with coarser grained materials (sand, gravel and blocks), whereas lower resistivities are linked to finer grained materials (mud). In this thesis, differences in resistivity are only interpreted based on lithological differences. It should be noted that the resolution of the profiles is not high enough to enable distinguishing individual thin layers. Therefore, a layer that is considered consisting of coarse-grained sediments (high resistivity) does not exclude the existence of fine sediments within the same layer.

Although the electrode contact with the ground was controlled twice before each ERT measurement, a bad contact of some electrodes with the ground was inevitable. This affected some results and can be seen as small areas of high resistivity at the top of the ERT profiles. However, this is not a relevant issue since the aim of this thesis is to investigate the deeper part of the ground.

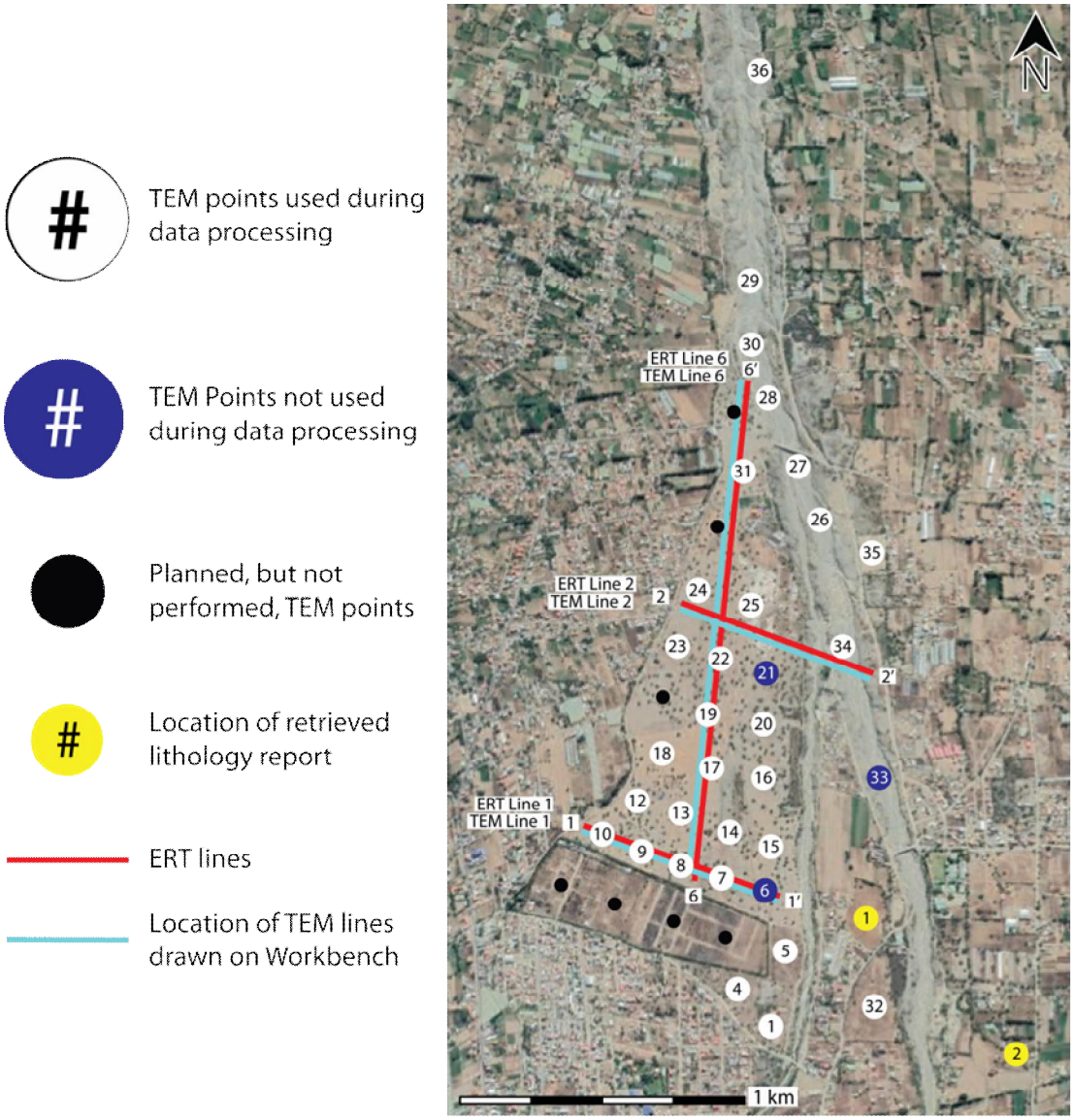

Figure 21. Study area showing locations of ERT lines (red) and TEM measurements (white & blue). The TEM lines drawn in Workbench are also marked (light blue). White dots are TEM points used during data processing, while the blue dots were disregarded. Black dots represent locations where measurements were supposed to be done but could not be due to either inaccessible property or proximity to powerlines or metal objects. Finally, yellow points are the locations of the retrieved lithology reports by UNDP (1979).

5.1. Results

5.1.1. General resistivity trend from the farmland and river

In general, all resistivity values range from 20 to 2000 Ωm. The lowest and highest resistivities measured are around 1 and 20000 Ωm respectively. Two 1D profiles from the farmland and the river provide how the resistivity varies throughout the study area (Fig. 22). All used and not used stations for the profiles are listed in appendix G. Within the farmland, the resistivity values from the TEM soundings do not follow a clear trend (Fig. 22a). The reason could be due to unknown proximity of metal trash during some measurements, giving rise to the variation in resistivity. Therefore, an interpreted interval of resistivity at all depths is marked as a shaded area in the profile below. Overall, the resistivity increases the first 25 m in the ground, then it decreases between 25 to 55 m. At 55 m and down 200 m, the resistivity remains relatively unchanged. The general trend from the river (Fig. 22b) is more distinct. The resistivity at the surface is 100 Ωm and increases down at 50 m, reaching its maximum resistivity value of around 2 000 Ωm. Then the resistivity decreases to values lower than 100 Ωm down to 115 m. Afterwards, the resistivity increases again, recording values close to 300 Ωm at 200 m.

Comparing the two resistivity trends, the measurements from the river show more consistent values than in the farmland. The major difference is in the top 100 m, where the high resistivity extends further down in the ground at the river and yields higher resistivity values.

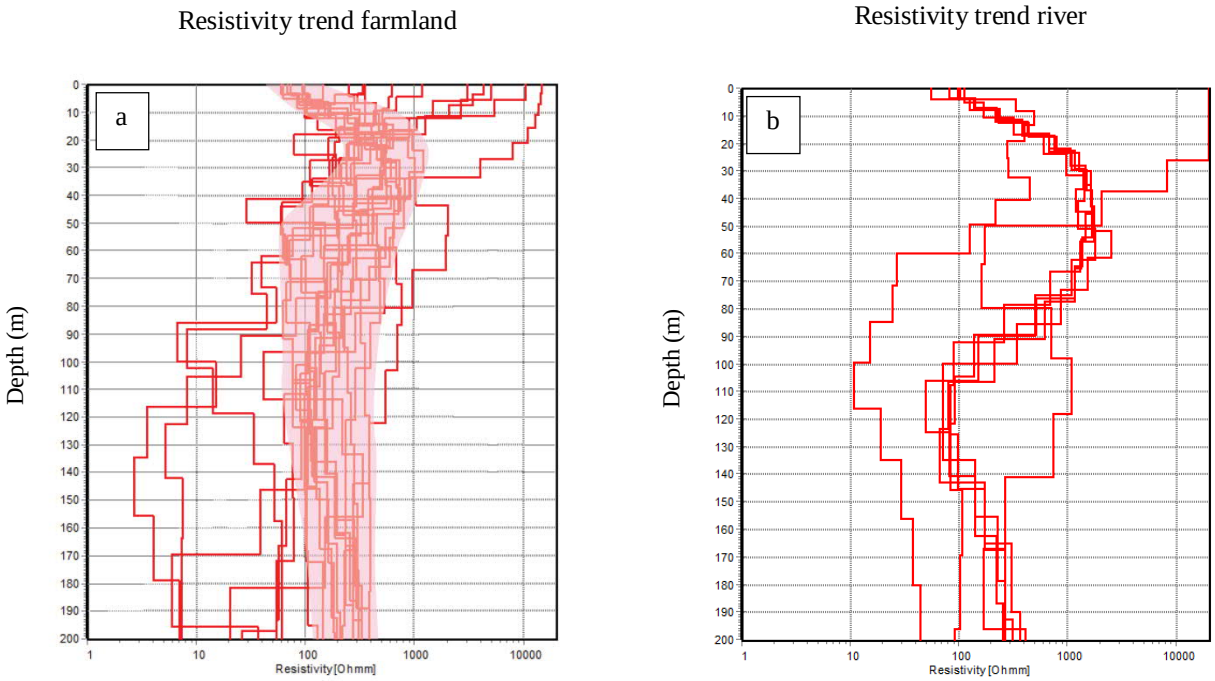

Figure 22. Resistivity trend from selected TEM measurements from the farmland (a) and the river (b). The general trend at both sites is that the resistivity increases at first, then decreases and finally remains the same or rises slightly until 200 m. The measurements from the river are more coherent compared to the farmland. Both graphs were made in Workbench.

5.1.2. TEM line 1 and ERT line 1

TEM line 1 has a maximum penetration depth of 230 m (Fig. 23). The profile is in the farmland. A high resistivity area with a thickness of 40 m (2620 – 2580 m.a.s.l.) is located in the eastern part (right side of the profile). Westwards (left side of the profile), the thickness of the layer decreases to only a few m. Beneath this layer, the resistivity remains more or less the same, at about 100 Ωm down to the DOI. It should be noted that the resistivity is slightly higher with around 300 Ωm at 210 – 280 m (x-axis).

ERT line 1 has a maximum penetration depth of 110 m (Fig. 24). The small areas of high resistivity in the surface of the profile is possibly due to bad electrode contact (see above in section 6). Down to 2590 m.a.s.l., the resistivity varies horizontally throughout the profile between 100 – 400 Ωm. The high resistivity in the top eastern part, as seen in TEM line 1 above (below 1'), cannot be seen in the ERT line 1 profile. Below 2590 m.a.s.l., the resistivities have values of around 100 Ωm. However, three vertical structures of approximately 600 Ωm between 200 – 250 m, 380 – 440 m and 580 – 640 m are extending downward to the DOI. Despite having a data residual of 8.27, the TEM profile probably indicates a more accurate description of the resistivity, because vertical structures with such distinctive differences in resistivity are not plausible in this geological area.

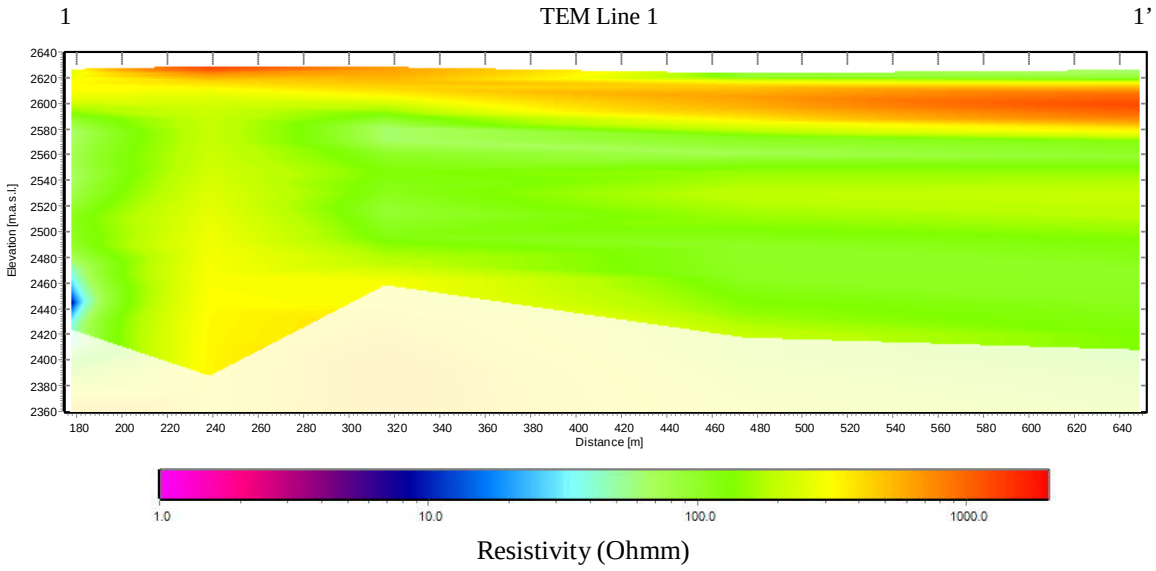

Figure 23. A 2D profile showing the variations in resistivity within TEM line 1.

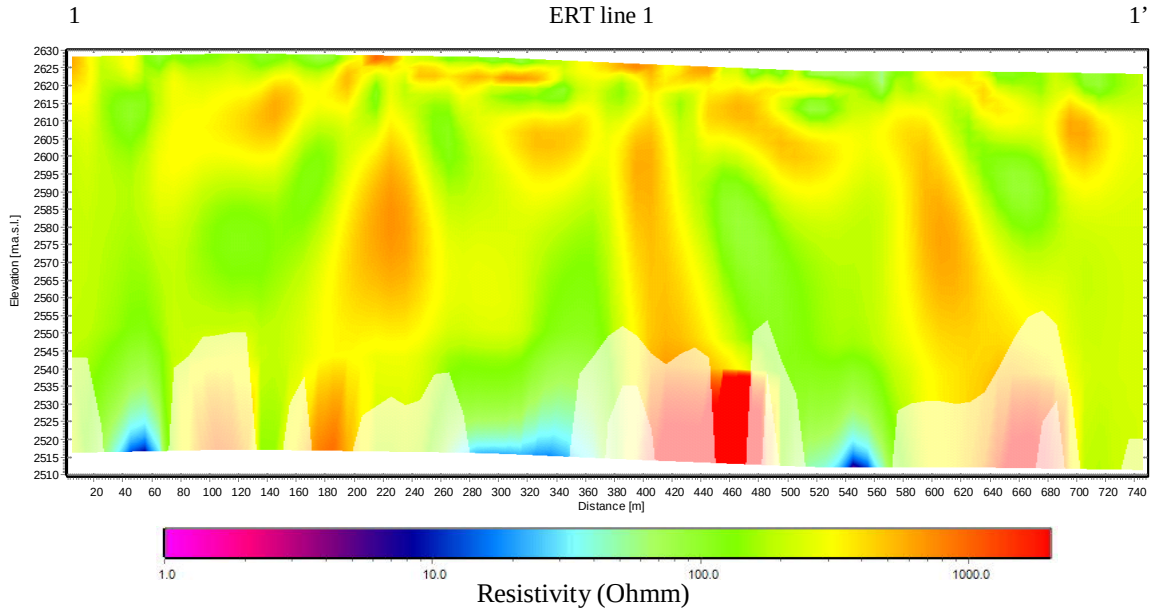

Figure 24. A 2D profile showing the variations in resistivity within ERT line 1.

5.1.3. TEM line 2 and ERT line 2

TEM line 2 has a maximum penetration depth of 180 m (Fig. 25). The profile spans across the farmland in the west and central part (180 – 460 m, x-axis) and the river in the eastern part (460 – 700 m, x-axis). The highest resistivities are located in the first 20 and 90 m in the west and east respectively. In this hig resistivity layer the resistivity reaches up to 2 000 Ωm. The data indicates a thin low resistivity layer (300 Ωm) at 2620 – 2600 m.a.s.l., but this can also be due to incorrect interpolation. Below this high resistivity layer, the resistivity is around 100 Ωm down to the DOI. In the western part at 2550 – 2510 m.a.s.l., a low resistivity area appears with a resistivity of approximately 10 Ωm.

ERT line 2 has a maximum penetration depth of around 100 m down to the standard DOI (Fig. 26). Bad electrode contact possible causes inconsistent resistivities at the top of the profile. The topography of the river can be seen in the eastern part. Below the farmland, a layer of low resistivity of (between 40 – 200 Ωm) is located at 2635 – 2620 m.a.s.l. and below the resistivity increases to 2000 Ωm. Below the river, there is a 25 m thick layer of high resistivity up to 2000 Ωm. Further down, the resistivity decreases and at around 40 m a rounded structure with low resistivity (5 – 20 Ωm) reaches into the standard DOI. Therefore, the existence of this structure is not certain.

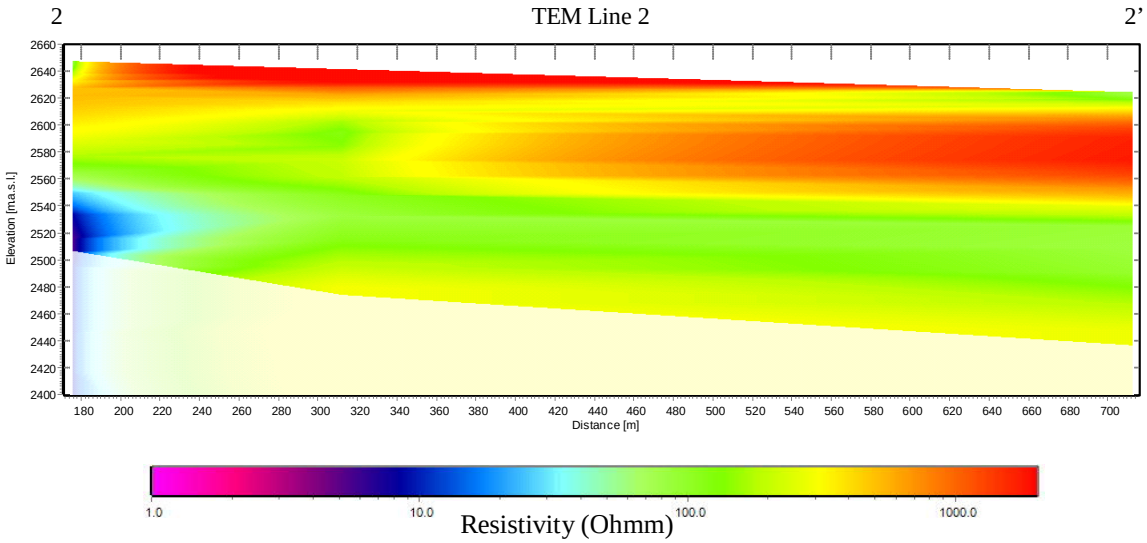

Figure 25. A 2D profile showing the variations in resistivity within TEM line 2.

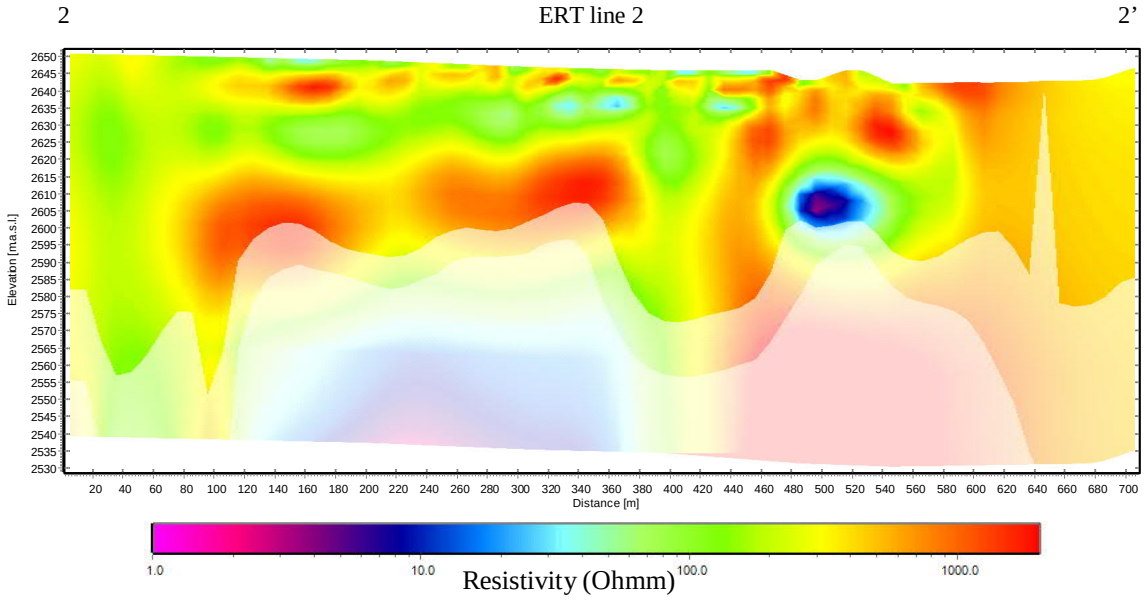

Figure 26. A 2D profile showing the variations in resistivity within ERT line 2.

5.1.4. TEM line 6 and ERT line 6

TEM line 6 has a maximum penetration depth of 260 m (Fig. 27). The line extends almost 2000 m from the northern to the southern part of the farmland. Resistivities reaching 2000 Ωm dominate the shallow parts of the profile. The thickness of this layer varies in the range of 30 – 80 m. Below this layer, resistivity values drop to around 100 Ωm down to the DOI. In the southern part (1600 – 1900 m, x-axis), the resistivity is slightly higher, reaching values of approximately 300 Ωm down to at least 2400 m.a.s.l.. In the northern part, a vertical structure of low resistivity (10 – 50 Ωm) can be observed. It extends from 2600 to 2460 m.a.s.l. and is approximately 100 m wide.

ERT line 6 has a maximum penetration depth of 110 m (Fig. 28). The inconsistent resistivity values at the top are possibly due to bad electrode contact. The profile indicates that the subsurface does not have any horizontal structures. Instead, vertical and elongated oval structures of higher resistivities (up to 2000 Ωm) are the main feature. The surrounding ground has resistivities ranging from 60 to 400 Ωm.

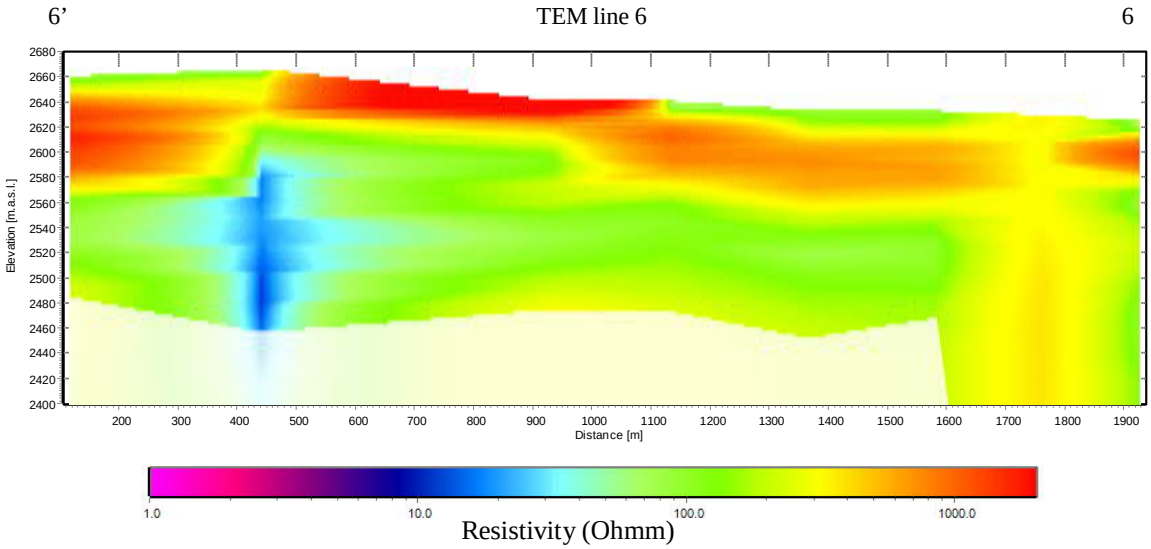

Figure 27. A 2D profile showing the variations in resistivity within TEM line 6.

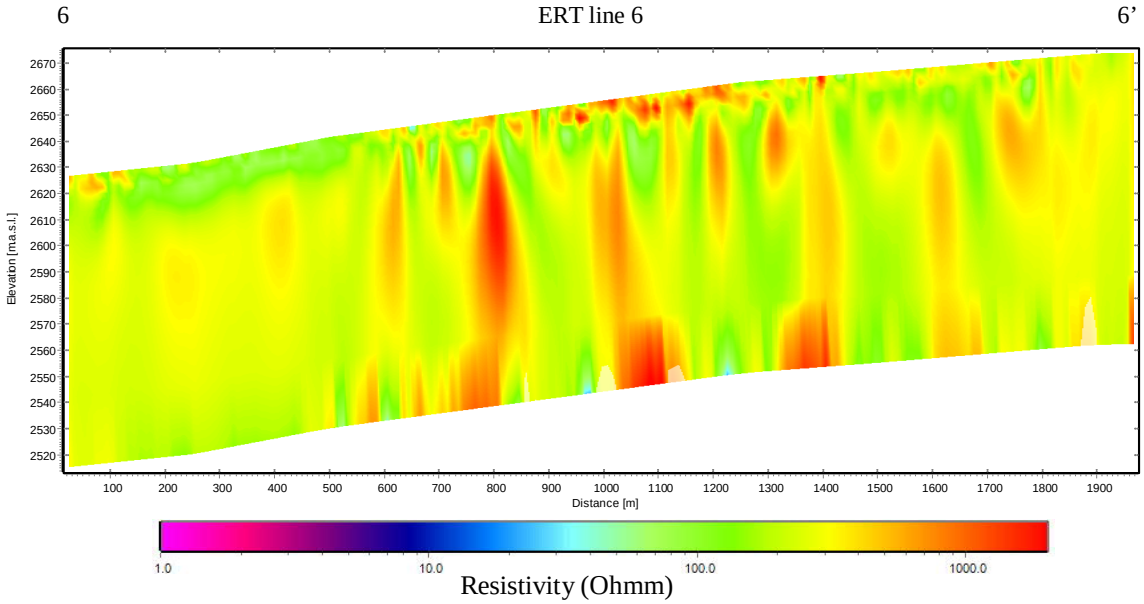

Figure 28. A 2D profile showing the variations in resistivity within ERT line 6.

5.1.5. Mean resistivities at different depths

The mean resistivities at different depths are shown in Fig. 29. The smooth (left) and the layered model (right) have six layers with a separation of 40 m between each layer. It should be noted that the northernmost measurement (left on both model images) will not be taken into account within this description because its location is too far away from the other measurements. In the smooth model, the top two layers (2660 – 2580 m.a.s.l) record the highest resistivity values. The only exceptions are the middle eastern part of the top layer and the south-western part of the second layer where the resistivities are around 100 Ωm. In general, the resistivity drops to approximately 100 Ωm at 2580 – 2540 m.a.s.l.. In the mid-eastern part, the resistivity remains high, while a low resistivity area (10 – 20 Ωm) appears in a small area of the mid-western part. In the layers at 2540 – 2500 and 2500 – 2460 m.a.s.l., the high resistivity areas ceases to exist, and the area of low resistivity in the mid-western part increases in size. In the south, resistivities drop to 5 – 40 Ωm. In the bottom layer (2460 – 2420 m.a.s.l.), the resistivity increases slightly in the central areas. However, it should be noted that the bottom layer lies close to or in the DOI and interpretations should be avoided.

The layered model shows a resistivity pattern similar to the smooth model. The first two layers have slightly higher resistivities in some areas compared to the smooth model. The third layer (2580 – 2540 m.a.s.l.) shows a small circular area in the mid-southern part with a resistivity close to 1 Ωm and continues down to the bottom layer. This low resistivity area does not appear to be natural and is probably due to poor data. The bottom three layers have similar resistivities as the smooth model, except in the northern part where the resistivity increases from approximately 100 Ωm in the higher end of the resistivity spectrum. In addition, the bottom layer shows higher resistivity in the mid-western part than in the smooth model.

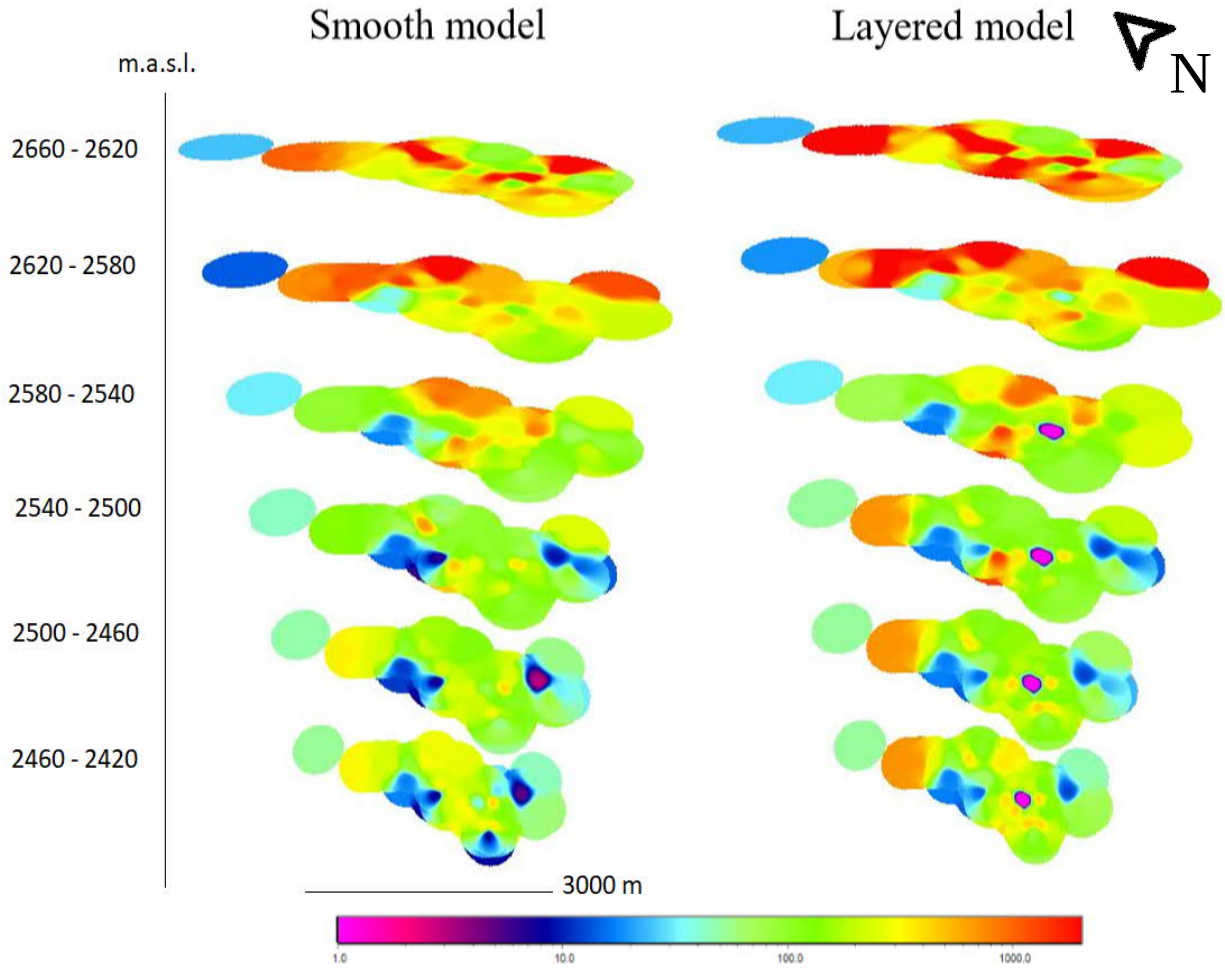

Figure 29. Mean resistivity at different elevations from the smooth and layered model. Each layer is 40 m apart.

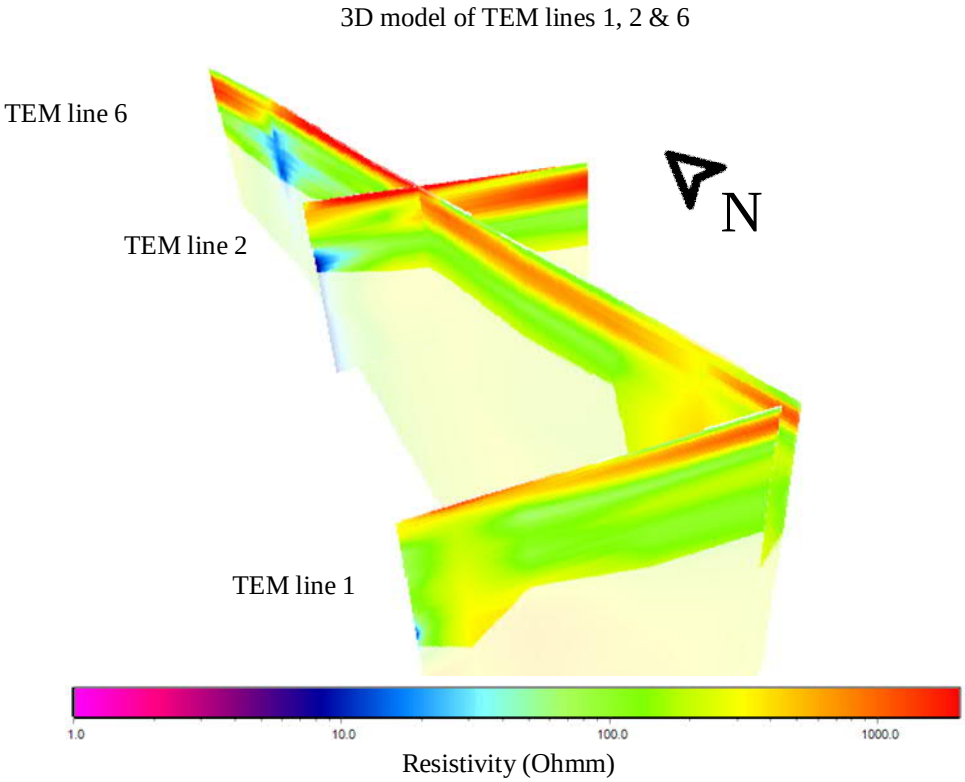

Figure 30. 3D model containing TEM line 1, 2 and 6. The model shows the variations of resistivity from the study area.

5.1.6. 3D model TEM lines 1, 2 and 6

The 3D model containing TEM lines 1, 2 and 6 are shown in Fig. 30. Generally, the top layer shows resistivity values up to 2000 Ωm. The thickness of this layer varies throughout the study area. In the northern and eastern parts, the layer is more noticeable and thicker than in the southern and western parts. A maximum thickness of 90 m in the eastern part (TEM line 2) and in the northern part (TEM line 6) is observed. The thickness decreases to 30 m in the south and to a few m in the south-west. Deeper down and to the DOI, resistivities generally drop to approximately 100 Ωm throughout the area. Two areas in the southern and south-western parts show slightly higher resistivities. The low resistivity area (10 – 40 Ωm) is located in the northern and north-western parts of the 3D model (Fig. 29).

5.2. Results from the additional investigations in the mountain area

In total three ERT and four TEM measurement were performed: two TEM measurements in the forest (points 37 & 38); one ERT line and two TEM measurements in the area of the soccer field (line 3 and points 39 & 40). Finally, two ERT lines were performed at the thermal bath of Liriuni (lines 4 & 5). Locations of these ERT lines and TEM points are shown in Fig. 31. The data residuals for all measurements are presented in appendix B.

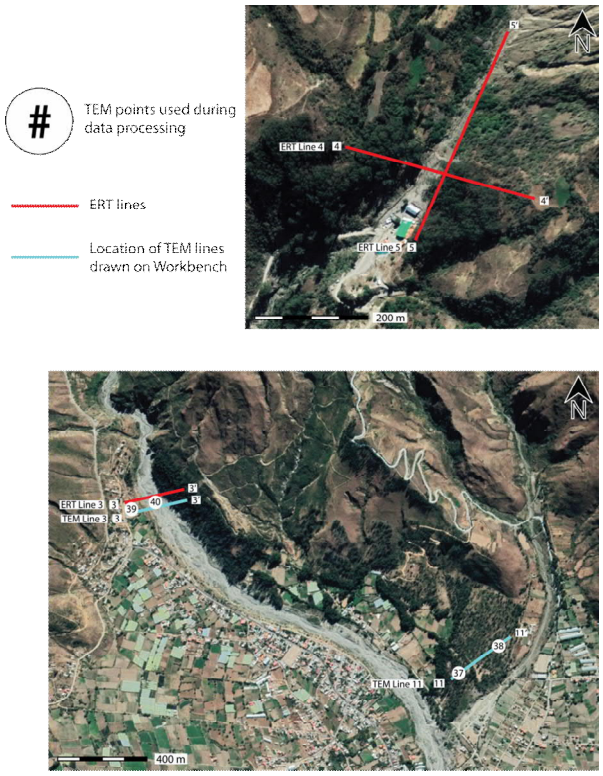

Figure 31. Locations of ERT lines (red) and TEM measurements (white) from the extra research in the mountain area. TEM lines drawn on Workbench are also marked (light blue). The forest area (bottom picture) is where TEM points 37 and 38 are located. The soccer field (bottom area) is where TEM points 39 and 40 are located. Liriuni (top picture) is located north of the forest and the soccer field).

5.2.1. Forest

TEM line 11 has a maximum penetration depth of 240 m (Fig. 32). The results indicate a higher resistivity in the top 60 m (400 – 2000 Ωm), especially in the western part of the profile. The resistivity decreases further down to around 100 Ωm towards the DOI, except in the western part, where the resistivity values reach a minimum of 20 Ωm at a depth of around 200 m.

5.2.2. Soccer field

TEM line 3 has a maximum penetration depth of 300 m (Fig. 33). This profile contains four distinctive layers of different resistivities. The top layer at about 80 – 100 m shows resistivity values of around 20000 Ωm. Below, a layer of about 30 m appears at 2780 – 2750 m.a.s.l. with resistivity values reaching 10 Ωm. A resistivity of around 100 Ωm follows in the next 100 m. Finally, a low resistivity layer is located in the western part of the section reaching resistivity values down to around 1 Ωm. This profile contains the highest (20000 Ωm) and lowest (1 Ωm) resistivity values recorded overall. The data residuals of measurements 39 and 40 are high, 17.3 and 16 respectively. It should be mentioned that the soccer field was surrounded by metallic fences, probably causing these high data residuals.

ERT line 3 has a maximum penetration depth of 110 m (Fig. 34). There is a total elevation difference of about 50 m in the profile. Bad electrode contact might cause the inconsistent resistivities in the upper 30 m of the profile. The resistivity pattern has no resemblance to TEM line 3, but is more realistic that TEM line 3. Below, the resistivity reaches values of about 300 Ωm in the western part, while values of around 1000 Ωm appear in the eastern part. The resistivity drops to around 100 Ωm in the middle section, down to 2770 m.a.s.l.. It should be noted that the standard DOI is close to the surface in most parts of the profile.

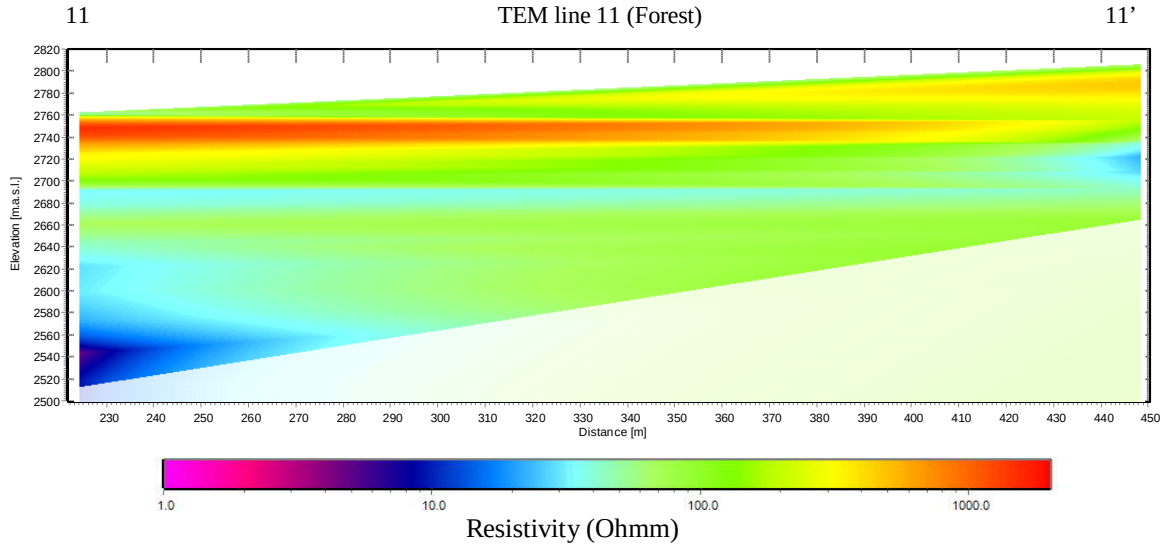

Figure 32. A 2D profile showing the variations in resistivity within TEM line 11.

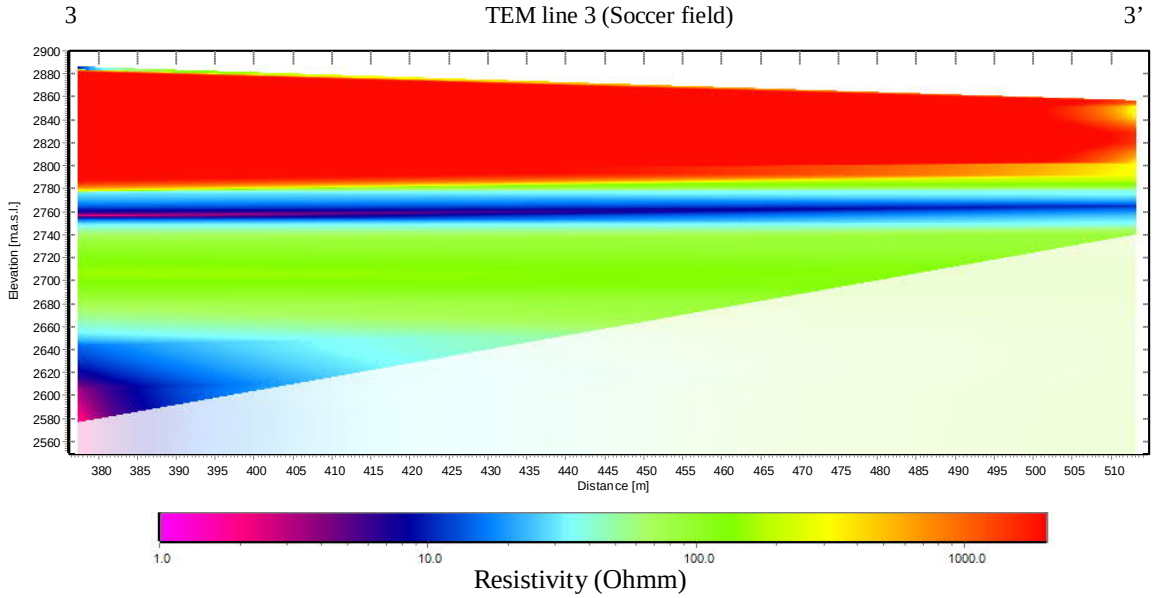

Figure 33. A 2D profile showing the variations in resistivity within TEM line 3.

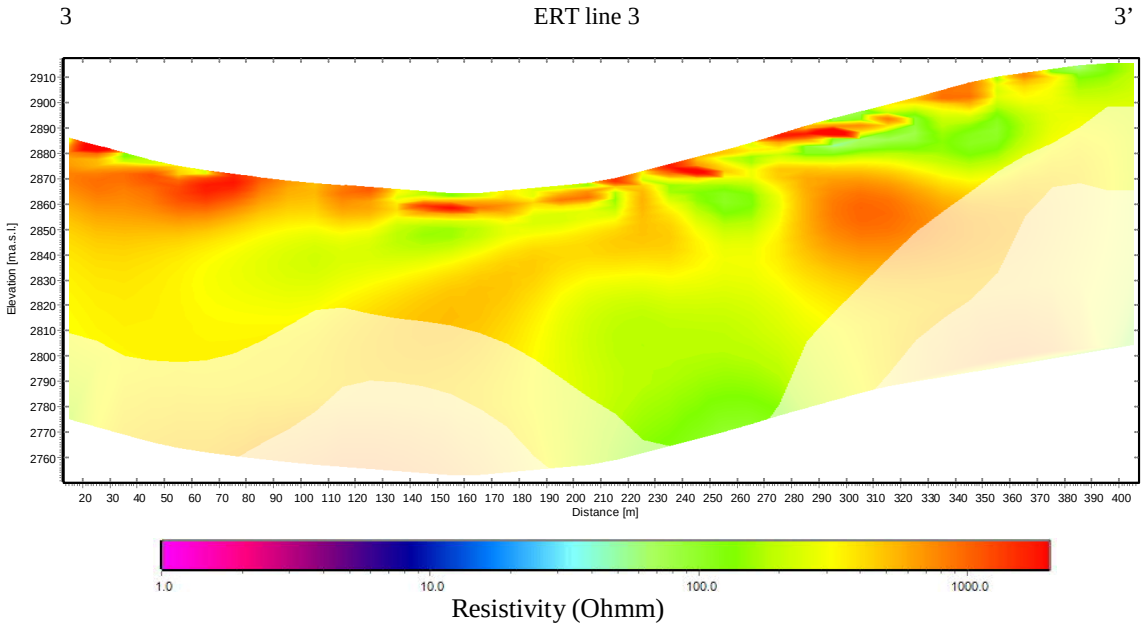

Figure 34. A 2D profile showing the variations in resistivity within ERT line 3.

5.2.3 Liriuni

ERT line 4 has a maximum penetration depth of 60 m (Fig. 35). The elevation difference in this profile is around 65 m. High resistivities at the top might be due to bad electrode contact. Overall, the profile shows resistivities of approximately 100 Ωm. The main feature is in the central portion, where resistivities are low in two spots (10 – 40 Ωm). The standard DOI is close to the surface, especially in the eastern part, making further interpretations difficult.

ERT line 5 has a maximum penetration depth of 120 m (Fig. 36). As in the previous profile, the varying resistivity at the surface is possibly due to bad electrode contact. The profile mainly consists of resistivities of about 100 Ωm. In the southern part, low resistivities are recorded (30 – 40 Ωm). Two spots in the central part of the section have low resistivity (30 – 40 Ωm), similar to ERT line 4.

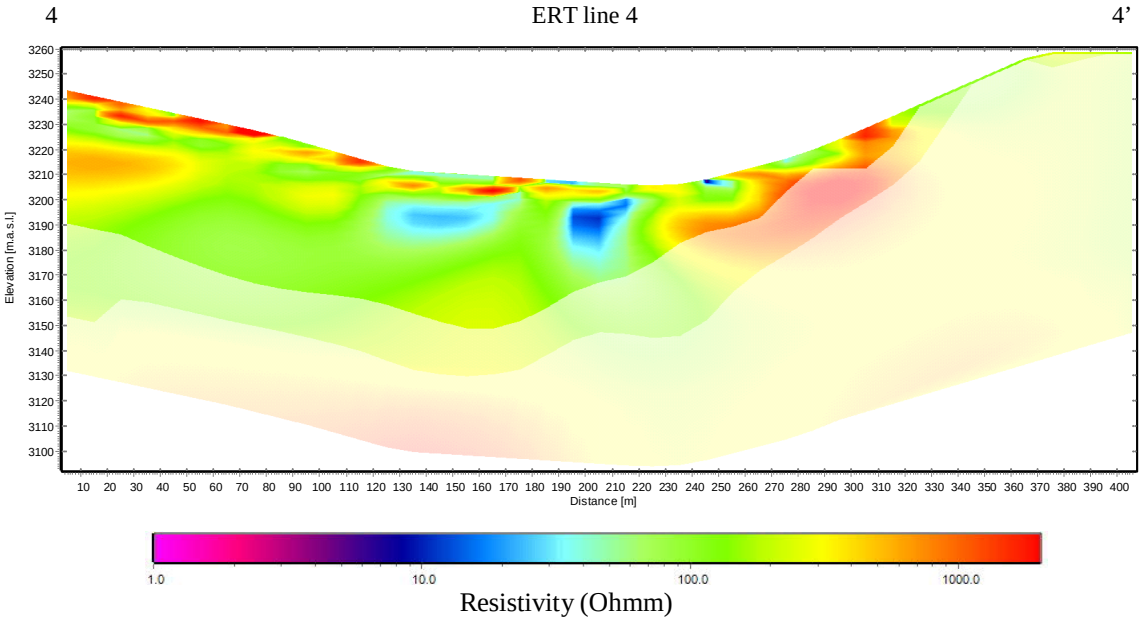

Figure 35. A 2D profile showing the variations in resistivity within ERT line 4.

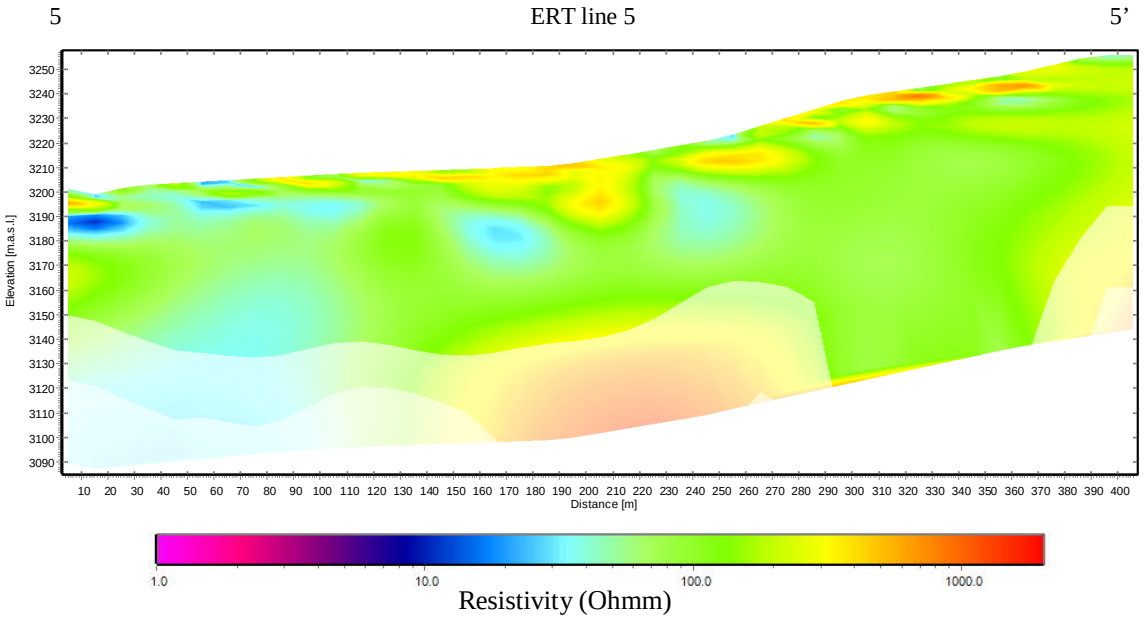

Figure 36. A 2D profile showing the variations in resistivity within ERT line 5.

6. Discussion

6.1. Geometry of the potential aquifer and the depth and resistivity of the bedrock

The results of the geophysical measurements provide insight as regards to the geometry of the aquifer. The measurements show resistivities up to 2000 Ωm in the upper parts of the subsurface. According to the resistivity chart (Fig. 9) by Palacky (1987), coarse-grained sediments, like gravel and sand, have resistivities ranging from 500 to 10000 Ωm. The lithology reports, mentioned in section 4.2.4, show that coarse grain sizes dominate the lithology in the top 70 – 100 m. Moreover, the geological map (App. A and D) shows surface sediments in the study area consist of alluvial fan deposits (boulder, gravel, sand and silt). Thus, it can be concluded that the top layer of high resistivity mainly contains sand, gravel and blocks in different proportions. This creates favourable conditions for water to infiltrate and to be stored. The high resistivity layer in the upper parts of the ground therefore represents the potential aquifer. Fig. 37 shows a 3D model containing TEM lines 1, 2, 6, 7, 8, 9 and 10. This model, combined with the resistivity trends from the farmland and the river (Fig. 22), gives a clear overview of the geometry of the potential aquifer. The models show that the potential aquifer is thicker in the northern and eastern part than in the southern and south-western part of the study area. This is in accordance with the decrease in grain size towards the centre of the valley (see section 4.2.1). The maximum thickness of the potential aquifer is 110 m and is located in the north-eastern part (where TEM lines 8 and 10 cross, App. E). The thickness in the north and east is about 90 m. In the central-eastern part of the study area it is around 80 m thick, while its thickness is 20 m in the mid-western part. The thickness is 40 m in the southern part. Finally, the minimum thickness of the potential aquifer is 5 m in the south-western part.

With regards to the boundaries of the potential aquifer, a boundary could be set in the south-western part, since a 5 m thick potential aquifer would not be economical to extract water from. However, it would still serve as an important area for infiltration of water to feed the potential aquifer. In the southern, western, northern and eastern parts of the study area, the thickness of the potential aquifer is significant, and no boundaries could be set. Further investigations would be needed in order to set the boundaries of the aquifer in the south, west, north and east. In addition, it is likely that this study area is representative for the rest of the northern part of the valley because the geology does not change significantly (App. A & D).

Further down, the resistivity decreases to approximately 100 Ωm. This resistivity is in line with resistivities of clay (3 – 100 Ωm) according to Fig. 9. Although 100 Ωm is in the higher end of the resistivity spectrum for clay, some sand, gravel and blocks within the layer are probably increasing the overall resistivity. The existence of fine-grained sediments below the coarser grains would also be in line with the geological history. Deposition of fluviolacustrine sediments during the upper Tertiary were followed by the accumulation of coarser sediments transported from the mountainous area during the Quaternary.

As mentioned in section 4.2.4, the thickness of the sediments in the valley increases from 100 m in the south to up to 1000 m towards the north (Renner & Velasco 2000). The maximum penetration depth of the measurements is 260 m (TEM line 6) and since the study area is located in the northern part of the valley, the thickness of the sediments is expected to exceed 260 m. Therefore, the depth of the bedrock cannot be determined in the study area. Instead, additional investigations in the forest and the soccer field could provide information about the resistivity of the bedrock. The bedrock within the study area consists of Ordovician siltstone (App. A). Although the resistivity of siltstone is not shown in Fig. 9, it can be assumed that

it will be in the range of shales and sandstones (5 – 1000 Ωm). TEM measurements from the forest (Fig. 32) show a drop in resistivity to 20 Ωm at 160 m at the bottom part of the profile. In the soccer field, TEM line 3 (Fig. 33) with its abrupt changes in resistivity between the layers, and in combination with their high data residuals (App. B), make the measurements unreliable. However, ERT line 3 (Fig. 34) shows a more plausible result. The proximity of the standard DOI to the surface throughout the profile is probably due to topographical changes of the profile. Although no clear boundary can be seen in the profile, the central bottom part shows resistivities of around 100 Ωm at a depth of approximately 70 m. The low resistivity at the bottom of the profiles (TEM line 11 & ERT line 3) could mark the boundary between the Ordovician siltstone and the overlying sediments. Previous geophysical surveys from Renner& Velasco (2000) found that the resistivity of the bedrock range from 150 to 210 Ωm. Given the discrepancy of the resistivities, it is not certain if the drop in resistivity in TEM line 11 and ERT line 3 indeed represents the basement at the depth of 70 m and 160 m respectively. Further TEM and ERT measurements would be needed to confirm this.

The potential aquifer is a major recourse for the inhabitants of the Valley of Cochabamba. It can be served as a source for drinking water now and in the future. Therefore, it is important that the farmland (and the surrounding area) remains as open land, enabling the water to infiltrate. Construction of houses and other buildings on the farmland would thus hinder such processes. Furthermore, some measurements had to be discarded due to high abundance of metal trash or objects (see section 5.3.2). These would have to be removed from the farmland since they potentially could be a source of harmful elements to the groundwater.

6.2. Notes for further research

ERT and TEM measurements were used for determining the geometry of the potential aquifer. These two methods are supposed to complement each other. However, the TEM data have provided more plausible results and a greater penetration depth.

The TEM seems better suited for the measurements of the local sediments. The coarse material, especially from the river, made it sometimes difficult for the electrodes to make good contact with the ground, which probably affected the ERT measurements, which show strange structures in the profiles. For example, the existence of a coarse-grained layer (high resistivity) oriented in a vertical direction is not probable, as indicated in ERT lines 1 and 6. The rounded structure of low resistivity in ERT line 2 does not fit in the geological setting and its position at the standard DOI could be affected by faulty data, while the complementing TEM profile does not display that structure. Due to these inconsistencies in ERT lines 1, 2 and 6 and the relatively high data residual in ERT line 6 (14.26), interpretations are primarily based on the TEM results.

Despite the differences between the ERT and TEM profiles, ERT line 2 and TEM line 2 indicate a low resistivity layer in the shallow parts of the profile. This is more noticeable in the ERT line 2 profile. As the TEM line 2 profile is an interpolation between several points, it is difficult to assess the existence of a thin layer of low resistivity, i.e. a layer of fine-grained sediments. If this impermeable layer would exist, the infiltration of water into deeper parts would be blocked.

The 1D models of TEM measurements in Workbench of the points 24 and 31(Fig. 21) show a drop in resistivity from around 100 Ωm down to 6 – 20 Ωm at 90 m. This is seen in Fig. 37, Fig. 29 and App. F (TEM line 9). This indicates that the lithology below 90 m includes more finer grains. It should be noted that the planned measurement between these points (Fig. 21) was not performed due to the proximity to metal objects. This missing measurement would have provided more detailed data for assessing the presence of this layer of more fine-grained sediments.

The depth of the water table is assumed to be around 40 m in the study area (pers. comm. Gonzales 2019). As the resistivity of a fluid depends on its salinity and ion content, the resistivity will be lowered if the concentration of ions is high within the fluid (Jeppsson & Dahlin 2017). At the moment, no data regarding the water chemistry is available. According to Gonzales (2019), the groundwater in this area has relatively low concentrations of ions, since it is used for drinking water without any treatment (pers. comm. Gonzales 2019). The measurements show no signs of changing resistivity at 40 m depth where the water table is assumed to be located. Since the resistivity of the fluid is not known, an explanation could be that the resistivity contrast is not large enough to appear in the results. Additional investigations are needed to clarify this issue.

The depth to the bedrock in the Valley of Cochabamba is not fully known. Renner& Velasco (2000) provide some information about the depth to the bedrock, but mainly in the southern part of the valley. The increasing thickness of the sediments towards the north make it difficult to determine the depth, which also is the case for this thesis. However, if attempts are made in the future, resistivities in the range of 20 to 210 Ωm would likely indicate the bedrock.

6.3. Liriuni

Despite the distance from active volcanoes and low geological activity, the baths of Liriuni are geothermally heated. This phenomenon is not unique to this area and it occurs in other places on earth which are not geologically active, such as the thermal springs of Bath, UK (Gallois 2007), and several thermal springs in Hungary (Korim 1972). The hot springs in Bath are of meteoric origin (Gallois 2007). Due to the low geothermal gradient in the area, water infiltrates down to 2500 m and is heating up. Then the water rises adiabatically through fractures in the rocks. A similar process is likely to occur at Liriuni. It is not known where the meteoric water infiltrates. A hypothesis is that water infiltrates in faults and cracks in the mountainous area. However, the required depth of water infiltration and the geothermal gradient in the area is not known. A fault is located close to the thermal spring of Liriuni (App. A and D), where heated water could rise adiabatically and feed the thermal springs of Liriuni.

The dominating resistivity range throughout ERT line 4 and 5 (Fig. 35 & 36) is around 100 Ωm. As

Liriuni is situated in the mountains it can be assumed that the resistivity values reflect the bedrock (Ordovician siltstone) and not finer sediments, such as clay. A clear fault line cannot be seen from the ERT lines. However, the spots of low resistivity (10 – 40 Ωm) can be interpreted as more weathered parts of the bedrock. Weathering lowers the resistivity of rocks and therefore these areas probably contain faults or cracks, enabling the water to rise to the surface. The low depth of the profile is probably a consequence of

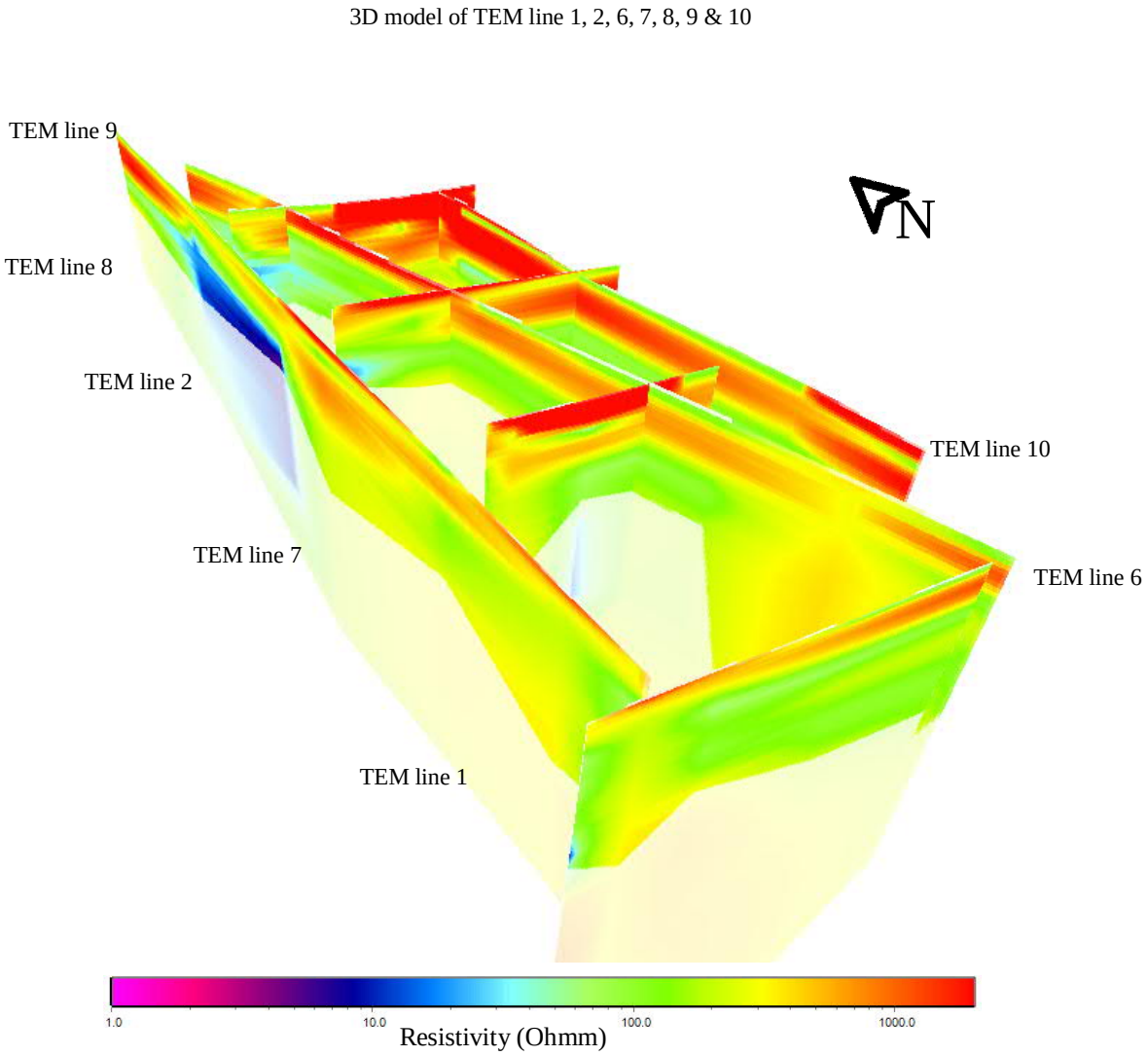

Figure 37. Same 3D model as in Fig. 30, but with the addition of TEM line 7, 8, 9 and 10. The model shows the variations in resistivity within the study area in greater detail.

the topographic differences within the profile.

7. Conclusions

- This thesis has primarily aimed at determining the geometry of the potential aquifer in the study area. This aim could be achieved. Its maximum thickness of about 100 m is located in the north-eastern part of the study area. In the northern and eastern part of the study area, the thickness is around 90 m. Towards the southern part, the thickness decreases to approximately 40 m, whereas it is about 20 m thick in the western part of the study area. In the south-western part the thickness of the potential aquifer drops to about 5 m. The south-western part could therefore be regarded as the boundary of the potential aquifer, while no boundary can be set in any other direction.
- This thesis secondarily aimed at determining the depth of the bedrock. Due to inadequate penetration depth of the measurements this could not be done. The thickness of the sediments is likely to be close to 1000 m thick in the study area, while the maximum penetration depth of the measurements is 260 m. The bedrock consists of Ordovician siltstone, which assumedly has a resistivity range of 5 – 1000 Ωm. Additional measurements that were performed outside of the study area, show resistivities between 20 and 100 Ωm at about 70 and 160 m depth, potentially indicating the boundary between the bedrock and the overlying sediments. Previous geophysical studies have shown that the resistivity of the bedrock is 150 – 210 Ωm, slightly higher than the observed resistivities in this thesis. Further TEM and ERT measurements are therefore needed to confirm the depth and resistivity of the bedrock.
- The surficial coarse-grained sediments allow water to infiltrate easily. This potential aquifer is therefore a necessity for the local inhabitants of the Valley of Cochabamba regarding drinking water. Any constructions on the open farmland will negatively affect infiltration of water and lower the recharge of this potential aquifer. Consequently, this potential source of drinking water would be lost. Furthermore, metallic objects and trash are present in some areas. These would need to be taken away, since they potentially could act as a source of harmful elements in the groundwater and thus drinking water.
- For future research. 1) it is suggested to use TEM prior to ERT if possible, because TEM has provided better penetration depth that ERT. The ERT measurements have generally not been reliable due to the fact that the coarse sediments make it difficult for the electrode to establish a good contact. The topography of the area probably affected the measurements as well. 2) Although the evidence is not conclusive, the bedrock most likely has a resistivity in the range of 20 to 210 Ωm. When attempting to determine the depth of the bedrock, this resistivity range could be used as a reference.
- Fine-grained sediments dominate the sediments below the potential aquifer, lowering the infiltration of water to greater depth. The measurements at ERT and TEM line 2 indicate a 15 – 20 m thick layer of fine-grained sediments close to the surface on top of coarse-grained sediments. This could potentially represent an aquiclude that locally blocks infiltrating water. Further ERT measurements with smaller electrode distances would be needed to confirm this assumption.
- In addition, measurements were performed to explain the existence of the nearby thermal baths of Liriuni. Two spots of lower resistivity in the profiles indicate that weathered rock allows heated water from deep parts to rise through cracks or faults.

8. Acknowledgements

I want to thank my external supervisor Andres Gonzales, professor at the UMSS, for his support during the fieldwork in Cochabamba and during this thesis.

I am grateful to my internal supervisor Dan Hammarlund, professor at Quaternary sciences a Lund University, for his valuable feedback regarding the structure of the thesis.

Special thanks to Toke Søltoft, Director & Geophysicist at Aarhus Geosoftware, and Etzar Gomez, doctoral student at Lund University, for the help to use Workbench in an efficient way.

Moreover, I want to thank Alfredo Mendoza, Senior lecturer at Engineering Geology, and Torleif Dahlin, Professor at Engineering Geology, for their feedback and inspiration during the thesis.

Finally, the fieldwork could not have been done without the WalkTEM that Teknisk Geologi at Lunds Tekniska Högskola (LTH) borrowed, Geoscientists Without Borders (GWB) who covered the transportation costs of the equipment from Lund to Cochabamba and the bachelor students Daniel Gareca, Daglin Camacho, Ivan Balcas and Jimmy Inca who helped during the fieldwork.

9. References

ABEM, 2019: WalkTEM Product Presentation. Retrieved: 2019-10-15.

Argollo, J. & Iriondo, M., 2008: *Cuaternario De Boli via y Regiones Vecinas*.

Christiansen, A., Auken, E. & Soerensen, K. 2009: The Transient Electromagnetic Method. *I*, 179-225,

Dahlin, T., 2001: The development of DV resistivity imaging techniques. Computers & Geosciences. 1019-1029 s.

Danielsen, J. E., Auken, E., Jørgensen, F., Sønder gaard, V. & Sørensen, K. I., 2003: The applica tion of the transient electromagnetic method in hydrogeophysical surveys: *Journal of Applied Geophysics 53***,** 181-198. doi: 10.1016/j.jappgeo.2003.08.004

Gallois, R. W., 2007: The-formation of the hot springs at Bath Spa, UK. Geological Magazine. 741-

747 s.
GEOBOL, 1979: Servicio Geologico de Bolivia - GE OBOL - Regional Cochabamba. 352 s.
GEOBOL, 1994: Carta Geologica de Bolovia Hoja Cochabamba.
Gouzes, R. & Delpont, G., 1990: Evaluacion de los recursos de agua y abastecimiento en aguq por table de la ciudad de Cochabamba Bolivia. BRGM-SEURECA.
Gregory-Wodzicki, K. M., 2000: Uplift history of the Central and Northern Andes- A review: *GSA Bulletin***,** 1091-1105.
Horton, B. K., 2018: Tectonic Regimes of the Central and Southern Andes-Responses to Variations in Plate Coupling During Subduction: *AGU Publi cations***,** 28. doi: 10.1002/
INE, 2016: Población de Cochabamba llega a 1.916.000 habitantes al 2016. Hämtad 2019-08-21 2019, från https://www.ine.gob.bo/index.php/component/k2/item/416-poblacion-de-cochabamba-llega-a-1-916-000-habitantes-al-2016?highlight=WyJjb2NoYWJhbWJhIl0=.
Korim, K., 1972: Geological Aspects of Thermal Wa ter Occurrences in Hungary. Geothermics. 96-102 s.
Lavenu, A., 1992: Formation and geological evolution. 16 s.
Lavenu, A., Thiele, R., Machette, M. N., Dart, R. L., Bradley, L.-A. & Haller, K. M., 2000: Maps and Database of Quaternary Faults in Bolivia and Chile. 50 s.
Mcneill, J. D., 1980: Technical Note TN-7. *Applica tions of Transient Electromagnetic Techniques.* Geonics Limited. 15 s.
Murray, B. P., Horton, B. K., Matos, R. & Heizler, M. T., 2010: Oligocene-Miocene basin evolution in the northern Altiplano, Bolivia: Implications for evolution of the central Andean backthrust belt and high plateau. 20 s.
Neumann-Redelin, C., Renner, S. & Torrez, J., 1978: UNDP-GEOBOL, 1978- Proyecto integrado de recur sos hidricos- Investigaciones de agues sub terráneas en las cuencas de Cochabamba. Co chabamba, Bolivia. 316 pp.
Palacky, G. J., 1987: Resistivity Characteristics of Geologic Targets. *Electromagnetic Methods in Applied Geophysics - Theory*. Society of Explo ration Geophysicist. 53-130 s.
Ramos, V. A., 2008: The Basement of the Central An des: The Arequipa and Related Terranes: *Annu al Review of Earth and Planetary Sciences 36***,** 289-324. doi: 10.1146/annurev.earth.36.031207.124304
Ramos, V. A., 2018: Tectonic Evolution of the Central Andes- From Terrane Accretion to Crustal De lamination.
Rapalini, A. E., Geuna, S. E., Franceschinis, P. R. & Spagnuolo, C. M., 2018: The Paleozoic Evolu tion of the Chilean-Argentinean Margin. *The Evolution of the Chilean-Argentinean Andes.* Spring International Publishing AG. 569 s.
Renner, S. & Velasco, C., 2000: Geología e Hidrogeo logía del Valle Central de Cochabamba. 125 s.
Reynolds, J. M., 2011: *An Introduction to Applied and Environmental Geophysics*. John Wiley & Sons, Ltd**.**
Rojas Vera, E. A., Giampaoli, P., Gobbo, E., Rocha, E., Olivieri, G. & Figueroa, D. 2019: Structure and tectonic evolution of the Interandean and Subandean Zones of the central Andean fold-thrust belt of Bolivia. *I Andean Tectonics*, 399-427,
Saldías, C., Speelman, S. & Van Huylenbroeck, G., 2013: Access to Irrigation Water and Distribu tion of Water Rights in the Abanico Punata, Bolivia: *Society & Natural Resources 26***,** 1008-1021. doi: 10.1080/08941920.2012.729651
SERGEOMIN, *Las Torrenteras de Cochabamba.* Ser vicio Geologico de Bolivia Regional Cocha bamba**.**
Stimson, J. 1991. *Isotopic and Geochemical Evolution of Groundwaters in Cochabamba valley, Boliv ia.* (Master), University of Waterloo, Waterloo, Ontario, Canada.
UNDP, U. N. D. P., 1979. Water resources project in Cochabamba. Report.

Personal communication

Gonzales, A. A. 2019: Professor at the Universidad Major de San Simon (UMSS) [Personal com munication].

Lecture Material

Jeppsson, H., 2017: Elektromagnetiska metoder, lecture material. Lund University. 134 s. [unpublished]
Jeppsson, H. & Dahlin, T., 2017: Geoelektrik, lecture material. Lund University. 76 s. [unpublished]

10 Appendix

Appendix A

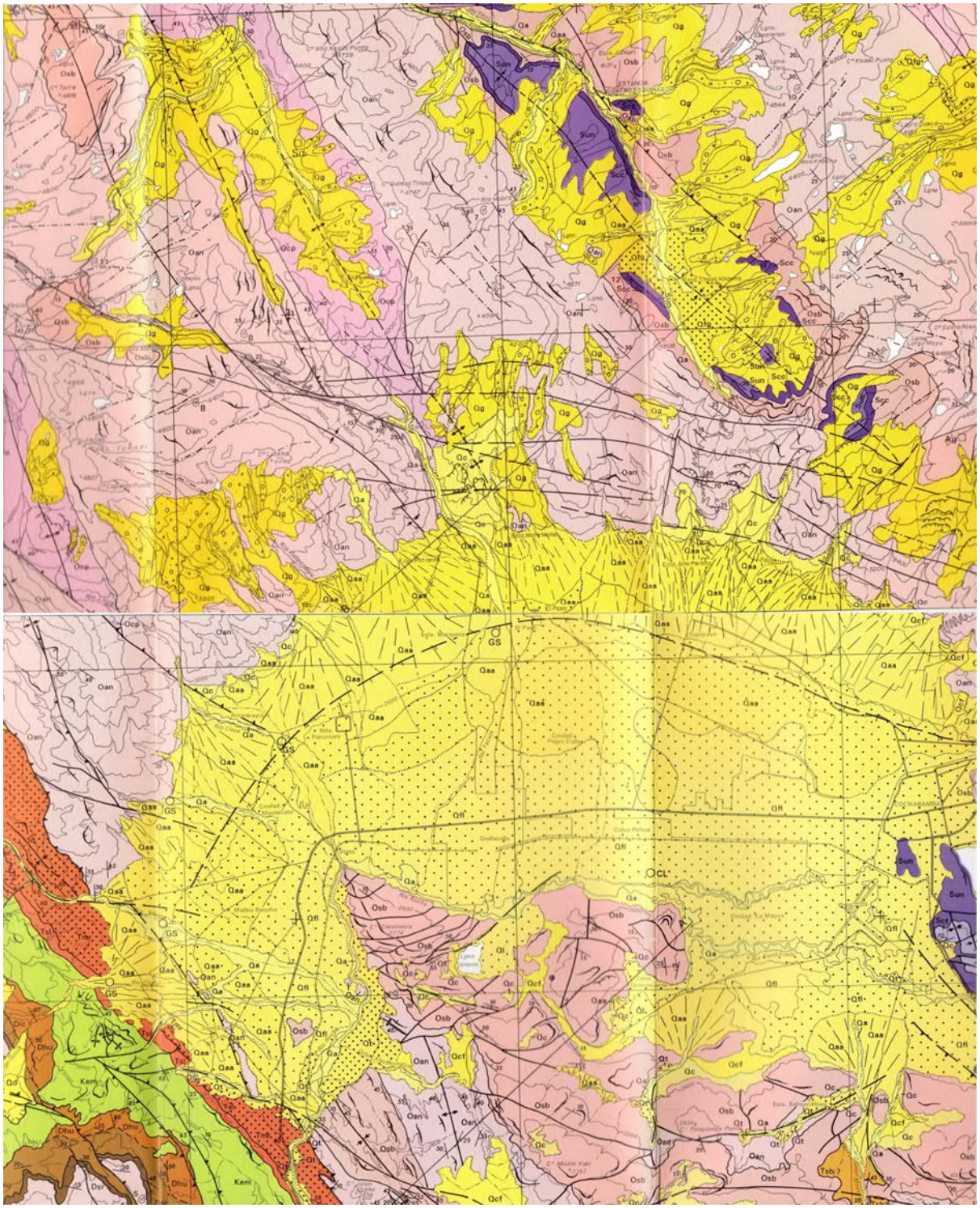

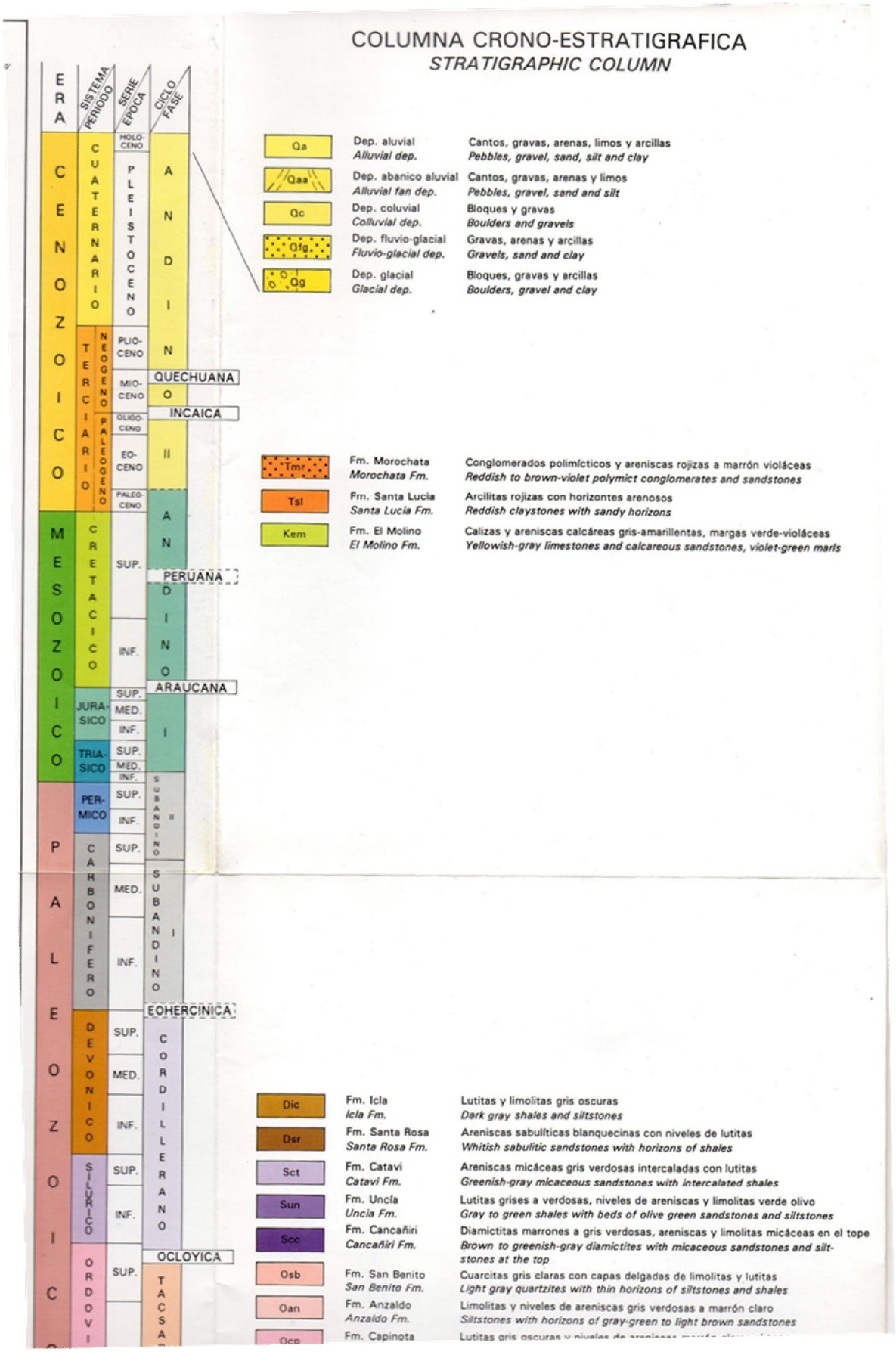
COLUMNA CRONO-ESTRATIGRAFICA
STRATIGRAPHIC COLUMN
ERA
SISTEMA PERIODO
SERIE EPOCA
CICLO FASE
CENOZOICO
CUATERNARIO
HOLOCENO
PLEISTOCENO
ANDINO
TERCIARIO
NEOGENO
PLIOCENO
MIOCENO
QUECHUANA
PALEOGENO
OLIGOCENO
INCAICA
EOCENO
II
PALEOCENO
MESOZOICO
CRETACICO
SUP.
PERUANA
INF.
ANDINO
JURASICO
SUP.
MED.
INF.
ARAUCANA
I
TRIASICO
SUP.
MED.
INF.
PALEOZOICO
PERMICO
SUP.
INF.
SUBANDINO II
CARBONIFERO
SUP.
MED.
INF.
SUBANDINO I
EOHERCINICA
DEVONICO
SUP.
MED.
INF.
CORDILLERANO
SILURICO
SUP.
INF.
OCLOYICA
ORDOVICICO
SUP.
TACSARA
Qa
Dep. aluvial
Alluvial dep.
Cantos, gravas, arenas, limos y arcillas
Pebbles, gravel, sand, silt and clay
Qaa
Dep. abanico aluvial
Alluvial fan dep.
Cantos, gravas, arenas y limos
Pebbles, gravel, sand and silt
Qc
Dep. coluvial
Colluvial dep.
Bloques y gravas
Boulders and gravels
Qfg
Dep. fluvio-glacial
Fluvio-glacial dep.
Gravas, arenas y arcillas
Gravels, sand and clay
Qg
Dep. glacial
Glacial dep.
Bloques, gravas y arcillas
Boulders, gravel and clay
Tmr
Fm. Morochata
Morochata Fm.
Conglomerados polimícticos y areniscas rojizas a marrón violáceas
Reddish to brown-violet polymict conglomerates and sandstones
Tsl
Fm. Santa Lucia
Santa Lucia Fm.
Arcilitas rojizas con horizontes arenosos
Reddish claystones with sandy horizons
Kem
Fm. El Molino
El Molino Fm.
Calizas y areniscas calcáreas gris-amarillentas, margas verde-violáceas
Yellowish-gray limestones and calcareous sandstones, violet-green marls
Dic
Fm. Icla
Icla Fm.
Lutitas y limolitas gris oscuras
Dark gray shales and siltstones
Dsr
Fm. Santa Rosa
Santa Rosa Fm.
Areniscas sabulíticas blanquecinas con niveles de lutitas
Whitish sabulitic sandstones with horizons of shales
Sct
Fm. Catavi
Catavi Fm.
Areniscas micáceas gris verdosas intercaladas con lutitas
Greenish-gray micaceous sandstones with intercalated shales
Sun
Fm. Uncía
Uncia Fm.
Lutitas grises a verdosas, niveles de areniscas y limolitas verde olivo
Gray to green shales with beds of olive green sandstones and siltstones
Scc
Fm. Cancañiri
Cancañiri Fm.
Diamictitas marrones a gris verdosas, areniscas y limolitas micáceas en el tope
Brown to greenish-gray diamictites with micaceous sandstones and siltstones at the top
Osb
Fm. San Benito
San Benito Fm.
Cuarcitas gris claras con capas delgadas de limolitas y lutitas
Light gray quartzites with thin horizons of siltstones and shales
Oan
Fm. Anzaldo
Anzaldo Fm.
Limolitas y niveles de areniscas gris verdosas a marrón claro
Siltstones with horizons of gray-green to light brown sandstones
Ocp
Fm. Capinota
Lutitas gris oscuras y niveles de

SIMBOLOS GEOLOGICOS
GEOLOGICAL SYMBOLS

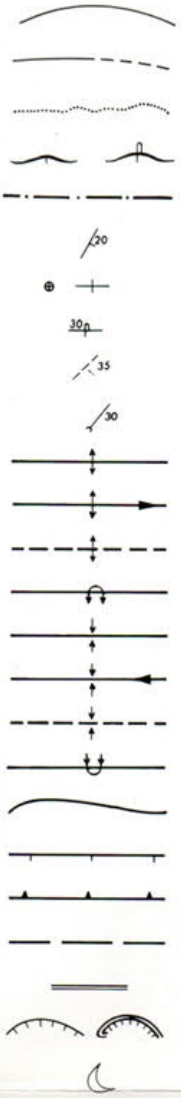

Contacto geológico	***Geological contact***
a) observado b) aproximado	*a) observed b) approximate*
c) inferido	*c) inferred*
Estrato conspicuo/volcado	*Marked bedding/overturned*
Lineamiento fotointerpretado	*Photointerpreted lineament*
Dirección de rumbo y buzamiento	***Direction of strike and dip***
a) horizontales b) verticales	*a) horizontal b) vertical*
c) invertidos o volcados	*c) inverted or overturned*
Esquistosidad	*Schistosity*
Eje del pliegue	*Plunge and direction of fold axis*
Ejes anticlinales	***Anticline axis***
a) con dirección de hundimiento	*a) with direction of plunge*
b) aproximado o inferido	*b) approximate or inferred*
c) invertido o volcado	*c) inverted or overturned*
Ejes sinclinales	***Syncline axis***
a) con dirección de hundimiento	*a) with direction of plunge*
b) aproximado o inferido	*b) approximate or inferred*
c) invertido o volcado	*c) inverted or overturned*
Fallas	***Faults***
a) Normal: dentaduras indican bloque hundido	*a) Normal: with teeth on downthrown side*
b) Inversa: dentaduras indican bloque elevado	*b) Reverse fault: with teeth on uplifted block*
c) Aproximada o inferida	*c) Approximate or inferred*
Diques/sills	*Dikes/sills*
Deslizamiento/Circo glacial	*Landslide/Glacial cirque*
Dunas	*Dunes*
Fósiles	***Fossils***
a) invertebrados b) vertebrados c) flora	*a) invertebrates b) vertebrates c) plants*
Minas y ocurrencias de minerales	***Mines and mineral occurrences***
a) mina	*a) mine*
b) minerales metálicos	*b) metallic minerals*
c) minerales no metálicos	*c) non-metallic minerals*
Zona de alteración	*Alteration zone*
Traza de perfil geológico	*Cross section*
Edad radiométrica	***Radiometric age***
Biotita/edad Ma/referencia	*Biotite/age Ma/reference*

K-Ar
Bi ■ 6.4 ± 0.3 Ma 2

SIMBOLOS TOPOGRAFICOS
TOPOGRAPHICAL SYMBOLS

Geological map from GEOBOL (1994) together with its legend.

Appendix B

Data residuals for all TEM stations (measurements) and the loop configuration used for each measurement. The

Station	Data residual		Type of configuration	Comments
	Smooth	Layered		
1	3.38	3.47	Centre loop	All OK
4	3.28	3.35	Centre loop	All OK
5	8.63	8.73	Centre loop	All OK
6	32.1	29.5	Offset	All OK
7	3.67	3.38	Offset	All OK
8	2.64	2.62	Offset	All OK
9	1.71	1.75	Offset	All OK
10	3.13	3.46	Offset	All OK
12	15.4	15.3	Offset	All OK
13	3.09	3.09	Offset	All OK
14	17.7	17.7	Offset	All OK
15	9.91	10.2	Offset	All OK
16	4.22	4.18	Offset	All OK
17	16.2	14.9	Offset	All OK
18	3.66	3.64	Offset	All OK
19	24.6	24.5	Offset	All OK
20	4.08	4.06	Offset	RC-200 coil close to powerlines.
22	3.98	3.99	Offset	All OK
23	13.7	13.6	Offset	10 m proximity to metallic fences.
24	4.38	4.21	Offset	Metallic fences were removed 100m from setup. Powerline approx 50-100m from set-up.
25	19.2	18.9	Offset	All OK
26	12.2	12.1	Offset	Powerline approx 100m away from the setup. CAT trucks were 200m away. One came approx 100m from the setup during measurement time.
27	4.46	4.39	Centre loop	One of the corners is slightly lower topographically. Another corner is approx 50m from powerlines
28	4.5	4.42	Offset	Slight topographic difference.
29	4.54	4.41	Offset	Topographic differences in the terrain. Cables were not horizontal. Could have affected the data.
30	4.71	4.52	Offset	Topographic differences in the terrain. Cables were not horizontal. Could have affected the data.

31	**8.29**	**8.3**	**Centre loop**	**Metallic fence south and powerlines north of the setup but more than 100m away. Metallic trash was found on the ground, inside and outside of the setup. They were removed but there may have been more.**
32	17.3	17.1	Offset	Metal objects 100 m away.
33	10.4	10.1	Centre loop	Topographic differences in the terrain. Cables were not horizontal and could have affected the data. This station was removed.
34	5.05	5.05	Offset	All OK
35	10.7	10.8	Centre loop	Measurement was on a football pitch. Two metallic goals were N and S of the setup. Distance from the goals were approx 100m away.
36	14.4	14.4	Centre loop	Metal trash on the ground. Some was removed but there may have been more.
37	7.88	7.8		Missing field notes
38	11.3	9.67		Missing field notes
39	17.3	4.17		Missing field notes
40	16	12.4		Missing field notes
ERT Line 1	8.27			
ERT Line 2	7.84			
ERT Line 3	11.95			
ERT Line 4	8.34			
ERT Line 5	5.26			
ERT Line 6	14.26			

comments provide available information on the proximity to metallic objects, powerlines or any other disturbances.

Appendix C

On Workbench it is necessary to set a search distance for each created profile. The used search distances for each

Search distance for the TEM profiles on Workbench	Meters
TEM line 1	100
TEM line 2	100
TEM line 6	100
TEM line 7	250
TEM line 8	250
TEM line 9	100
TEM line 10	100
Forest (TEM line 11)	250
Soccer field (TEM line 3)	250

TEM profile created are shown below.

Appendix D

The same geological map as in appendix A but focused where the study area is located. Red dots represent the TEM

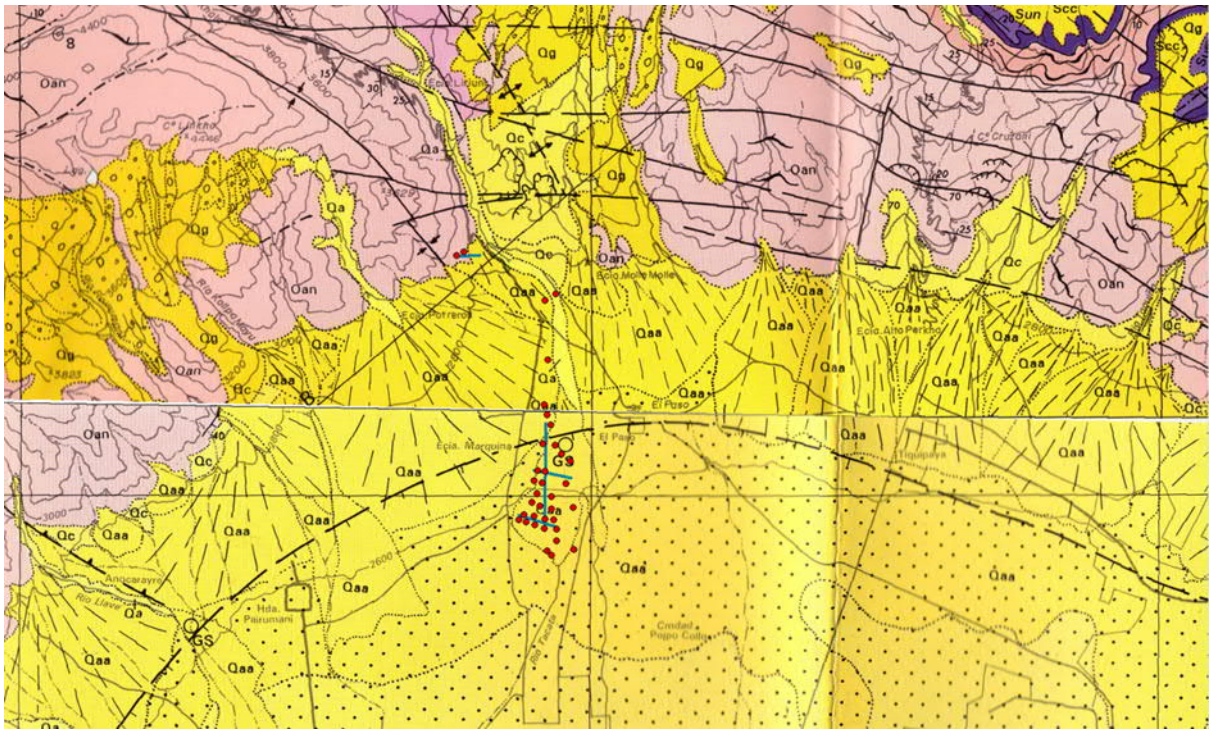

measurements and the blue lines represent the ERT lines.

Appendix E

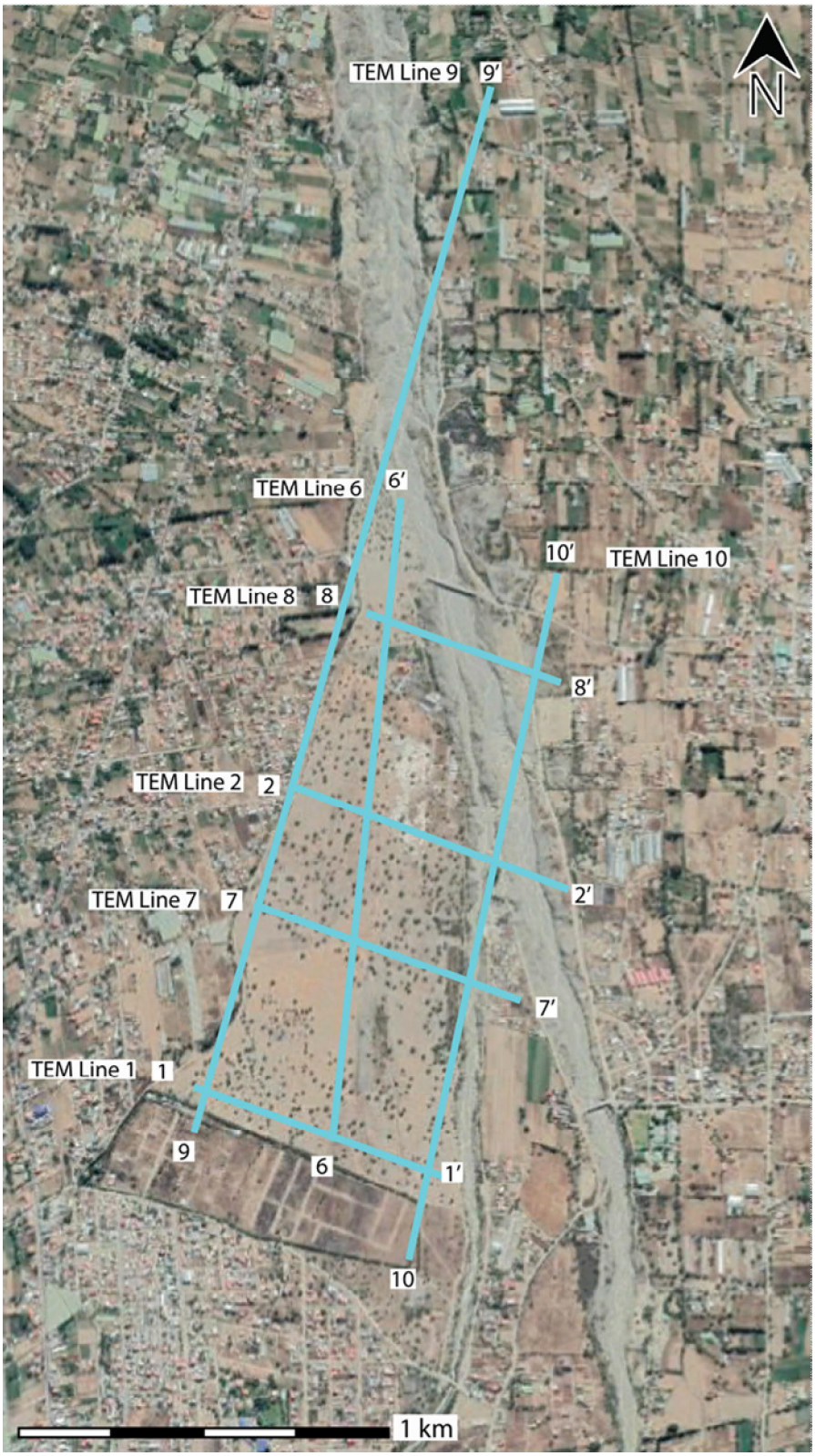

All locations of the created TEM lines on Workbench within the study area is shown below.

Appendix F

Here all remaining profiles not shown in the results are presented. In total it is four profiles: TEM line 7, 8, 9 and

7 TEM Line 7 7’

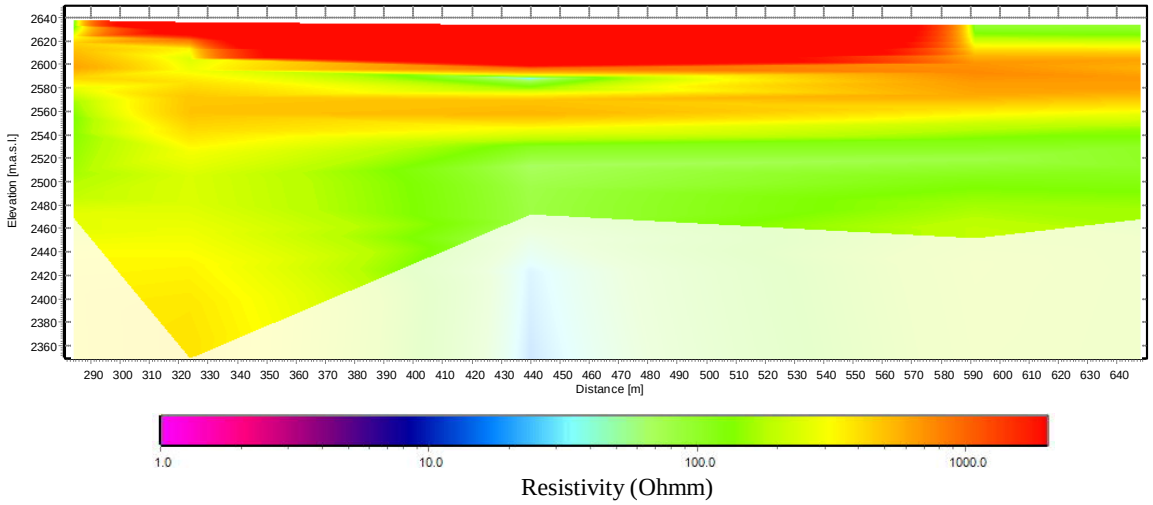

Resistivity (Ohmm)

8 TEM Line 8 8’

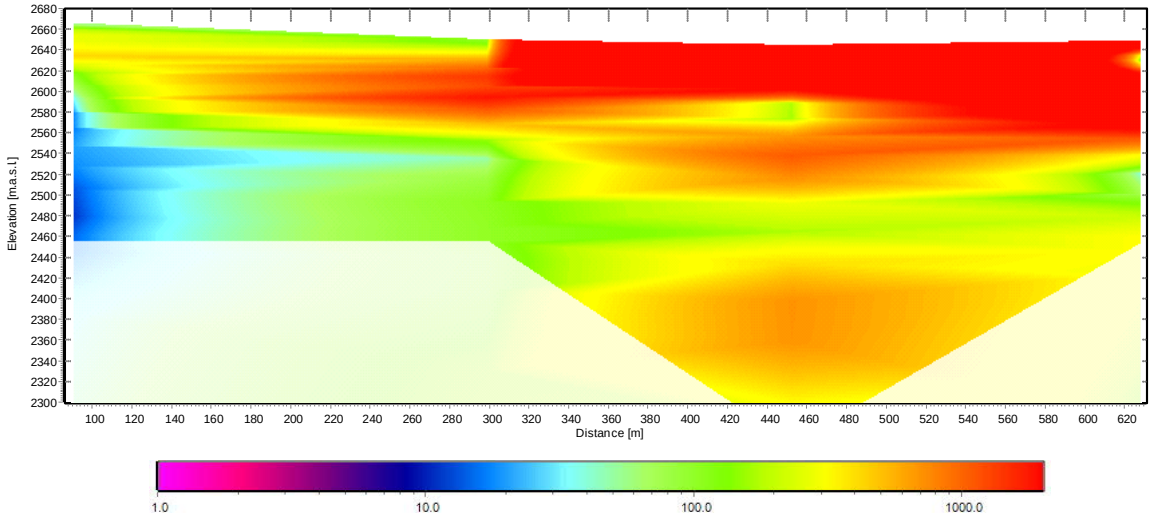

Resistivity

9’ TEM Line 9 9

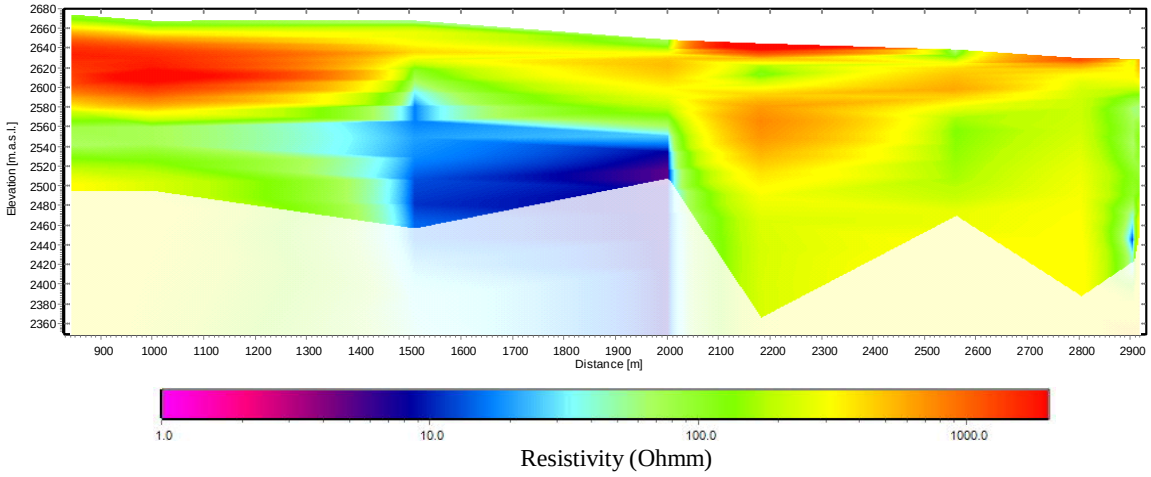

10’ TEM Line 10 10

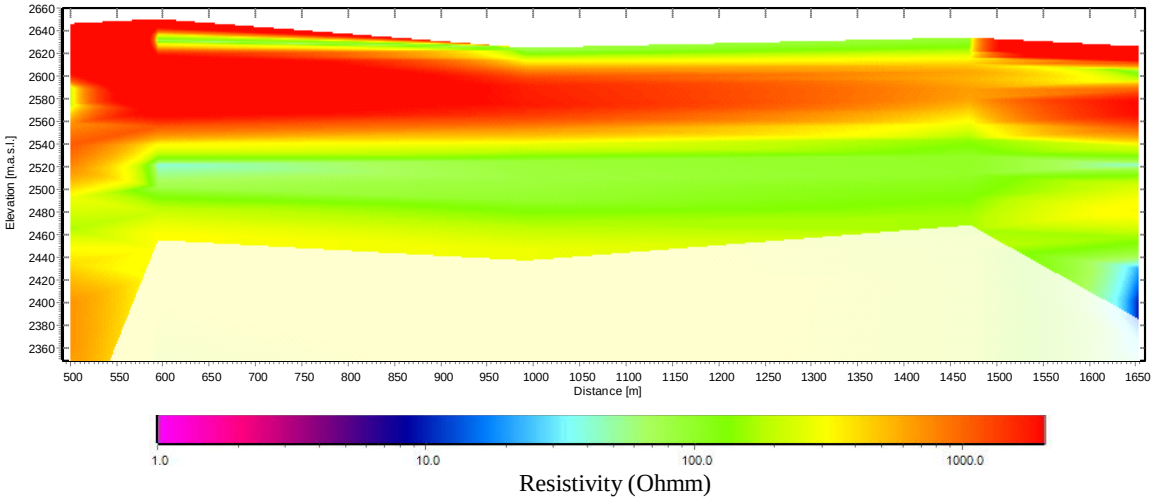

10.
Appendix G

Points used for general trend		Points not used for general trend
Farm	**River**	
1	26	31
4	27	32
5	28	35
7	29	37
8	30	38
9	34	39
10	36	40
12		
13		
14		
15		
16		
17		
18		
19		
20		
22		
23		
24		
25		

Tidigare skrifter i serien ”Examensarbeten i Geologi vid Lunds universitet”:

527. Pettersson, Johan, 2018: Ultrastructure and biomolecular composition of sea turtle epidermal remains from the Campanian (Upper Cretaceous) North Sulphur River of Texas. (45 hp)
528. Jansson, Robin, 2018: Multidisciplinary perspective on a natural attenuation zone in a PCE contaminated aquifer. (45 hp)
529. Larsson, Alfred, 2018: Rb-Sr sphalerite data and implications for the source and timing of Pb-Zn deposits at the Caledonian margin in Sweden. (45 hp)
530. Balija, Fisnik, 2018: Stratigraphy and pyrite geochemistry of the Lower–Upper Ordovician in the Lerhamn and Fågelsång -3 drill cores, Scania, Sweden. (45 hp)
531. Höglund, Nikolas, 2018: Groundwater chemistry evaluation and a GIS-based approach for determining groundwater potential in Mörbylånga, Sweden. (45 hp)
532. Haag, Vendela, 2018: Studie av mikrostrukturer i karbonatslagkäglor från nedslagsstrukturen Charlevoix, Kanada. (15 hp)
533. Hebrard, Benoit, 2018: Antropocen – vad, när och hur? (15 hp)
534. Jancsak, Nathalie, 2018: Åtgärder mot kusterosion i Skåne, samt en fallstudie av erosionsskydden i Löderup, Ystad kommun. (15 hp)
535. Zachén, Gabriel, 2018: Mesosideriter – redogörelse av bildningsprocesser samt SEM-analys av Vaca Muertameteoriten. (15 hp)
536. Fägersten, Andreas, 2018: Lateral variability in the quantification of calcareous nannofossils in the Upper Triassic, Austria. (15 hp)
537. Hjertman, Anna, 2018: Förutsättningar för djupinfiltration av ytvatten från Ivösjön till Kristianstadbassängen. (15 hp)
538. Lagerstam, Clarence, 2018: Varför svalde svanödlor (Reptilia, Plesiosauria) stenar? (15 hp)
539. Pilser, Hannes, 2018: Mg/Ca i bottenlevande foraminiferer, särskilt med avseende på temperaturer nära 0°C. (15 hp)
540. Christiansen, Emma, 2018: Mikroplast på och i havsbotten - Utbredningen av mikroplaster i marina bottensediment och dess påverkan på marina miljöer. (15 hp)
541. Staahlnacke, Simon, 2018: En sammanställning av norra Skånes prekambriska berggrund. (15 hp)
542. Martell, Josefin, 2018: Shock metamorphic features in zircon grains from the Mien impact structure - clues to conditions during impact. (45 hp)
543. Chitindingu, Tawonga, 2018: Petrological characterization of the Cambrian sandstone reservoirs in the Baltic Basin, Sweden. (45 hp)
544. Chonewicz, Julia, 2018: Dimensionerande vattenförbrukning och alternativa vattenkvaliteter. (15 hp)
545. Adeen, Lina, 2018: Hur lämpliga är de geofysiska metoderna resistivitet och IP för kartläggning av PFOS? (15 hp)
546. Nilsson Brunlid, Anette, 2018: Impact of southern Baltic sea-level changes on landscape development in the Verkeån River valley at Haväng, southern Sweden, during the early and mid Holocene. (45 hp)
547. Perälä, Jesper, 2018: Dynamic Recrystallization in the Sveconorwegian Frontal Wedge, Småland, southern Sweden. (45 hp)
548. Artursson, Christopher, 2018: Stratigraphy, sedimentology and geophysical assessment of the early Silurian Halla and Klinteberg formations, Altajme core, Gotland, Sweden. (45 hp)
549. Kempengren, Henrik, 2018: Att välja den mest hållbara efterbehandlingsmetoden vid sanering: Applicering av beslutsstödsverktyget SAMLA. (45 hp)
550. Andreasson, Dagnija, 2018: Assessment of using liquidity index for the approximation of undrained shear strength of clay tills in Scania. (45 hp)
551. Ahrenstedt, Viktor, 2018: The Neoproterozoic Visingsö Group of southern Sweden: Lithology, sequence stratigraphy and provenance of the Middle Formation. (45 hp)
552. Berglund, Marie, 2018: Basaltkuppen - ett spel om mineralogi och petrologi. (15 hp)
553. Hernnäs, Tove, 2018: Garnet amphibolite in the internal Eastern Segment, Sveconorwegian Province: monitors of metamorphic recrystallization at high temperature and pressure during Sveconorwegian orogeny. (45 hp)
554. Halling, Jenny, 2019: Characterization of black rust in reinforced concrete structures: analyses of field samples from southern Sweden. (45 hp)
555. Stevic, Marijana, 2019: Stratigraphy and dating of a lake sediment record from Lyngsjön, eastern Scania - human impact and aeolian sand deposition during the last millennium. (45 hp)
556. Rabanser, Monika, 2019: Processes of Lateral Moraine Formation at a Debris-covered Glacier, Suldenferner (Vedretta di Solda), Italy. (45 hp)

557. Nilsson, Hanna, 2019: Records of environmental change and sedimentation processes over the last century in a Baltic coastal inlet. (45 hp)
558. Ingered, Mimmi, 2019: Zircon U-Pb constraints on the timing of Sveconorwegian migmatite formation in the Western and Median Segments of the Idefjorden terrane, SW Sweden. (45 hp)
559. Hjorth, Ingeborg, 2019: Paleomagnetisk undersökning av vulkanen Rangitoto, Nya Zeeland, för att bestämma dess utbrottshistoria. (15 hp)
560. Westberg, Märta, 2019: Enigmatic worm-like fossils from the Silurian Waukesha Lagerstätte, Wisconsin, USA. (15 hp)
561. Björn, Julia, 2019: Undersökning av påverkan på hydraulisk konduktivitet i förorenat område efter in situ-saneringsförsök. (15 hp)
562. Faraj, Haider, 2019: Tolkning av georadarprofiler över grundvattenmagasinet Verveln - Gullringen i Kalmar län. (15 hp)
563. Bjermo, Tim, 2019: Eoliska avlagringar och vindriktningar under holocen i och kring Store Mosse, södra Sverige. (15 hp)
564. Langkjaer, Henrik, 2019: Analys av Östergötlands kommande grundvattenresurser ur ett klimtperspektiv - med fokus på förstärkt grundvattenbildning. (15 hp)
565. Johansson, Marcus, 2019: Hur öppet var landskapet i södra Sverige under Atlantisk tid? (15 hp)
566. Molin, Emmy, 2019: Litologi, sedimentologi och kolisotopstratigrafi över krita–paleogen-gränsintervallet i borrningen Limhamn-2018. (15 hp)
567. Schroeder, Mimmi, 2019: The history of European hemp cultivation. (15 hp)
568. Damber, Maja, 2019: Granens invandring i sydvästa Sverige, belyst genom pollenanalys från Skottenesjön. (15 hp)
569. Lundgren Sassner, Lykke, 2019: Strandmorfologi, stranderosion och stranddeposition, med en fallstudie på Tylösand sandstrand, Halland. (15 hp)
570. Greiff, Johannes, 2019: Mesozoiska konglomerat och Skånes tektoniska utveckling. (15 hp)
571. Persson, Eric, 2019: An Enigmatic Cerapodian Dentary from the Cretaceous of southern Sweden. (15 hp)
572. Aldenius, Erik, 2019: Subsurface characterization of the Lund Sandstone – 3D model of the sandstone reservoir and evaluation of the geoenergy storage potential, SW Skåne, South Sweden. (45 hp)
573. Juliusson, Oscar, 2019: Impacts of subglacial processes on underlying bedrock. (15 hp)
574. Sartell, Anna, 2019: Metamorphic paragenesis and P-T conditions in garnet amphibolite from the Median Segment of the Idefjorden Terrane, Lilla Edet. (15 hp)
575. Végvári, Fanni, 2019: Vulkanisk inverkan på klimatet och atmorsfärcirkulationen: En litterarurstudie som jämför vulkanism på låg respektive hög latitud. (15 hp)
576. Gustafsson, Jon, 2019: Petrology of platinum-group element mineralization in the Koillismaa intrusion, Finland. (45 hp)
577. Wahlquist, Per, 2019: Undersökning av mindre förkastningar för vattenuttag i sedimentärt berg kring Kingelstad och Tjutebro. (15 hp)
578. Gaitan Valencia, Camilo Esteban, 2019: Unravelling the timing and distribution of Paleoproterozoic dyke swarms in the eastern Kaapvaal Craton, South Africa. (45 hp)
579. Eggert, David, 2019: Using Very-Low-Frequency Electromagnetics (VLF-EM) for geophysical exploration at the Albertine Graben, Uganda - A new CAD approach for 3D data blending. (45 hp)
580. Plan, Anders, 2020: Resolving temporal links between the Högberget granite and the Wigström tungsten skarn deposit in Bergslagen (Sweden) using trace elements and U-Pb LA-ICPMS on complex zircons. (45 hp)
581. Pilser, Hannes, 2020: A geophysical survey in the Chocaya Basin in the central Valley of Cochabamba, Bolivia, using ERT and TEM. (45 hp)

LUNDS UNIVERSITET

Geologiska institutionen
Lunds universitet
Sölvegatan 12, 223 62 Lund